Wilfrid Laurier University

Scholars Commons @ Laurier

Theses and Dissertations (Comprehensive)

2016

THE ROLE OF ORGANIC MATTER IN THE SURFACE CHEMISTRY OF ARSENIC COMPOUNDS ON IRON–(OXYHYDR)OXIDES STUDIED BY ATR-FTIR

Arthur Situm
Wilfrid Laurier University, arthursitum@hotmail.com

Follow this and additional works at: https://scholars.wlu.ca/etd

Part of the Environmental Chemistry Commons, Geochemistry Commons, and the Physical Chemistry Commons

Recommended Citation

Situm, Arthur, "THE ROLE OF ORGANIC MATTER IN THE SURFACE CHEMISTRY OF ARSENIC COMPOUNDS ON IRON–(OXYHYDR)OXIDES STUDIED BY ATR-FTIR" (2016). *Theses and Dissertations (Comprehensive)*. 1834.
https://scholars.wlu.ca/etd/1834

This Thesis is brought to you for free and open access by Scholars Commons @ Laurier. It has been accepted for inclusion in Theses and Dissertations (Comprehensive) by an authorized administrator of Scholars Commons @ Laurier. For more information, please contact scholarscommons@wlu.ca.

THE ROLE OF ORGANIC MATTER IN THE SURFACE CHEMISTRY OF ARSENIC COMPOUNDS ON IRON–(OXYHYDR)OXIDES STUDIED BY ATR-FTIR

by

ARTHUR SITUM

Bachelor of Science (Honours), Wilfrid Laurier University, 2014

Thesis

Submitted to the Department of Chemistry and Biochemistry

Faculty of Science

in partial fulfillment of the requirements for

Master of Science in Chemistry

Wilfrid Laurier University

© Arthur Situm 2016

TABLE OF CONTENTS

Acknowledgements 4
List of publications 5
Abstract 6
List of tables 8
List of figures 10
1 Introduction 16
1.1 Arsenic compounds in the environment 16
1.1.1 Inorganic arsenic 17
1.1.2 Organic arsenic 18
1.1.3 Arsenic cycling pathways: redox and methylation chemistry 19
1.2 Environmental regulations of arsenic in soils and drinking water 20
1.2.1 Methods for removal of arsenic from drinking water 21
1.2.2 Analytical methods for the detection and analysis of arsenic in drinking water 22
1.3 Organic matter in soil 22
1.4 Role of organics in controlling the environmental fate of arsenic compounds 23
1.4.1 Bulk/batch studies 25
1.4.2 Surface sensitive infrared spectroscopic studies 26
2 Overview of thesis objectives 28
3 Experimental and modeling approach 28
3.1 Reagents 28
3.2 Characterization of hematite nanoparticles 29
3.3 Film preparations on ATR-FTIR crystal 30
3.4 Experimental Procedure: 31
3.4.1 Principle of ATR-FTIR as a surface sensitive technique 31
3.4.2 Calibration curves from spectra collected for aqueous phase species 32
3.4.3 Adsorption and desorption kinetics using ATR-FTIR 32
3.4.4 Adsorption isotherm studies using ATR-FTIR 33

3.4.5 pH envelope studies using ATR-FTIR 33
3.5 Modeling of adsorption kinetics 33
3.6 Modeling of desorption kinetics 35
3.7 Modeling adsorption thermodynamics with the Langmuir model 36
4 Results and discussion 37
4.1 Characterization of Aqueous phase model organics using ATR-FTIR 37
4.2 Adsorption thermodynamics of model organics using ATR-FTIR 40
4.2.1 Organic adsorption spectra and assignment 40
4.2.2 Adsorption isotherms on hematite at room temperature 47
4.2.3 pH envelope curves on hematite 50
4.3 Adsorption kinetics of model organic matter 53
4.4 Desorption kinetics of model organic matter on hematite 59
4.4.1 Desorption kinetics of citrate due to flowing arsenicals 59
4.4.2 Desorption kinetics of oxalate due to flowing arsenicals 62
4.4.3 Desorption kinetics of pyrocatechol due to flowing arsenicals 64
4.4.4 Effect of Cl^- (aq) on the desorption kinetics of surface organics 66
4.4.5 Comparison of surface organics desorption kinetics 68
4.5 Adsorption kinetics of arsenic compounds on hematite 70
4.5.1 Adsorption on clean surfaces-spectra, spectral assignment and kinetic curves 70
4.5.2 Adsorption on surface pre-exposed to model organic matter-kinetic curves 72
5 Conclusions and significance 78
Appendix a: Macros used in data collection 80
Appendix b: Macros used in data analysis 83
Appendix c: Spectral math used in data analysis 93
Appendix d: Speciation curve calculations 97
References 99

Acknowledgements

I would like to begin by thanking Dr. Al-Abadleh for her guidance and patience while working with me over the past five years. Since the day I knocked on her office door and asked if there was any research work for me to do in the lab, it has been a constant learning experience. I would also like to thank the members of my committee, Dr. Ian Hamilton and Dr. Scott Smith, for their feedback and guidance throughout this project.

I would also like to thank current and past members of the Dr. Al-Abadleh group: Dr. Hamid Firooz, Derek Arts, Samantha Slikboer, Kevin Jakiela, Brandon Caughell, Geoffrey Williams, Aminur Rahman, Adrian Adamescu and especially Abdus Sabur and Julia Tofan-Lazar for their support, feedback and for any training received. It has been a pleasure to have worked with all of you. Thanks as well to my good friends Michael Forsyth, Arnold Mak, Vishal Singh, Mikal Jamokha and Dean Blasutti for discussing with me my research frustrations and excitements.

Finally, I would like to thank my family for all their support and encouragement throughout my studies. To receive such love and positivity is truly a blessing.

List of Publications

(1) **Arthur Situm,** Mohammad A. Rahman, Sabine Goldberg, and Hind A. Al-Abadleh*. Spectral Characterization and Surface Complexation Modeling of Organics on Hematite Nanoparticles: An Interface Important in Environmental Systems and Medical Applications. Submitted (2016).

A. Situm contributed the experimental data and figures, initial analysis, and literature search.

(2) **Arthur Situm,** Mohammad A. Rahman, Nick Allen, Nadine Kaberngi, and Hind A. Al-Abadleh. Type of organic functional groups on the surface of hematite nanoparticles affects surface charge and arsenicals binding kinetics. (In preparation)

A. Situm contributed the experimental data and figures, initial analysis, first draft of the manuscript and literature search.

Abstract

The interaction of organic matter with the interfaces of active soil components such as iron oxides is ubiquitous within soil environments. The presence of organics at these interfaces may have implications for other soil constituents whose mobility is controlled by their ability to bind to active soil components. Most of the studies performed to date which look at these interactions are bulk/batch studies performed ex-situ. Attenuated total internal reflectance Fourier transform infrared spectroscopy (ATR-FTIR) was utilized within this work to study interactions between select model organics (citrate, oxalate and pyrocatechol) and iron−(oxyhydr)oxides, as well as their effect on the surface chemistry of organic and inorganic arsenicals. Using baseline-corrected peak height measurements, model organics were reacted with iron−(oxyhydr)oxide nanoparticles as a function of pH and concentration to generate pH envelope and adsorption isotherm curves. The Langmuir adsorption model was applied to adsorption isotherm curves to obtain K_{eq} constants for model organics on the surface of hematite nanoparticles.

Kinetic adsorption experiments were performed for model organics on hematite nanoparticles over a range of ionic strength conditions, with results showing a positive correlation between ionic strength and observed initial adsorption rates (r_{obs1}), obtained from the Langmuir adsorption model, of citrate and oxalate. Experiments on the kinetic desorption of model organics from the surface of hematite nanoparticles were also carried out to obtain initial rates of model organic desorption (k'_{des1}) using the Langmuir desorption model; 1 mM of arsenate, 1 mM of dimethylarsinic acid (DMA), and a range of chlorine concentrations were utilized as the desorbing agents. These results show that arsenate is an effective desorbing agent for all three of the model organics. Conversely, the effect of DMA and chloride as desorbing agents varied, with citrate being moderately sensitive, oxalate being very sensitive, and pyrocatechol being insensitive.

Arsenate and DMA adsorption kinetic experiments on hematite nanoparticles, which were either reacted or unreacted with model organics, were performed to obtain r_{obs1}. These experiments were plotted as a function of aqueous arsenic concentration, analyzed using the Langmuir adsorption model to obtain pseudo- first order adsorption rates (k_{ads1}). The results of these experiments show that the presence of surface oxalate on hematite nanoparticles has an enhancing effect on the initial rates of arsenate and DMA adsorption, when compared to unreacted hematite. Conversely, the presence of surface pyrocatechol was shown to have an inhibiting effect on the initial rate of adsorption of arsenate to hematite nanoparticles.

Results shown herein, along with aqueous phase comparisons of iron organic standards, provided information that has culminated in proposed surface complexes of the studied model organics on the surface of hematite nanoparticles under environmentally-relevant conditions. It is proposed that: oxalate forms a combination of outer-sphere and inner-sphere binuclear monodentate complexes, citrate forms an inner-sphere monodentate complex with either singly- or doubly-deprotonated carboxylic groups, and pyrocatechol forms a mixture of inner-sphere binuclear bidentate and monodentate surface complexes. The significance of this work is in providing a better fundamental understanding of the effect that different organic functional groups have on the binding of arsenicals to geosorbents, and thus the mobility of arsenicals within environments where organics are prevalent.

List of Tables

Table 1. Examples of environmentally relevant inorganic arsenic compounds at pH 7 18

Table 2. Examples of environmentally relevant organic arsenic compounds at pH 7 19

Table 3. Band assignments for ATR-FTIR absorption spectra of aqueous citrate and citrate adsorbed on hematite and goethite particles. 42

Table 4. Band assignments for ATR-FTIR absorption spectra of aqueous oxalate and oxalate adsorbed on hematite and goethite particles. 44

Table 5. Band assignments for ATR-FTIR absorption spectra of aqueous pyrocatechol and pyrocatechol adsorbed on hematite and goethite particles. 44

Table 6. log($55.5K_{eq}$) values calculated from K_{eq} values in Figure 15. 49

Table 7. Linearized first-order observed adsorption rates (min^{-1}) at various ionic strength conditions of model organics on 6 mg hematite film. 59

Table 8. Linearized first-order observed desorption rates (min^{-1}) of model organics from 6 mg hematite film. 68

Table 9. Linearized first-order observed rate constants of 1.0 mM arsenate and 1.0 mM DMA adsorption onto 6 mg hematite in the presence and absence of adsorbed model organics. 74

Table 10. Best-fit parameters from the linear least-squares regression to the experimental data of the observed adsorption rate (r_{obs}) versus [arsenate(aq)] as shown in Figure 37. For the adsorption of arsenate on hematite in the presence and absence of surface organics. 1 mM solution of each organic was flown over hematite for 80 min at 10 mM KCl and pH 7 prior to arsenate flow. 76

Table 11. Best-fit parameters from the linear least-squares regression to the experimental data of the observed adsorption rate (r_{obs}) versus [DMA(aq)] as shown in Figure 38. For the adsorption of

DMA on hematite in the presence and absence of surface organics. 1 mM solution of each organic was flown over hematite for 80 min at 10 mM KCl and pH 7 prior to DMA flow..... 77

List of Figures

Figure 1. Anthropogenic sources and fate of arsenic in the environment..... 16

Figure 2. The Challenger mechanism for the biological methylation of arsenate. 20

Figure 3. TEM image of hematite nanoparticles used in this study. [The scale bar corresponds to 20 nm.] 30

Figure 4. Diagram of ATR-FTIR crystal in the flow cell. 32

Figure 5. Speciation curves of (a) citric acid, (b) oxalic acid and (c) pyrocatechol. The solid black line on each plot indicates pH 7 conditions at which experiments were conducted. 37

Figure 6. ATR-FTIR absorbance spectra of 0.1 M aqueous citrate (CA), oxalate (OA) and pyrocatechol (PC) at pH 7, I = 10 mM KCl. Clean ZnSe ATR crystal used (no film)..... 38

Figure 7. ATR-FTIR absorbance spectra of a) citrate, c) oxalate and e) pyrocatechol, respectively, over a concentration range of 0.005 to 0.1 M. b), d) and f) calibration curves generated from baseline-corrected ATR absorbances at 1570 cm^{-1} for citric and oxalate and 1257 cm^{-1} for pyrocatechol. Error bars are ±s. 39

Figure 8. ATR-FTIR absorption spectra of adsorbed citrate, oxalate and, pyrocatechol (1 mM) at pH 7, I = 10 mM KCl, and 2 mL/min flow rate at room temperature on a) 6 mg hematite film and b) 16 mg goethite films after 80 min flow time. 40

Figure 9. Complexes formed by citrate with the surface of hematite and goethite. (Left): protonated inner-sphere monodentate, (Right): deprotonated inner-sphere monodentate..... 41

Figure 10. Complexes formed by oxalate with the surface of hematite and goethite. (Left): inner-sphere bidentate mononuclear, (Right): outer-sphere complex. 43

Figure 11. Complexes formed by pyrocatechol with the surface of hematite and goethite. (Left): inner-sphere bidentate binuclear, (Right): inner-sphere monodentate..... 45

Figure 12. ATR-FTIR absorption spectra of surface carbonate desorption by nitrogen gas bubbled, at pH 7, and I = 10 mM KCl, using a 2 mL/min flow rate at room temperature on 6 mg hematite film. 46

Figure 13. ATR-FTIR absorbance spectra of adsorbed a) citrate, b) oxalate and c) pyrocatechol respectively, collected as a function of concentration. Adsorption of model organics (1 mM) on 6 mg hematite film at pH 7, I = 10 mM KCl, and a 2 mL/min flow rate at room temperature and nitrogen gas bubbling. 46

Figure 14. ATR-FTIR absorbance spectra of adsorbed a) citrate, b) oxalate and c) pyrocatechol respectively, collected as a function of time. Adsorption of model organics on 6mg hematite film at varying concentrations ranging from 10^{-6} M to 10^{-3} M (pH 7, I = 10 mM KCl, and a 2 mL/min flow rate at room temperature). 47

Figure 15. Adsorption isotherms of a) citrate b) oxalate and c) pyrocatechol on 6 mg hematite film at pH 7, I = 10 mM KCl, and a 2 mL/min flow rate at room temperature. The solid line represents the least-squares fitting of the 1-site Langmuir adsorption model: Absorbance = $(Amax*K_{eq}*[organic]/M)/(1+K_{eq}*[organic]/M)$. Data points represent the average of three to four experiments. Error bars are ±s. 48

Figure 16. Linearized absorbances for the adsorption of a) citrate, b) oxalate and c) pyrocatechol on 6 mg hematite film as a function of concentration at pH 7, I = 10 mM KCl, and a 2 mL/min flow rate at room temperature. [Data points represent the average of three to four experiments and error bars were removed for clarity.] 49

Figure 17. Adsorption of model organics (1 mM) on 6 mg hematite film at varying pH, I = 10 mM KCl, and a 2 mL/min flow rate at room temperature and nitrogen gas bubbling. ATR-FTIR absorbance spectrum of adsorbed a) citrate, b) oxalate and c) pyrocatechol respectively. 51

Figure 18. Adsorption of a) citrate b) oxalate and c) pyrocatechol adsorption on 6 mg hematite film as a function of pH, at I = 10 mM KCl, and a 2 mL/min flow rate at room temperature. Data points represent the average of three experiments. Error bars are ±s. 52

Figure 19. Adsorption of model organics (1 mM) on 16 mg goethite film at varying pH, I = 10 mM KCl, and a 2 mL/min flow rate at room temperature and nitrogen gas bubbling. ATR-FTIR absorbance spectra of adsorbed a) citrate, b) oxalate and c) pyrocatechol respectively..... 53

Figure 20. Adsorption of a) citrate b) oxalate and c) pyrocatechol adsorption on 16 mg goethite film as a function of pH, at I = 10 mM KCl, and a 2 mL/min flow rate at room temperature. Data points represent the average of three experiments. Error bars are ±s. 54

Figure 21. Adsorption of model organics (1 mM) on to a clean, 6 mg hematite film at pH 7, I = 10 mM KCl, and a 2 mL/min flow rate at room temperature. ATR-FTIR absorbance spectra of adsorbed a) citrate, b) oxalate and c) pyrocatechol respectively, collected as a function of time. 55

Figure 22. Adsorption kinetic curves generated from the baseline-corrected ATR-FTIR absorbances for a) citrate, b) oxalate and c) pyrocatechol adsorbed on to a clean, 6 mg hematite film at pH 7, I = 10 mM KCl, and a 2 mL/min flow rate at room temperature, respectively. Data points represent the average of three to four experiments. Error bars are ±s. 56

Figure 23. Adsorption kinetics of a) citrate, b) oxalate, and c) pyrocatechol on 6 mg hematite film with 0, 10, 100, and 1000 mM KCl at pH 7. [Data points represent the average of two to four experiments and error bars have been removed for clarity.] 57

Figure 24. Linearized adsorption kinetics of a) citrate, b) oxalate, and c) pyrocatechol on 6 mg hematite film with 0, 10, 100, and 1000 mM KCl at pH 7. ln(1-(A(Organic)/A(OrganicMax))) with A(Organic) corresponding the band measured for citric oxalate, and pyrocatechol respectively.

[Data points represent the average of two to four experiments and error bars have been removed for clarity.] 58

Figure 25. ATR-FTIR absorbance spectra correspond to citrate desorption from 6 mg hematite film at pH 7, I = 10 mM KCl, and a 2 mL/min flow rate at room temperature, by the flowing of a) 10 mM Cl^-, b) 1 mM DMA and c) 1 mM Ars respectively. 60

Figure 26. Desorption kinetic curves generated from the baseline-corrected ATR-FTIR absorbances of a) citrate from 6 mg hematite film at pH 7, I = 10 mM KCl, and a 2 mL/min flow rate at room temperature, by 10 mM KCl, 1.0 mM Arsenate and 1.0 mM DMA, and b) shows ln(A(Organic)/A(OrganicMax)) with A(Organic) corresponds to absorbance at 1579 cm^{-1}. Data points represent the average of two to four experiments and error bars have been removed for clarity. 61

Figure 27. ATR-FTIR absorbance spectra correspond to oxalate desorption from 6 mg hematite film at pH 7, I = 10 mM KCl, and a 2 mL/min flow rate at room temperature, by the flowing of a) 10 mM Cl^-, b) 1 mM DMA and c) 1 mM Ars respectively. 62

Figure 28. Desorption kinetic curves generated from the baseline-corrected ATR-FTIR absorbances of a) oxalate from 6 mg hematite nanoparticles at pH 7, I = 10 mM KCl, and a 2 mL/min flow rate at room temperature, by 10 mM Cl^-, 1.0 mM Arsenate and 1.0 mM DMA, and b) shows ln(A(Organic)/A(OrganicMax)) with A(Organic) corresponds to absorbance at 1658 cm^{-1}. Data points represent the average of two to four experiments and error bars have been removed for clarity. 63

Figure 29. ATR-FTIR absorbance spectra correspond to pyrocatechol desorption from 6 mg hematite film at pH 7, I = 10 mM KCl, and a 2 mL/min flow rate at room temperature, by the flowing of a) 10 mM Cl^-, b) 1 mM DMA and c) 1 mM Ars respectively. 64

Figure 30. Desorption kinetic curves generated from the baseline-corrected ATR-FTIR absorbances of a) pyrocatechol from 6 mg hematite film at pH 7, I = 10 mM KCl, and a 2 mL/min flow rate at room temperature, by 10 mM Cl^-, 1.0 mM Arsenate and 1.0 mM DMA, and b) shows ln(A(Organic)/A(OrganicMax)) with A(Organic) corresponds to absorbance at 1257 cm^{-1}. Data points represent the average of two to four experiments and error bars have been removed for clarity. 65

Figure 31. Desorption kinetics of a) citrate, c) oxalate, and e) pyrocatechol from 6 mg hematite film at pH 7, and a 2 mL/min flow rate at room temperature by 0, 10, 100, and 1000 mM Cl-. [Data points represent the average of two to four experiments and error bars have been removed for clarity.] 66

Figure 32. Desorption kinetics of a) citrate, c) oxalate, and e) pyrocatechol from 6 mg hematite film at pH 7, and a 2 mL/min flow rate at room temperature by 0, 10, 100, and 1000 mM Cl^-. b), d), and f) show ln(A(Organic)/A(OrganicMax)) with A(Organic) corresponding the band measured for citric oxalate, and pyrocatechol respectively. [Data points represent the average of two to four experiments and error bars have been removed for clarity.] 67

Figure 33. ATR-FTIR absorbance spectra of a) 1.0 mM arsenate and b) 1.0 mM DMA adsorption on to a clean, 6 mg hematite film at pH 7, I = 10 mM KCl, and a 2 mL/min flow rate at room temperature. 70

Figure 34. Baseline-corrected adsorption kinetics of a) 1.0 mM arsenate and b) 1.0 mM DMA on to a clean, 6 mg hematite film at pH 7, I = 10 mM KCl, and a 2 mL/min flow rate at room temperature, respectively. Data points represent the average of two to four experiments. Error bars are ±s. 71

Figure 35. ATR-FTIR absorbance spectra of 1.0 mM arsenate adsorption on to a a) citrate, c) oxalate and e) pyrocatechol saturated 6 mg hematite film and 1.0 mM DMA adsorption on to a b) citrate, d) oxalate and f) pyrocatechol saturated 6 mg hematite film at pH 7, I = 10 mM KCl, and a 2 mL/min flow rate at room temperature. All absorbance spectra were generated using the corresponding 80 min model organic adsorption time single beam spectra as reference spectra. 72

Figure 36. Baseline-corrected adsorption kinetics of a) arsenate and c) DMA respectively, on citrate, oxalate, pyrocatechol and unreacted hematite films at pH 7, I = 10 mM KCl, and a 2 mL/min flow rate at room temperature, and b) and d) show ln(1-(A(As)/A(AsMax))) with A(As) corresponding to each hematite film's arsenate or DMA peak respectively. Data points represent the average of two to four experiments and error bars have been removed for clarity. 73

Figure 37. Dependency of a) the observed initial rate of adsorption (r_{obs}) on [arsenate(aq)] on hematite surfaces in the presence and absence of surface organics. Lines through the data represent linear least-squares fits and b) shows maximum adsorption of arsenate on hematite surfaces in the presence and absence of surface organics as a function of [arsenate(aq)]. Error bars are ±s. 75

Figure 38. a) Dependency of a) the observed initial rate of adsorption (robs) on [DMA(aq)] on hematite surfaces in the presence and absence of surface organics. Lines through the data represent linear least-squares fits and b) shows maximum adsorption of DMA on hematite surfaces in the presence and absence of surface organics as a function of [DMA(aq)]. Error bars are ±s. 77

1 Introduction

1.1 Arsenic compounds in the environment

Arsenic is a natural element that exist within the environment and can be introduced through a number of natural and anthropogenic processes including: copper and gold smelting, oil refinement, the burning of coal high in arsenic, runoff from municipal waste and natural weathering of particular types of rock and minnerals.[1-2] In the past, uses of arsenic included chromated copper arsenate for wood preservation, roxarsone used as a chicken steroid and the utilization of organic arsenic as a pesticide and herbicide.[1-3] Arsenic has been identified as a human toxin and carcinogen, with its toxic effects dependent on the species, oxidation state and route of exposure.[4] Because of this variability, understanding the environmental chemistry of arsenic is important in lowering rates of exposure and in finding new methods for remediation. The following Figure 1 illustrates anthropogenic and natural sources of arsenic, and processes effecting the environmental fate of arsenic.

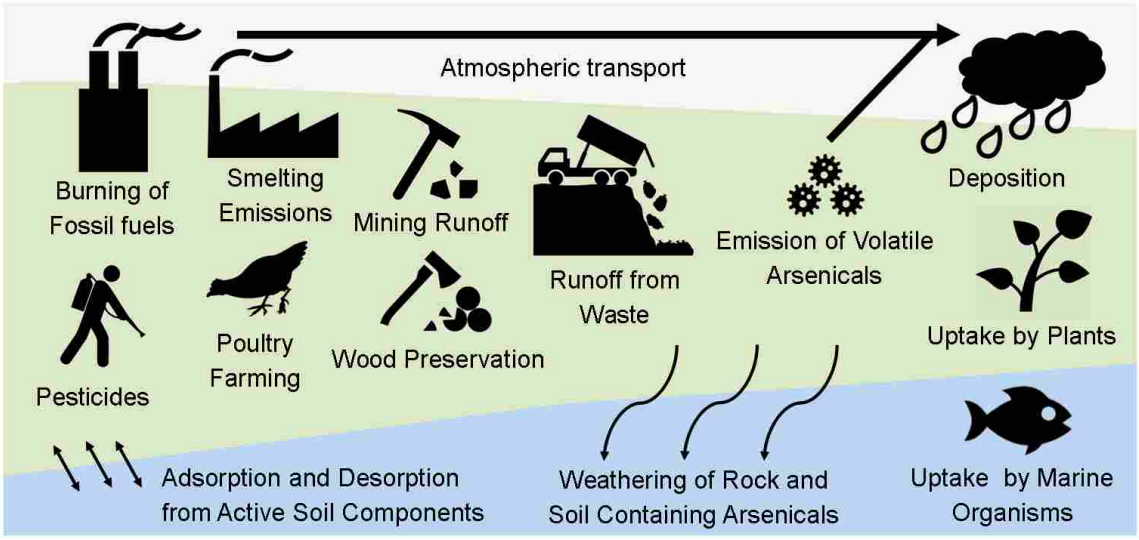

Figure 1. Anthropogenic sources and fate of arsenic in the environment.

As shown in Figure 1, the environmental fate of arsenic can be uptake by marine organisms and plants. In the latter, this occurs via transport proteins within roots that are often meant for the uptake of the phosphorus, which forms compounds similar to ones formed by arsenic. Once within the plant, As(V) undergoes reduction to As(III) and toxic effects are either coped with via detoxification mechanisms, or the plant experiences the toxic effects of arsenics presence.[5]

1.1.1 Inorganic arsenic

Arsenic can be found in a wide array of rocks and minerals. The most common example of mineralized arsenic is arsenopyrite (FeAsS) and is often associated with the transition metals Cd, Pb, Ag, Au, Sb, P, W and Mo.[2] Because of this association, mining and smelting introduce inorganic arsenic into the environment through stack emission from smelting processes or acid mine drainage.[2, 6] An example of this is Giant Mine in the Northwest Territories, where years of mining gold from arsenopyrite ore has produced gas with a high arsenic concentration, that oxidizes to form arsenic trioxide (As_2O_3).[6-7] Arsenic gas is produced during the roosting process where in the ore is heated at high temperatures to release the gold but also results in the release of arsenic gas. Although most of the arsenic can be removed from the stack, these environmental precautions were not implemented at Giant Mine till 1951 (3 years after the opening of the mine) which resulted in contamination extending out 17 km from the property.[6-7] Copper mining and smelting represents the single largest anthropogenic input of arsenic into the environment, with the burning of arsenopyrite-contaminated coal as the second highest source.[2, 6] Although phased out in Canada, chromated copper arsenate was used as a wood preservative, which caused the slow leaching of arsenic from woodlots in which it was utilized.[6] In soil and water, arsenic predominantly exists as either arsenate or arsenite depending on redox conditions.[2] Table 1 shows examples of inorganic forms of arsenic most commonly found within soil environments.

Table 1. Examples of environmentally relevant inorganic arsenic compounds at pH 7

Name of arsenic compound	Oxidation state	Structure
Arsenic acid (Arsenate)	As (V)	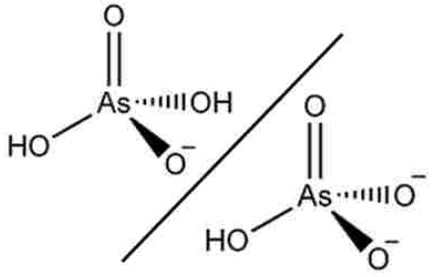
Arsenous acid (Arsenite)	As (III)	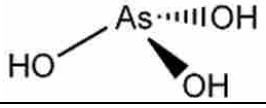

1.1.2 Organic arsenic

The formation of organic arsenic in the environment occurs through the biotransformation of inorganic species of arsenic. Many species of organic arsenic exist, and a few have been used for specific purposes. For example, 4-hydroxy-3-nitrobenzenearsenic acid, known as Roxarzone, was historically used as a steroid in the poultry industry in Canada.[3] Conversely, dimethylarsinic acid (DMA), in conjunction with other so called "rainbow" herbicides, was used in the Vietnam War by US forces for crop destruction.[8] In general, both organic and inorganic species of arsenic have historically been used domestically as a pesticide in orchards.[6] Although organic arsenic is thought to be less toxic, it generally has higher mobility within the environment, and less information is available on organic arsenic chemistry compared to that of inorganic arsenic.[1, 9] Table 2 shows examples of none volatile organic forms of arsenic found within soil environments and relevant organic arsenic contaminates.

Table 2. Examples of environmentally relevant organic arsenic compounds at pH 7

Name of arsenic compound	Oxidation state	Structure
Monomethylarsonic acid (MMA)	As (V)	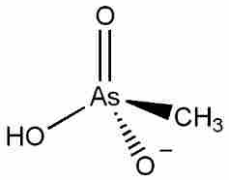
Dimethylarsinic acid (DMA)	As (V)	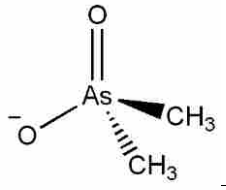
4-hydroxy-3-nitrobenzenearsenic acid (Roxarzone)	As (V)	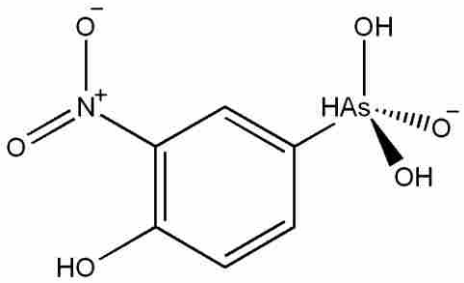

1.1.3 Arsenic cycling pathways: redox and methylation chemistry

The two major oxidation states of inorganic arsenic found in natural environments are As(III) and As(V) with oxidation states of -3 and 0 are also being possible.[2, 9] Under natural soil and neutral water conditions, inorganic As(III), arsenite, exits as a neutral species (pKa: 9.23, 12.1, 12.7).[9-10] Conversely, arsenate exits as an anion (pKa: 2.22, 6.98, 11.53) and is predominant under oxidizing conditions.[9-10] Within soils, arsenate dominates in the oxidizing conditions of the upper layers while arsenite will dominate in the reducing conditions of lower layers.[9] The anionic charge present on arsenate results in electrostatic attraction between arsenate and cationic active soil components such as iron oxides, resulting in adsorption.[3, 9] Arsenite lacks a charge under environmental conditions, which results in high mobility within soils compared with arsenate.[9] Inorganic arsenic has the ability to transform into the organic form through natural methylation to either monomethylarsonic acid (MMA) (pKa: 3.6, 8.2) or dimethylarsinic acid (DMA) (pKa:

6.14).[2] The Challenger Mechanism is one example of arsenic methylation. It produces MMA and DMA, as well as the volatile trimethylarsine (TMA) as a final product.[11]

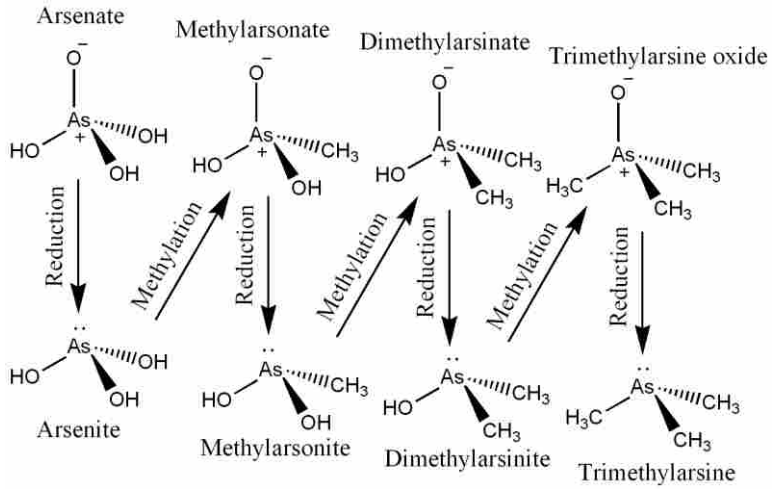

Figure 2. The Challenger mechanism for the biological methylation of arsenate.

1.2 Environmental regulations of arsenic in soils and drinking water

Arsenic is classified by Environment Canada as a Schedule 1 Substance and is regulated under the Canadian Environmental Protection Act (CEPA).[12] This classification is a result of the high carcinogenic and toxicological, of arsenic effects on humans.[12] Human exposure to arsenic from soil and water is comparably low in the developed world compared to the intake from food, particularly fish and shellfish.[12] However, intake from non-food sources can surpass food intake if the affected population is close to a point source.[12] Regulations on arsenic in drinking water vary depending on conditions within a country, including levels of arsenic naturally present in drinking water and the practical challenges associated with trying to achieve a particular concentration level.[13] Health Canada mandates a 0.010 mg/L maximum acceptable concentration (MAC) of arsenic in drinking water, which is identical to the limit set by the World Health Organization

(WHO).[12] Conversely, 0.050mg/L has been recommended and adopted as a guideline for many countries in the developing world, including Bangladesh.[13]

For soils, the average concentrations measured in Canada range from 4.8 to 13.6 mg/kg and are not regarded as high contributors to exposure, with the exception of specific contaminated sites such as the above-mentioned Giant Mine in North West Territories.[12]

1.2.1 Methods for removal of arsenic from drinking water

There are numerous methods for the removal of arsenic from drinking water, with a typical process consisting of a pretreatment step and a polishing step.[12] The pretreatment step is designed to oxidize arsenic (III) to arsenic (V). This is performed because neutral As(III) is more difficult to remove than anionic As(V). Potassium permanganate, hydrogen peroxide, ozone, chlorine and ferric chloride can all be utilized for the oxidation of As(III) to As(V).[12] In Canada, the most common method for removal of arsenic and subsequent polishing of arsenic in municipal systems is to use adsorptive media such as activated alumina or iron oxide.[12] Other methods include, but are not limited to: reverse osmoses, lime softening, ion exchange, coagulation/filtration and manganese greensand filtration.[12, 14] By contrast, short-term solutions are often necessary in the developing world to limit exposure of populations to contaminated water, which can exceed 1000 µg/L in some cases.[13, 15] One example is to use shallow dug wells, which can provide water that is still contaminated (from 10 µg/L to 50 µg/L) but to a lesser extent than deeper groundwater.[13] Although these short-term solutions are not removal processes, they have the advantage of being inexpensive and easy to implement.

1.2.2 Analytical methods for the detection and analysis of arsenic in drinking water

Among the various analytical methods available for the detection of arsenic, a fundamental distinction exists between methods that can provide information on the chemical speciation of arsenic and methods that can only detect total arsenic. Given that the mobility, toxicity and bioavailability of arsenic are all dependent on the speciation in which it exists, information on the speciation of arsenic is one important variable (in conjunction with other complex environmental factors) for predicting these behaviors. Chromatographic techniques such as High Performance Liquid Chromatography (HPLC) using an ion exchange column, or Gas Chromatography (GC) can be used to separate arsenic species for detection.[16] One such method detection that allows for the differentiation of As(III) and As(V) is hydride generation atomic absorption spectrometry.[16] The drawback of speciation-sensitive techniques is that they often cost more or require more expertise to run than simpler methods that test only for total arsenic.

1.3 Organic matter in soil

Natural organic matter (NOM) is an important component of soils, particularly topsoil, as it can make up a significant proportion of soils and play a role in many types of chemical and biological reactions. Organics high in carboxylic acid groups, such as citric acid, are naturally found within soils and can be introduced through secretion by plant roots and microbes.[17-22] This process is hypothesized to enhance the bioavailability of nutrients, such as iron and phosphorus, so that they may be up taken by the organism.[22] In addition to the secretion, organics are also introduced by the decaying biological matter and can serve as an agricultural supplement.[20, 22] NOM also acts as a food source for helpful microscopic organisms and aids in water retention, further enhancing soil fertility.[22]

The functional groups and size of NOM are highly variable and are characterized as either fulvic acid, humic acid or humin depending on molecular weight. Organic matter is often found at a high concentration within the upper layer of soil, referred to as the O-horizon (a soil horizon being a distinct layer of soil).[18] Once introduced, organic matter retention in soils are heavily correlated with the presence of active soil components, specifically iron and aluminum oxide content.[18, 21] It is reported in Lalonde et al. that an esstimated 21.5 ± 8.6% of the worlds sedimentary organic carbon is associated with iron.[21] The adsorption of organic matter to geosorbents in soils such as aluminum and iron oxides is correlated with the long-term retention of organic matter within soils, as well as the long-term storage of carbon in deeper soil horizons via burial.[19-20] This process has implications for understanding global carbon cycling.[20] Removal of organic matter from soils normally occurs either by biominneralization to CO_2 or through errosion/weathering, which causes the leaching of organic matter from soil into ground or surface water.[22]

1.4 Role of organics in controlling the environmental fate of arsenic compounds

The mobility of arsenic within the environment is often determined by its ability to bind to active soil components such as mineral clays and metal oxides.[1] This binding process can be altered by the presence of other reactive substances such as natural organic matter (NOM). Prior research indicates a positive correlation between the presence of NOM and an increase in the mobility of arsenicals.[23-30] Mladenov et al. report an increase in dissolved arsenic concentration in deep groundwater with high concentrations of NOM.[27] This study uses isotope C-13 NMR and bulk analysis techniques to study fulvic acid isolates and the concentration of arsenic in surface and ground waters.[27]

NOM influences arsenic mobility in one of three primary ways: First, NOM occupy potential binding sites for arsenic, thus increasing the portion of arsenic within the dissolved phase.[25-27] Second, adsorbed natural organic matter can reverse the electronic charge of the geosorbent surface from positive to negative, thus creating repulsive forces against the binding of anionic arsinicals.[24] Third, the natural organic matter may form a dissolved-metal bridging complex with arsenic, thus drawing more arsenic into the dissolved phase.[23, 27-30]

There are two drawbacks to using IR techniques to study NOM from field samples regardless of source location. First, NOM produces broad bands in the IR region due to the high degree of variability among functional groups. These broad IR bands make it unclear what specific complexes are being formed with the surface of the geosorbent and by what mechanisms they form.[24, 26] Second, the complexation reactions between arsenic and NOM further complicate the system, exacerbating the difficulty in determining the mechanisms of arsenic binding in the presence of adsorbed organics.[24, 26] An example of both effects is reported in Redman et al., wherein the effect of NOM on arsenic sorption to hematite is studied using attenuated total reflectance Fourier transform infrared spectroscopy (ATR-FTIR).[26] The author's report that the presence of NOM adsorbed to the surface of hematite greatly decreases the kinetics of adsorption of arsenic to hematite.[26] As a result of this complexity in reaction mechanism and IR spectrum, it is necessary to utilize compounds that can serve as analogs for NOM. To this end, previous studies have examined the interaction of low molecular weight (LMW) organics with geosorbents. These model organic compounds may also have environmental implications regarding arsenic mobility in addition to serving as model organics.[31] Oxalic acid, citric acid and pyrocatechol are all used as model organic compounds due to their ability to serve as analogs to functional groups on NOM.

Specifically, both oxalic and citric acid possess carboxylic acid functional groups, while pyrocatechol itself represents phenolic compounds.

1.4.1 Bulk/batch studies

In Wang and Mulligan, batch experiments were performed using the three low molecular weight organics: succinic acid, L-aspartic acid, and L-cysteine with Pb–Zn mine tailings containing arsenic and a significant amount (23%) of iron.[31] These experiments involved shaking the mine tailings for 24-h with distilled water and organic additives at each tested pH value.[31] Wang and Mulligan reported that the addition of organics inhibits the mobilization of arsenic under acidic conditions, but increase mobilization under neutral conditions.[31] The mobility of arsenic species was shown to be heavily correlated with iron mobility in the tested samples.[31] It is theorized that co-mobilization may have been a factor in increasing arsenic mobilization.[31] Other bulk studies report a binding affinity between model organic compounds and iron oxides, including pyrocatechol, citric and oxalic acid, the same organics utilized in this study.[32-33] Evanko and Dzombak (1998) performed batch experiments which involved reacting goethite individually with 28 simple organic acids as well as Aldrich humic acid over a range of pH values and measuring percent of organic adsorbed to determine relative binding affinities.[32] It was reported that the adsorption of model organics to goethite increased at low pH and decreased at high pH.[32] This trend correlates with the charges of goethite and the reacting organic compound, resulting in electronic repulsion when both species are anionic.[32] It was reported that adjacent carboxylic or phenolic groups, or an ortho-phenolic carboxylic acid pair, increase adsorption compared with similar organics.[32] Yeasmin et al. preformed batch experiments using ^{14}C-labelled oxalic and citric acid, as well as four amino acids with five different minerals including goethite.[33] Batch experiments were complemented with surface sensitive attenuated total reflectance Fourier

transform infrared spectroscopy (ATR-FTIR) experiments and the Freundlich equation applied to adsorption results.[33] These batch experiments were limited to comparing the adsorption of different combinations of geosorbent and organic acid.[33] It was reported that both citrate and oxalate have high adsorption to ferrihydrite and goethite compared to other geosorbents, with citrate having Freundlich constants of 17.01 and 9.57 for ferrihydrite and goethite, respectively, compared to oxalate having 1.02 and 0.55.[33] The Freundlich equation is similar to the Langmuir adsorption model employed in this work (section 3.7), with the difference being that former assumes a multi- rather than a mono-layer. It was also reported that ferrihydrite has the highest Freundlich constant for all organic acids, with the exception of lysine owing to its positive charge.[33]

1.4.2 Surface sensitive infrared spectroscopic studies

A major drawback of all batch studies is that environmentally relevant interactions between the dissolved phase and the solid geosorbent surface are not studied directly, making these studies less environmentally relevant. In order to probe this solid/liquid interface, surface sensitive techniques must be used. Yeasmin et al. preformed both batch and surface-sensitive experiments with model organic compounds and minerals. The results from the batch experiments are described above in section 1.4.1.[33] The results from the surface sensitive ATR-FTIR experiments produce adsorption spectra for each organic acid/mineral combination.[33] It was reported that the adsorption of both oxalate and citrate to iron oxide and kaolinite surfaces results in the formation of a combination of inner-sphere and outer-sphere complexes, with binding occurring between deprotonated carboxylic acids and the iron/aluminum binding sites present on the mineral surface.[33] Persson and Axe used ATR-FTIR combined with density functional theory calculations and extended x-ray absorption fine structure spectroscopy to study oxalate binding to goethite as a function of pH.[34] It was reported that oxalate forms a combination of outer-sphere and inter-

sphere complexes with goethite with outer-sphere complexes being favored at higher pH values.[34] Yang et al. studied the adsorption of pyrocatechol to goethite using ATR-FTIR, as well as performing 2D IR correlation analyses and quantum chemical calculations.[35] It was reported that pyrocatechol is able to form an inner-sphere complex of both mononuclear monodentate and binuclear bidentate with the surface of goethite, where the binuclear bidentate complexation was favored as surface coverage increased.[35] Hug and Bahnemann, used ATR-FTIR to study the binding interactions between three dicarboxylic acids (oxalic acid, malonate, and succinate) and three metal oxides, including the iron oxide lepidocrocite.[36] The results indicated that oxalate forms an inner-sphere bidentate complex with lepidocrocite that can either take the form of a binuclear bridging or mononuclear chelating complex.[36] The overall binding affinity for the organic acids reached its maximum at lower pH (specifically, pH 3 for oxalic acid) with higher pH values causing desorption of the metal oxide being studied.[36] Gulley-Stahl et al. studied pyrocatechol adsorption on hematite films using ATR-FTIR as a function of pH. It is reported that under basic a neutral conditions pyrocatechol promoted dissolution of hematite attributed to the formation of inner-sphere bidentate mononuclear with the surface of hematite.[37]

Previous studies have been carried out in the Al-Abadleh research group that used ATR-FTIR to study the interaction between various organic and inorganic arsenicals and the iron-oxides hematite and goethite.[3, 38-39] Arts et al. conducted ATR-FTIR experiments studying the adsorption kinetics of arsenate and p-arsanilic acid (pAsA) to the surface of hematite nanoparticles.[3] It was reported that arsenate is able to form a strong inner-sphere bidentate binuclear complex with a k_{ads1} of 0.66 ± 0.07 min^{-1} mM^{-1}, while pAsA was reported to form an inner-sphere monodentate complex with the surface of hematite with a k_{ads1} of 0.42 ± 0.04 min^{-1} mM^{-1}.[3] The same ATR-FTIR experiments were conducted by Tofan-Lazar and Al-Abadleh to study the adsorption of

dimethylarsinic acid (DMA) to goethite and hematite.[38] The formation of outer-sphere complexes between DMA and both iron−(oxyhydr)oxides was reported with a k_{ads1} of 0.4 ± 0.15 min^{-1} mM^{-1}.[38] The Al-Abadleh group also performed thermodynamic studies for arsenate, DMA and monomethylarsonic acid (MMA). Through a combination of ATR-FTIR experimental results and triple-layer surface complexation modeling, $logK_{eq}$ values for adsorption to hematite nanoparticles were reported to be 12.93 ± 0.06 for arsenate, 7.30 ± 0.04 for DMA, and 11.27 ± 0.05 for MMA.[40] Sabur et al. also report that MMA forms a combination of strong inner-sphere bidentate binuclear and monodentate complexes with the surface of hematite at room temperature.[40] The studies referenced in section 1.4.2 are all examples of the effectiveness of ATR-FTIR in obtaining thermodynamic and kinetic information on complexation occurring at the solid/liquid interface.

2 Overview of thesis objectives

The objectives of this thesis are to utilize ATR-FTIR to: (1) determine the structure of model organics adsorbed to the surface of hematite and goethite nanoparticles, (2) quantify the adsorption thermodynamics of model organics to the surface of hematite from pH envelope and adsorption isotherm studies, (3) quantify the adsorption and desorption kinetics of model organics on hematite, and (4) to quantify the adsorption kinetics of arsenicals to hematite that has been pre-exposed to organics relative to clean surfaces.

3 Experimental and Modeling Approach

3.1 Reagents

Each solution was prepared used 18 MΩ-cm Millipore water with 10 mM KCl added to adjust the ionic strength (potassium chloride, 99%+, GR ACS, EMD). The oxalic acid solutions were made using: oxalic acid dihydrate (Oxalic acid dihydrate, 99%+, ACS reagent, Sigma-

Aldrich) and mixed on a stir plate until the solid oxalic acid had dissolved. The pH of the newly formed solution was around 3 and was raised using concentrated NaOH solution (sodium hydroxide, 99%+, GR ACS, EMD). For experiments, involving citric acid (citric acid monohydrate, 99%+, ACS reagent, Alfa Aesar) or pyrocatechol (pyropyrocatechol, 99%+, C9510-100G, Sigma-Aldrich) the same procedure was followed with the resulting solutions pH being around 3 and 6, respectively. The arsenic solutions were prepared using sodium arsenate (sodium arsenate, $AsO_4HNa_2 \bullet 7H_2O$, ACS reagent, J.T. Baker, used as received), and DMA (sodium cacodylate trihydrate, $C_2H_6AsO_2Na \bullet 3H_2O$, Sigma-Aldrich, used as received) added to 10 mM KCl and mixed on a stir plate until the solid had fully dissolved. Protective equipment was worn when handling arsenic compounds including gloves and a gas mask. This was done in order to minimize the risk of exposure, as both substances are human carcinogens. The pH of both resulting arsenic solutions was just above pH 7 and was lowered to pH 7 with dilute HCl solution (hydrochloric acid, ACS, 6 N, Ricca Chemical).

3.2 Characterization of hematite nanoparticles

The hematite nanoparticles used in this study were sent to McMaster University where transmission electron microscopy (TEM) images were taken. Figure 3 is a TEM of hematite nanoparticles showing size and shape.

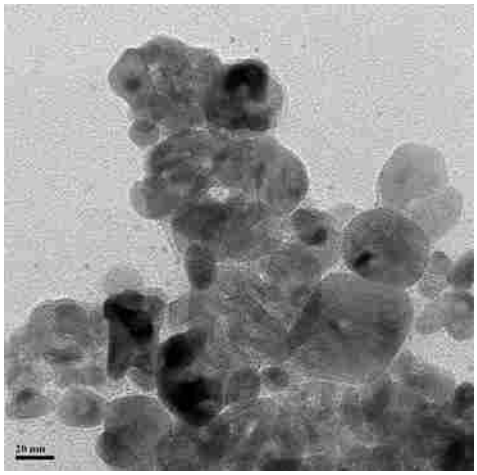

Figure 3. TEM image of hematite nanoparticles used in this study. [The scale bar corresponds to 20 nm.]

Average particle size of hematite particles was measured to be 39 ± 11 nm. These measurements were performed by measuring the diameters of hematite particles on physical printouts of multiple TEM images, referencing these measurements to the scale bar on each image, and averaging the referenced particle sizes. Other analyses performed includes the determination of the iso-electric point of hematite (pH 8.45) and the surface area 54 m^2/g per gram. Characterization of goethite nanoparticles was carried out previously in Tofan-Lazar and Al-Abadleh.[38]

3.3 Film preparations on ATR-FTIR crystal

A fresh hematite film was deposited on to the ZnSe ATR-FTIR crystal before each experiment. The mass of each hematite sample is 6 mg, which was measured and added to a glass vial (α-Fe_2O_3, 98%+, US Research Nanomaterials, Inc.). Following this, 0.91 mL 18 MΩ-cm Millipore water and 0.39 mL ethanol ethyl alcohol, (anhydrous, denatured, 85% ethanol, 14.3%

methanol, Anachemia) were then added to the same vial as the hematite. The glass vial was then sonicated for one hour to fully disperse the hematite particles throughout the solution. After sonication, the film was deposited across the ZnSe ATR crystal using a pasteur pipet so that the solution was evenly distributed. The film was deposited a night before to dry for the experiment the following day. Around 18 hours pass between when film preparation and the experiment. For experiments involving goethite (iron(III) hydroxide nano rods, 99+%, Nanostructured and Amorphous Materials Inc.), the same procedure was used but using 16 mg of goethite.

3.4 Experimental Procedure:

3.4.1 Principle of ATR-FTIR as a surface sensitive technique

The IR spectrometer used in this study is a Nicolet 8700 spectrometer (Thermo Instruments) equipped with an MCT detector and a HATRPlus accessory (Pike Technologies). The ATR cell has a ZnSe internal reflection element (IRE) (80×10×4 mm, 100 μL) crystal mounted within. The IR beam enters the ZnSe crystal at a 60° degree angle where it undergoes multiple internal reflections. Each time the light interacts with the sample, an evanescent wave is produced which is partially absorbed by the sample at the interface with the crystal. The attenuated evanescent wave is bounced back to the crystal and then hits the detector. This produces a single beam spectrum that can be referenced to another single beam spectrum creating an absorbance spectrum. The main advantage of using ATR-FTIR, which allows for probing reactions taking place at the solid-liquid interface. An overview of the use of ATR-FTIR in studying the liquid/solid interfaces can be found in Hind et al. [41]

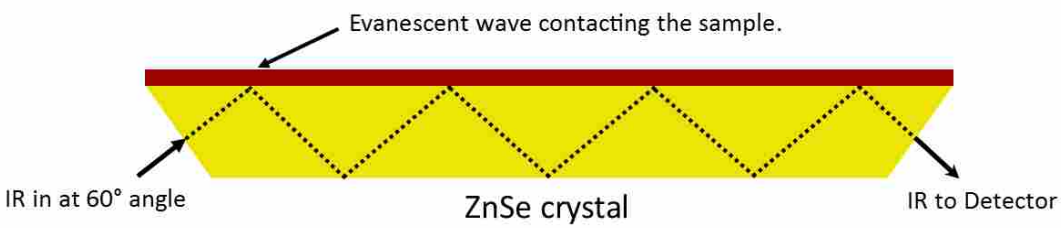

Figure 4. Diagram of ATR-FTIR crystal in the flow cell.

3.4.2 Calibration curves from spectra collected for aqueous phase species

Aqueous phase calibration curves were generated by running a series of increasing concentration of oxalate, pyrocatechol, citrate, iron oxalate, DMA, or arsenate solutions over a clean ZnSe ATR flow cell (no hematite or goethite film present). Spectra were collected using OMNIC for the dry ZnSe, background KCl solution and after each consecutive concentration. Upon completion, each sample aqueous phase spectrum was referenced to the dry ZnSe spectrum. Then using spectral math (see appendix C), each aqueous phase species absorbance spectra was subtracted from the background KCl absorbance spectrum referenced to dry ZnSe. This was done to properly subtract out water absorbance from the aqueous phase species absorbance spectra and isolate the absorbance from the species being studied.

3.4.3 Adsorption and desorption kinetics using ATR-FTIR

At the start of the experiment, 10 mM KCl at pH 7 was flown over the hematite film for 90 min with a single beam spectrum recorded at 90 min. Following the initial KCl flow, 1 mM, at pH 7 organic solution was flown for 80 min. Following the 1.0 mM organic solution, either 1.0 mM arsenate, 1.0 mM DMA or 10 mM KCl were flown for 80 min. Control experiments were also conducted where 1 mM arsenate or DMA flown directly after the initial 90 min KCl. The flow rate used in all experiments was 2 mL/min as measured directly by a 5 mL volumetric cylinder located

at the end of the output flow tube. Using macros basic (see appendix A), 50 single beam spectra were recorded for the first 5 min of flow time of an organic solution, or 40 single beam spectra for the first 10 min of an arsenical solution. After the first 5 min or 10 min respectively, single beam spectra were recorded manually every 5 min until 80 min had passed, at which time, either the next solution was flown or the experiment ended. Every single beam spectrum was referenced to the initial single beam spectrum recorded after 90 min of KCl flow to generate the absorbance spectra reported herein (see appendix B). Adsorption and desorption kinetics curves generated from baseline-corrected peak heights plotted versus reaction times were created using peak heights from maximum peak height wavenumber (e.g. if there is a shift in wavenumber of maximum peak height then the wavenumber at which the peak of measurement is made also shifts).

3.4.4 Adsorption isotherm studies using ATR-FTIR

At the start of the experiment, 10 mM KCl at pH 7 was flown over the hematite film for 90 min with a single beam spectrum recorded at 90 min. Following the initial KCl flow, pH 7 organic solutions with concentrations starting at 1×10^{-6} M up to 1×10^{-3} M were flown for 30 min each. The flow rate used in all experiments was 2 mL/min as measured directly by a 5 mL volumetric cylinder located at the end of the output flow tube. Every single beam spectrum was referenced to the initial single beam spectrum recorded after 90 min of KCl flow to generate the absorbance spectra reported herein (see appendix B).

3.4.5 pH envelope studies using ATR-FTIR

At the start of the experiment, 10 mM KCl at pH 7 was flown over the hematite film for 60 min with a single beam spectrum recorded at 60 min. Next, 10 mM KCl at pH 9 was flow for 30min with a spectrum collected after 30min. Following the initial KCl flow, 0.1 mM organic

solutions with pH starting at 9 and going down in intervals of 0.5, down to pH 5, were flown for 30 min each. The flow rate used in all experiments was 2 mL/min as measured directly by a 5 mL volumetric cylinder located at the end of the output flow tube. Every single beam spectrum was referenced to the single beam spectrum recorded after 30 min of pH 9, KCl flow to generate the absorbance spectra reported herein (see appendix B).

3.5 Modeling of adsorption kinetics

A baseline-corrected peak height analysis was performed on ATR absorbance spectra using Macros Basic (Appendix B). Baseline-corrected peak height measurements attributed to surface complexes, at the wavenumber of specific spectral features, were used as an accurate measurement of surface coverage. The reaction to be analyzed is between aqueous analyte species and empty reactive sites on the surface of the geosorbent film, shown in reaction 1.

$$[MO]_{aq} + \text{empty site} \underset{k_{des}}{\overset{k_{ads}}{\rightleftharpoons}} [MO]_{ads} \quad \ldots (1)$$

In the above equation, [MO] is the concentration of model organic, k_{ads} is the adsorption rate constant, and k_{des} is the desorption rate constant. The Langmuir adsorption model can be used to analyze the kinetics and thermodynamics of reaction 1. The assumption within the Langmuir adsorption model is that a homogeneous surface is formed and that reactive surface sites are identical. The Langmuir kinetic adsorption model, shown in equation 2, was used to analyze the collected peak heights in order to generate time dependent adsorption kinetic curves.

$$\theta(t) = b(1 - e^{-r_{obs}*t}) \ldots (2)$$

$$where, b = k_{ads1}\,[MO]_{aq}/r_{obs1}$$

$$and, r_{obs} = k_{ads}[MO] + k_{des}$$

$\theta(t)$ is a measure of surface coverage. Surface coverage is related to absorbance via the relation expressed in equation 3. Expanding the θ term in equation 3 with the measurement for surface coverage produces equation 4, which provides a measurement of baseline-corrected peak height absorbance.

$$\theta = \frac{A}{A_{max}} \ldots (3)$$

$$A = b'(1 - e^{-r_{obs}*t}) \ldots (4)$$

$$where, b' = A_{max} * b$$

Equation 4 is then linearized to produce equation 5 with b' being a collection of constants equal to absorbance in the plateau region of the adsorption kinetic curve.

$$\ln\left(1 - \frac{A}{b'}\right) = -r_{obs} * t \ldots (5)$$

Using equation 5, r_{obs} is equal to the slope of the least-squared fit of $\ln\left(1 - \frac{A}{b'}\right)$ plotted against adsorption time. The Langmuir adsorption kinetic adsorption model allows for the plotting of r_{obs} against aqueous analyte concentration to extract k_{ads} using equation 6.

$$r_{obs} = k_{ads}[MO]_{aq} + k_{des} \ldots (6)$$

3.6 Modeling of desorption kinetics

Desorption of model organics from the surface of geosorbents by the adsorption of aqueous arsenic species is shown in reaction 7 and can be described by the Langmuir kinetic desorption model shown in equation 8.

$$[As]_{aq} + [MO]_{ads} \xrightarrow{k_{des}} [MO]_{aq} + [As]_{ads} \ldots (7)$$

$$\theta(t) = \theta_0 e^{-k'_{des} * t} \ldots (8)$$

$$where, \theta = \frac{A}{A_{max}} \; and, \theta_0 = \frac{A_0}{A_{max}}$$

$$and, k'_{des} = k_{des} * [As]_{aq}$$

$\theta(t)$ and θ_0 are converted to absorbance values and linearized to produce equation 9.

$$\ln\left(\frac{A}{A_0}\right) = -\mathrm{k}'_{\mathrm{des}} * t \ldots (9)$$

A_0 equals the initial absorbance before the start of desorption. The initial observed desorption rate can be extracted by plotting $\ln\left(\frac{A}{A_0}\right)$ vs desorption time with the initial observed desorption being equal to the slope of the least-squared fit.

3.7 Modeling adsorption thermodynamics with the Langmuir model

The Langmuir adsorption model predicts a dynamic equilibrium between adsorbed and aqueous phase species, shown by reaction 1. According to the Langmuir adsorption model, the equilibrium constant K_{eq} for reaction 1 can be expressed by equation 10.

$$K_{eq} = \frac{\theta}{[MO](1-\theta)} \ldots (10)$$

θ is the surface coverage, which is a fraction of occupied sites on the surface of the geosorbent, while the $(1 - \theta)$ term is the fraction of empty sites. Equation 10 can be rearranged into the form of y=mx+b, using equation 3.

$$\theta = \frac{K_{eq}[MO]_{aq}}{1 + K_{eq}[MO]_{aq}}$$

$$or, \quad \frac{A}{A_{max}} = \frac{K_{eq}[MO]_{aq}}{1 + K_{eq}[MO]_{aq}}$$

$$or, \quad \frac{1}{A} = \frac{1 + K_{eq}[MO]_{aq}}{A_{max}K_{eq}[MO]_{aq}}$$

$$or, \quad \frac{1}{A} = \frac{1}{A_{max}K_{eq}} * \frac{1}{[MO]} + \frac{1}{A_{max}} \ldots (11)$$

K_{eq} can be obtained from the slope of the $\frac{1}{A}$ vs $\frac{1}{[MO]}$ plot using the y-intercept, equal to $\frac{1}{A_{max}}$.4

Results and Discussion

4.1 Characterization of Aqueous phase model organics using ATR-FTIR

Figure 5 shows the speciation curves for citric acid, oxalic acid, and pyrocatechol using the formulas shown in Appendix D. Citric acid at pH 7 contains a mixture of triply and doubly deprotonated species in about an 80-20 ratio. The species of oxalic acid at pH 7 is fully deprotonated, while pyrocatechol is fully protonated.

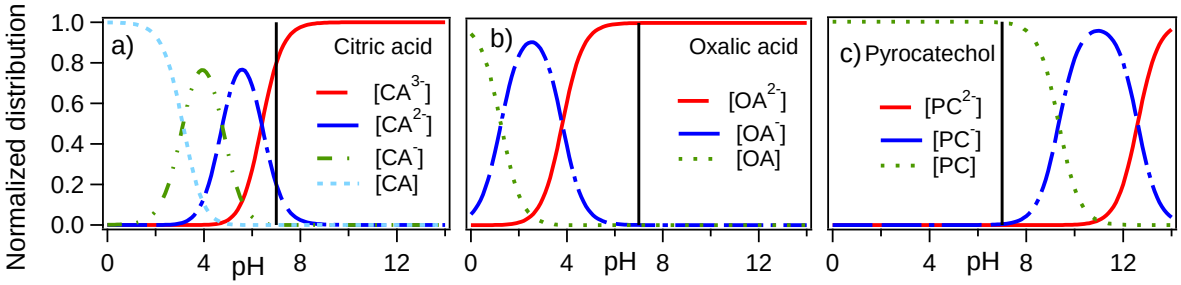

Figure 5. Speciation curves of (a) citric acid, (b) oxalic acid and (c) pyrocatechol. The solid black line on each plot indicates pH 7 conditions at which experiments were conducted.

To aid in the interpretation of surface interactions between model organics and iron−(oxyhydr)oxides films, bulk aqueous phase absorbance ATR-FTIR spectra were collected

using a clean ZnSe ATR crystal. Figure 6 shows the ATR-FTIR absorbance spectra of aqueous citrate, oxalate and pyrocatechol at pH 7.

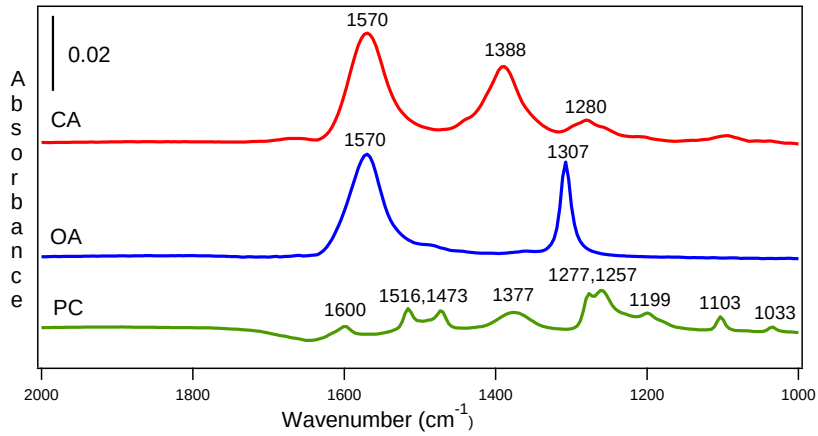

Figure 6. ATR-FTIR absorbance spectra of 0.1 M aqueous citrate (CA), oxalate (OA) and pyrocatechol (PC) at pH 7, I = 10 mM KCl. Clean ZnSe ATR crystal used (no film).

There are three main bands present in the aqueous spectra of citrate: 1570, 1388 and 1280 cm^{-1} assigned to $\nu_a(COO^-)$, $\nu_s(COO^-)$ and δ (CO_2^-) respectivly.[42] The aqueous spectra of oxalate contains two bands at 1307 and 1569 cm^{-1} which are assigned to $\nu_s(COO^-)$ and $\nu_a(COO^-)$, respectively.[43] The aqueous absorbance spectra of pyrocatechol is much more complicated than that of the two carboxylic acids, owing to the presence an aromatic ring. The bands present in the aqueous phase spectra of pyrocatechol are produced from the following vibrational modes: 1600 cm^{-1} from ν(CC) + ν(CO), 1516 cm^{-1} from ν(CC), 1473 cm^{-1} from ν(CC) and δ (CH), 1377 cm^{-1} from δ (OH) and ν(CC), 1277 and 1257 cm^{-1} from ν(CO) and δ (CH), 1199 cm^{-1} from ν(CO) and δ (OH), 1103 cm^{-1} from δ (CH) and 1033 cm^{-1} from δ (CH).[37, 44] The height of the most intense band from each organic compound was measured over a range of concentrations to generate aqueous phase calibrations curves for each model organic compound as a function of concentration. The bands selected for measurement were 1570 cm^{-1} for citrate and oxalate and

1257 cm^{-1} for pyrocatechol. Figure 7 shows spectra and calibration curves generated for each model organic compound in the aqueous phase. The slopes correspond to molar absorption coefficient (ε) multiplied by the path length of the ZnSe ATR crystal.

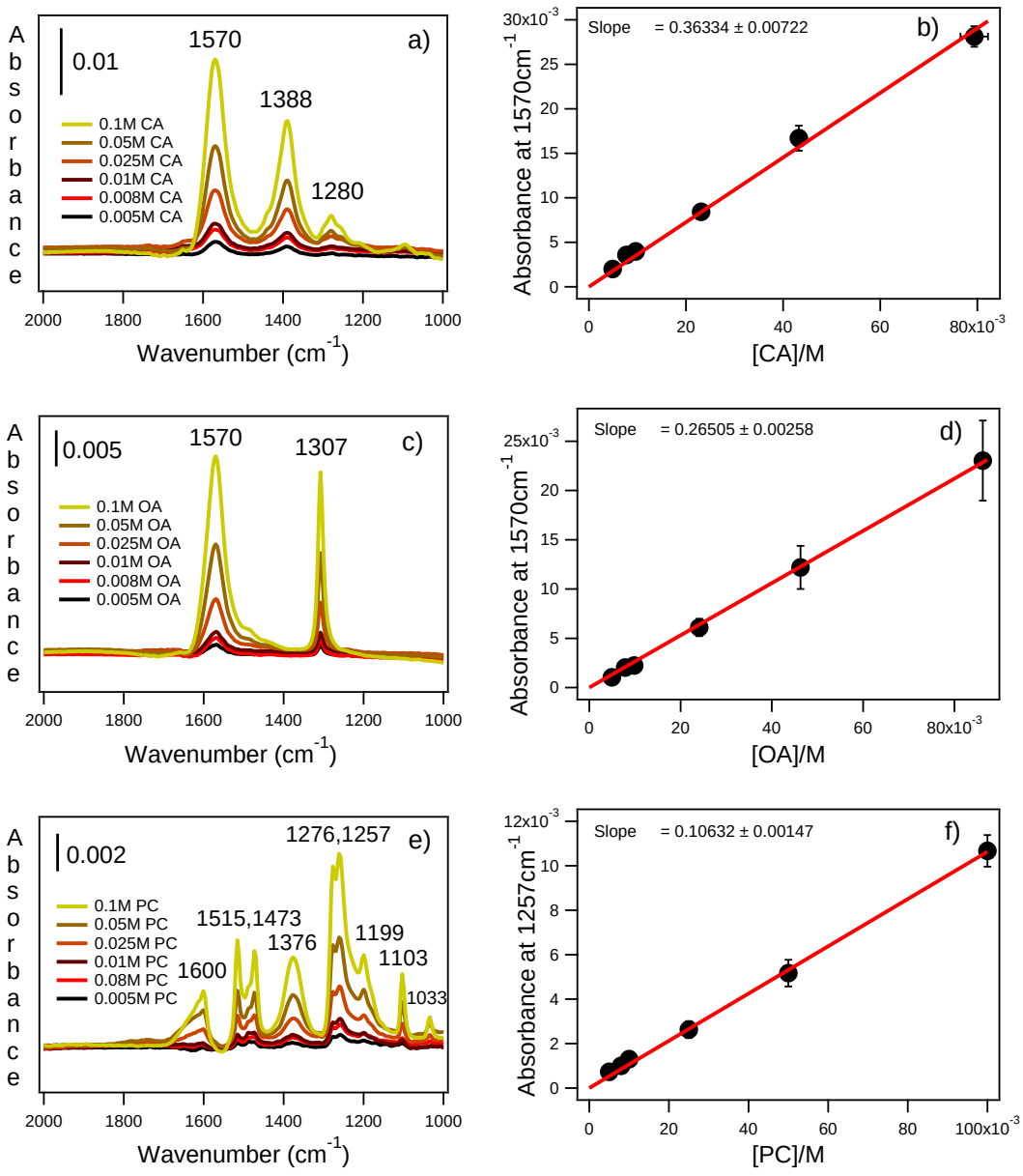

Figure 7. ATR-FTIR absorbance spectra of a) citrate, c) oxalate and e) pyrocatechol, respectively, over a concentration range of 0.005 to 0.1 M. b), d) and f) calibration curves generated from baseline-corrected ATR absorbances at 1570 cm^{-1} for citric and oxalate and 1257 cm^{-1} for pyrocatechol. Error bars are ±s.

The Beer–Lambert law states that measured absorbance is a function of the analyte concentration, path length and the molar absorption coefficient (ε), according to equation 12.

$$Beer-Lambert\ law: Absorbance = \varepsilon\ (M^{-1}\ cm^{-1}) * b\ (cm) * c\ (M) \ldots (12)$$

With an effective path length of 2.7×10^{-4} cm, the calculated molar absorption coefficients are 1345.7, 981.7, and 393.8 $cm^{-1}\ M^{-1}$ for citrate, oxalate, and pyrocatechol, respectively. Molar absorption coefficients are necessary for the conversion of baseline-corrected absorbance values attributed to a specific adsorbed analyte into surface coverage. The assumption made is that the molar absorption coefficient of an aqueous analyte is the same as its surface complex.

4.2 Adsorption thermodynamics of model organics using ATR-FTIR

4.2.1 Organic adsorption spectra and assignment

Thermodynamic adsorption isotherm experiments at pH 7 were carried out using aqueous solutions of model organics citrate, oxalate and, pyrocatechol flown over 6 mg hematite and 16 mg goethite films deposited across a ZnSe ATR crystal. The resulting ATR-FTIR absorption spectra for adsorbed species are shown in Figure 8 for 1 mM solutions.

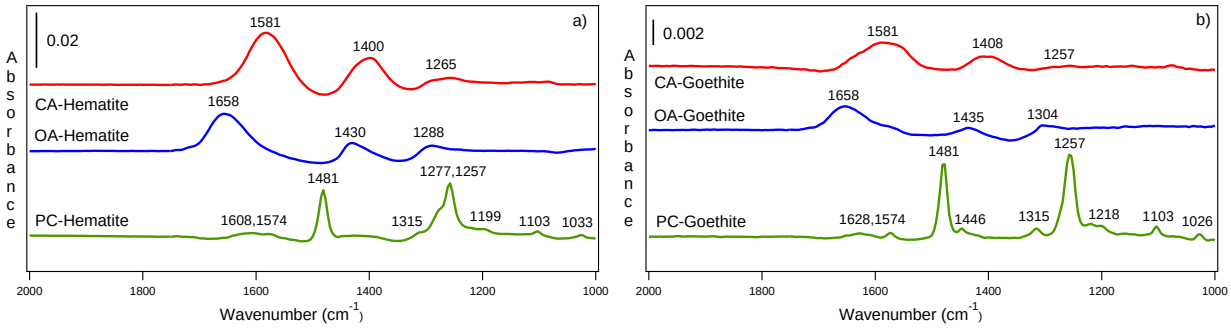

Figure 8. ATR-FTIR absorption spectra of adsorbed citrate, oxalate and, pyrocatechol (1 mM) at pH 7, I = 10 mM KCl, and 2 mL/min flow rate at room temperature on a) 6 mg hematite film and b) 16 mg goethite films after 80 min flow time.

The comparison between the aqueous phase spectra and the surface spectra of each model organic compound shows differences corresponding to the formation of surface complexes. The spectra of adsorbed citrate has shifted slightly compared to aqueous citrate. Although the peak at 1581 cm^{-1} in Figure 8 a) may be close to the $\nu_a(COO^-)$ aqueous peak at 1570 cm^{-1} shown in Figure 6, it is attributed to iron binding on the surface of hematite and goethite consistent with the formation of inner-sphere monodentate surface complex as shown in Figure 9.[42, 45] this assignment is also been supported by triple-layer or surface complexation modelling performed in Situm et al.[45]

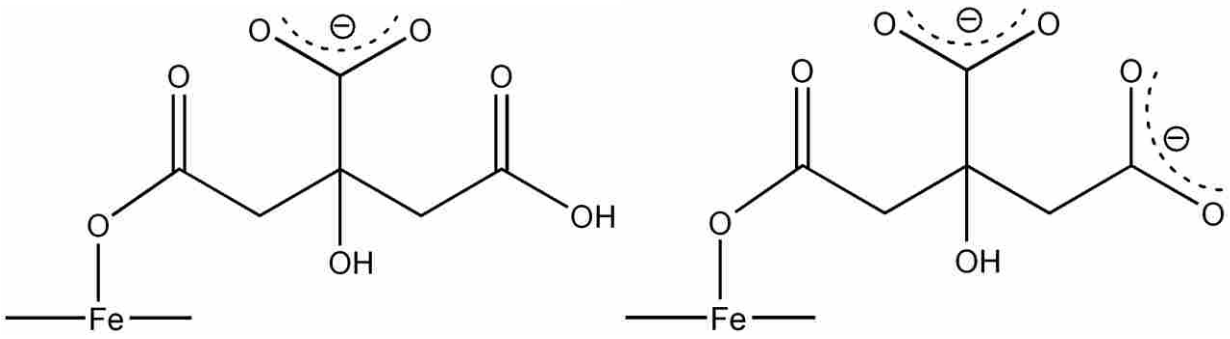

Figure 9. Complexes formed by citrate with the surface of hematite and goethite. (Left): protonated inner-sphere monodentate, (Right): deprotonated inner-sphere monodentate.

The three main bands in the absorption spectra of adsorbed citrate on hematite are slightly shifted but have almost the same assignments as aqueous citrate, with 1581 cm^{-1}, 1400 cm^{-1} and 1265 cm^{-1} assigned to $\nu(CO_2Fe)$, $\nu_s(COO^-)$ and δ (CO_2^-) respectivly.[42, 45] The band assignments of the absorption spectra of adsorbed citrate to goethite are the same as for hematite with the $\nu_s(COO^-)$ band at 1400 cm^{-1} shifted to 1408 cm^{-1} and the 1265 cm^{-1} δ (CO_2^-) band shifted to 1257 cm^{-1}.[42,

[45] A full listing of band assignments for citrate surface and aqueous phase citrate are in Table 3. Noerpel and Lenhart preformed bulk ATR-FTIR experiments reacting citrate with hematite nanoparticles and coupled these finding with surface complexation modeling and computational molecular modeling.[42] Situm et al. is the submitted publication done in collaboration with Dr. Sabine Goldberg at the U.S. Salinity Laboratory reporting the thermodynamic results found herein in combination with triple-layer surface complexation modeling.[45]

Table 3. Band assignments for ATR-FTIR absorption spectra of aqueous citrate and citrate adsorbed on hematite and goethite particles.

Band assignment	Aqueous spectra wavenumber (cm^{-1})	Surface spectra wavenumber (cm^{-1})		Reference
		Hematite	Goethite	
$\nu_a(COO^-)$	1570			[42, 45]
$\nu(CO_2Fe)$		1581	1581	[42, 45]
$\nu_s(COO^-)$	1388	1400	1408	[42, 45]
δ (CO_2^-)	1280	1265	1257	[42, 45]

The number of bands present in the ATR-FTIR absorbance spectrum of adsorbed oxalate has increased to three from two compared to aqueous oxalate, indicating that the symmetry of oxalate has been altered. The three main bands in the absorption spectra of adsorbed oxalate are 1658, 1430 and 1288 cm^{-1} on hematite and 1658, 1435 and 1304 cm^{-1} on goethite. The first two are assigned to $\nu(CO_2Fe)$, and 1288 cm^{-1} is assigned to $\nu_s(COO^-)$ bonding for hematite.[34, 45] The surface complexes formed by oxalate on the surface of hematite and goethite are shown in Figure 10.

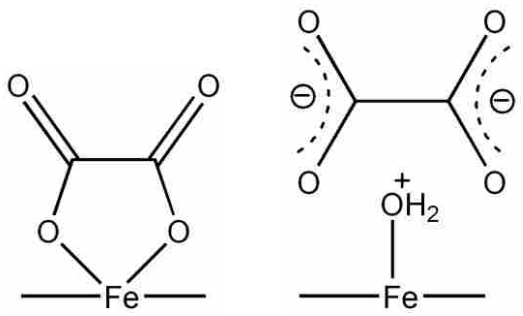

Figure 10. Complexes formed by oxalate with the surface of hematite and goethite. (Left): inner-sphere bidentate mononuclear, (Right): outer-sphere complex.

The band assignments of the absorption spectra of adsorbed oxalate on goethite are the same as for hematite with the $\nu(CO_2Fe)$ band at 1430 cm^{-1} shifted to 1435 cm^{-1} and the $\nu_s(COO^-)$ band 1288 cm^{-1} shifted to 1304 cm^{-1}.[34, 45] The initial surface complex assignment made was that the decrease in symmetry was consistent with the formation of an inner-sphere complex. Persson and Axe reported a five membered mononuclear bidentate complex is formed from adsorption of oxalate to goethite.[17, 34] Although an inner-sphere complexation is believed to form from oxalate binding to the surface of hematite, further analysis performed in Situm et al. through triple-layer surface complexation modelling indicates that outer-sphere complexation may occur simultaneously with inner-sphere complexation.[45] the assignment of outer-sphere complexation is also supported by kinetic results presented in sections 3.3 and 3.4 of this work. A full listing of band assignments for surface and aqueous phase oxalate are in Table 4.

Table 4. Band assignments for ATR-FTIR absorption spectra of aqueous oxalate and oxalate adsorbed on hematite and goethite particles.

Band assignment	Aqueous spectra wavenumber (cm^{-1})	Surface spectra wavenumber (cm^{-1}) Hematite	Goethite	Reference
$\nu_a(COO^-)$	1570			[34, 45]
$\nu_s(COO^-)$	1307	1288	1304	[34, 45]
$\nu(CO_2Fe)$		1658, 1430	1658, 1435	[45]

The largest change in the ATR-FTIR absorption spectra of pyrocatechol adsorbed to hematite and goethite compared with aqueous pyrocatechol is an increase in intensity of the band at 1257 cm^{-1} and the shift and large increase from the aqueous band at 1473 cm^{-1} to the surface band at 1481 cm^{-1}. The band at 1481 cm^{-1} is assigned to ν(COFe) along the band at 1257 cm^{-1}.[45] The shoulder at 1277 cm^{-1}, which is not present in pyrocatechol-goethite surface spectra, is assigned to ν(COFe).[45] A full listing of band assignments for surface and aqueous phase pyrocatechol are in Table 5.

Table 5. Band assignments for ATR-FTIR absorption spectra of aqueous pyrocatechol and pyrocatechol adsorbed on hematite and goethite particles.

Band assignment	Aqueous spectra wavenumber (cm^{-1})	Surface spectra wavenumber (cm^{-1}) Hematite	Goethite	Reference
ν(CC) + ν(CO)	1600	1608	1628	[35, 37, 44-45]
ν(CC) + δ (CH)	1516, 1473	1574	1574	[35, 37, 44-45]
ν(COFe)		1481, 1257	1481, 1446, 1257	[45]
δ (OH) + ν(CC)	1377	1315	1315	[35, 37, 44-45]
ν(CO) + δ (CH)	1277 and 1257	1277		[35, 37-38, 44-45]
ν(CO), δ (OH)	1199	1199	1199	[35, 45]
δ (CH)	1103	1103	1103	[35, 45]
δ (CH)	1033	1033	1026	[37, 44 45]

The decrease in bands associated with hydroxide vibrational modes and formation of *v*(COFe) suggests pyrocatechol forms a mixture of inner-sphere bidentate binuclear and inner-sphere monodentate complexs on hematite and goethite as shown in Figure 11.

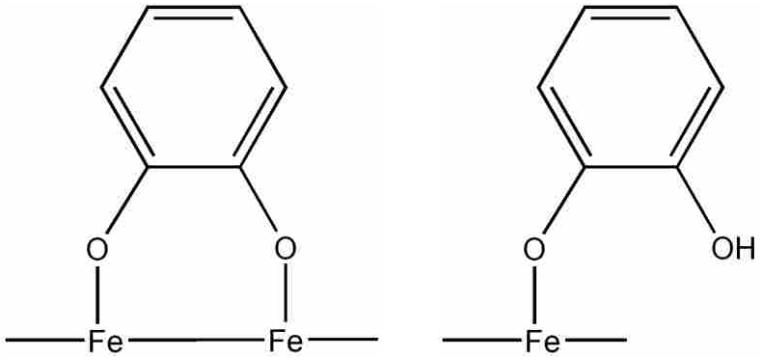

Figure 11. Complexes formed by pyrocatechol with the surface of hematite and goethite. (Left): inner-sphere bidentate binuclear, (Right): inner-sphere monodentate.

It should be emphasized that the surface complexation assignments for citrate, oxalate, and pyrocatechol on hematite are only proposed. To confirm these surface complexes, computational studies would need to be paired with this work in order to compare IR frequencies.

The negative bands that are present in model organic adsorption spectra in Figure 8 at 1485 and 1350 cm^{-1} have been attributed to carbonate desorption from the surface of hematite.[46] In order to confirm this assignment, nitrogen gas was bubbled through 10 mM KCl, at pH 7 then flown over an unreacted hematite film. Difference spectra from the nitrogen gas bubbling test are shown in Figure 12, which were obtained by referencing to the spectra collected after 1 min flow time.

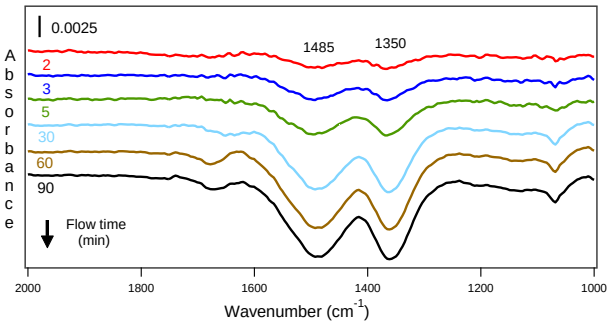

Figure 12. ATR-FTIR absorption spectra of surface carbonate desorption by nitrogen gas bubbled, at pH 7, and I = 10 mM KCl, using a 2 mL/min flow rate at room temperature on 6 mg hematite film.

The results of the nitrogen gas bubbling experiment show that the negative bands observed at 1485 and 1350 cm^{-1} are from loss of carbonate from the surface of hematite. The adsorption of organics was also carried out using with continued nitrogen gas bubbling. The resulting spectra of citrate, oxalate, and pyrocatechol adsorption are shown in Figure 13, and shows minimum interference from the signal of surface carbonate.

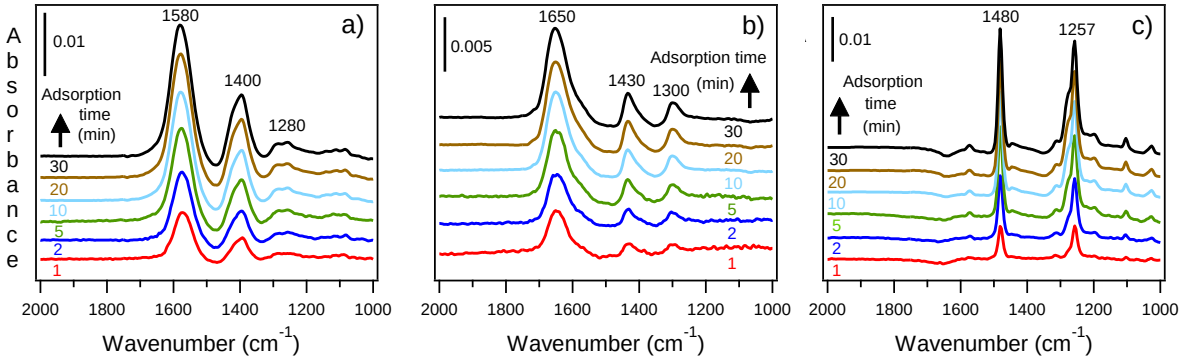

Figure 13. ATR-FTIR absorbance spectra of adsorbed a) citrate, b) oxalate and c) pyrocatechol respectively, collected as a function of concentration. Adsorption of model organics (1 mM) on 6 mg hematite film at pH 7, I = 10 mM KCl, and a 2 mL/min flow rate at room temperature and nitrogen gas bubbling.

4.2.2 Adsorption isotherms on hematite at room temperature

Adsorption isotherm experiments were conducted for the adsorption of model organics on hematite nanoparticles, with the goal of extracting equilibrium constants. Figure 14 shows the adsorption of model organics to hematite nanoparticles as a function of increasing concentration.

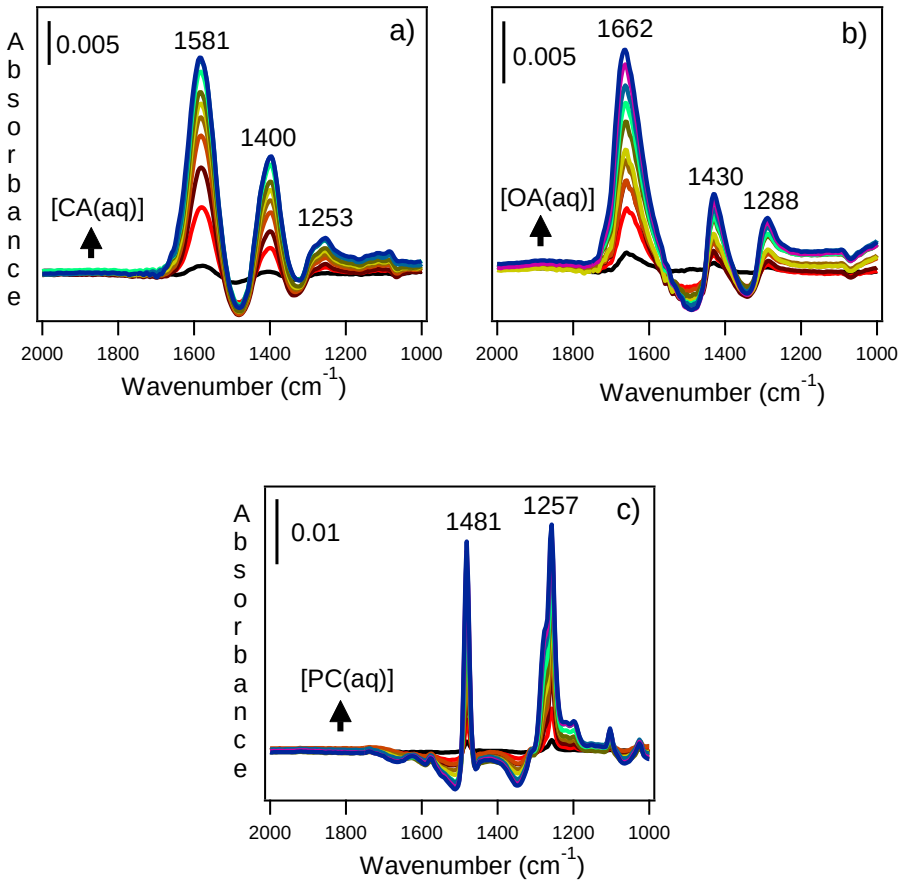

Figure 14. ATR-FTIR absorbance spectra of adsorbed a) citrate, b) oxalate and c) pyrocatechol respectively, collected as a function of time. Adsorption of model organics on 6mg hematite film at varying concentrations ranging from 10^{-6} M to 10^{-3} M (pH 7, I = 10 mM KCl, and a 2 mL/min flow rate at room temperature).

From the spectra in Figure 14, adsorption isotherm curves can be generated for the adsorption of model organics to hematite nanoparticles. Figure 15 shows Langmuir adsorption isotherms for the adsorption of model organics on hematite nanoparticles.

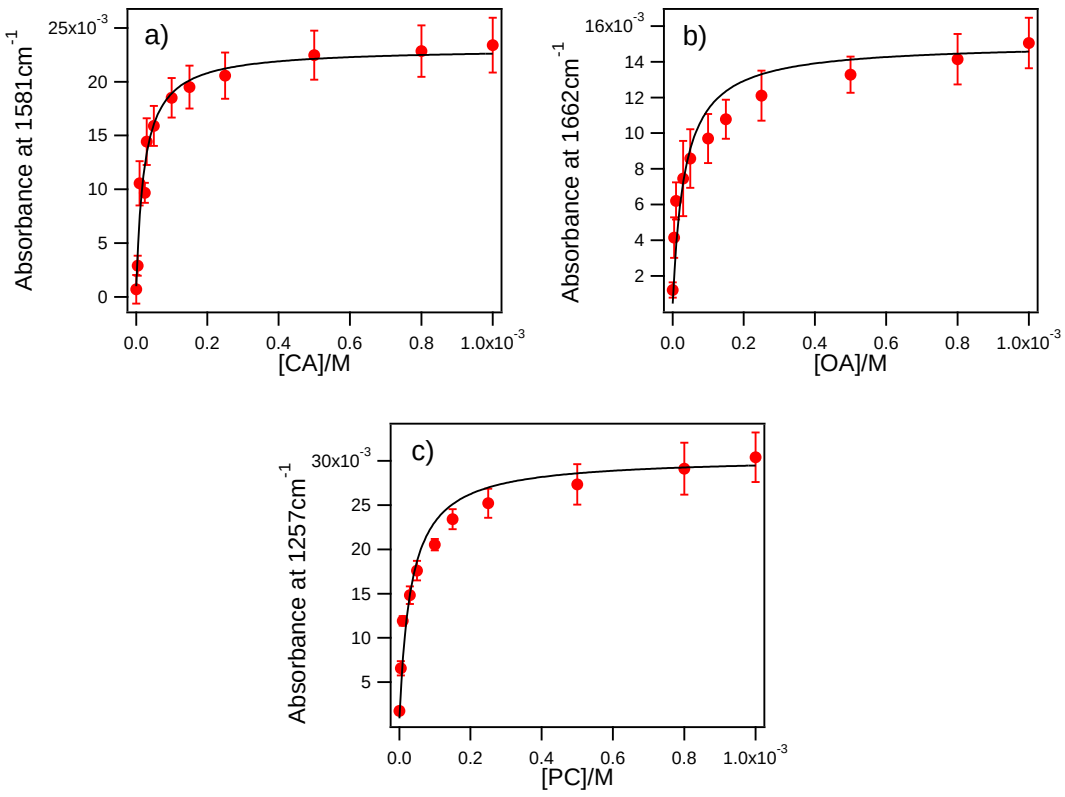

Figure 15. Adsorption isotherms of a) citrate b) oxalate and c) pyrocatechol on 6 mg hematite film at pH 7, I = 10 mM KCl, and a 2 mL/min flow rate at room temperature. The solid line represents the least-squares fitting of the 1-site Langmuir adsorption model: Absorbance = (Amax*K_{eq}*[organic]/M)/(1+K_{eq}*[organic]/M). Data points represent the average of three to four experiments. Error bars are ±s.

The solid line within Figure 15 represents the least-squared fitting of the one-site Langmuir adsorption model, the derivation of which can be found in section 3.7 of this work. Using equation 12, the results from Langmuir isotherms can be used with molar absorption coefficient (ε) values obtained from aqueous calibration curves in section 4.1 to calculate surface concentration from absorbance. Using equation 11 found in section 3.7, Langmuir adsorption isotherm curves were linearized to extract K_{eq} values for the adsorption of model organics to hematite nanoparticles.

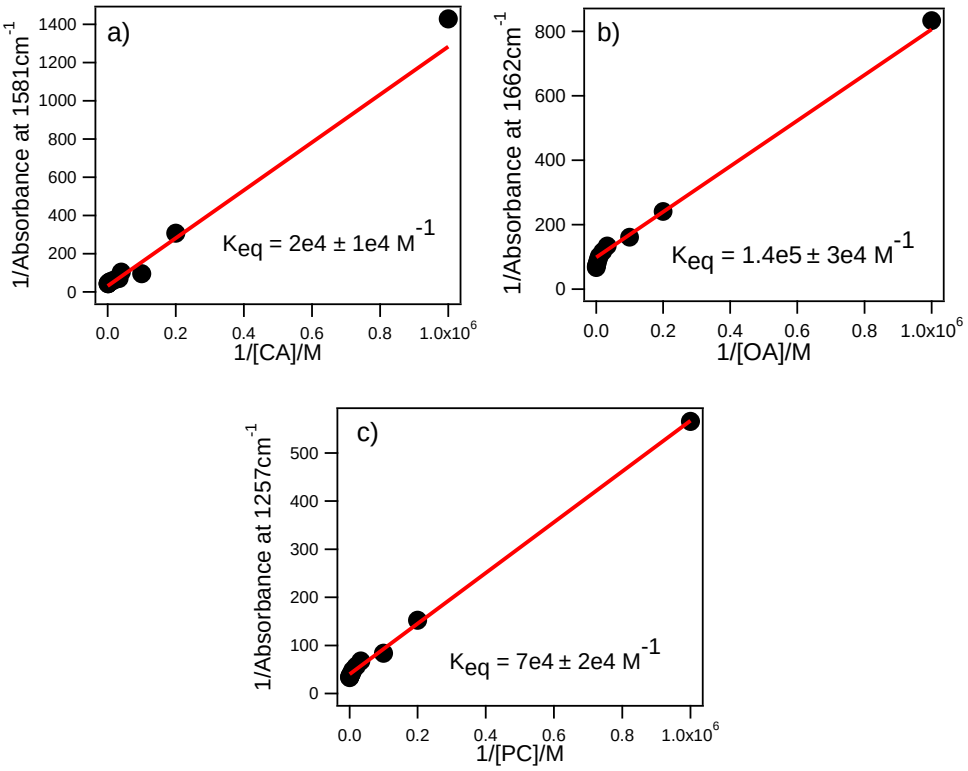

Figure 16. Linearized absorbances for the adsorption of a) citrate, b) oxalate and c) pyrocatechol on 6 mg hematite film as a function of concentration at pH 7, I = 10 mM KCl, and a 2 mL/min flow rate at room temperature. [Data points represent the average of three to four experiments and error bars were removed for clarity.]

Using the concentration of water (55.5 M) to eliminate M^{-1}, the $\log K_{eq}$ values were calculated from the K_{eq} values shown in Figure 16 and are shown in Table 6.

Table 6. $\log(55.5K_{eq})$ values calculated from K_{eq} values in Figure 15.

$\log K_{eq}$	Citrate	Oxalate	Pyrocatechol
Langmuir adsorption model, hematite, (This work)	6 ± 4	7 ± 1	7 ± 2
Triple-layer surface complexation model, hematite[45]	5.71	10.08	7.03
CD-Music model, goethite[47]	29.75	18.00	
CD-Music model, goethite[48]	39.6		
Diffuse double layer model, goethite[49]	13.004		

$\log K_{eq}$ values obtained from Langmuir adsorption model are compared to $\log K_{eq}$ values obtained from triple-layer surface complexation modelling preformed in Situm et al.[45] Also included in Table 6 are $\log K_{eq}$ values for model organic binding to goethite nanoparticles. Filius et al. (1997) and Geelhoed et al. (1998) are studies performed in the Van Riemsdijk group using the CD-MUSIC model to analyze the adsorption of oxalate and citrate to goethite.[47-48] The charge distribution (CD) multi-site complexation (MUSIC) model used by the Van Riemsdijk group considers surface complexes to have spatial charge distribution rather than being point charges.[50] Marcussen et al. preformed bulk phase experiments, reacting citrate with goethite nanoparticles and analyzing the results using diffuse double-layer surface complexation modelling to produce $\log K_{eq}$ values.[49] The surface complexation models described herein illustrates the wide variety of models available to describe surface complexation.

4.2.3 pH envelope curves on hematite and goethite

pH envelope adsorption experiments were carried out for model organics on hematite and goethite as described in section 3.4.5. Figure 17 shows absorbance spectra for model organics adsorbed to the surface of hematite.

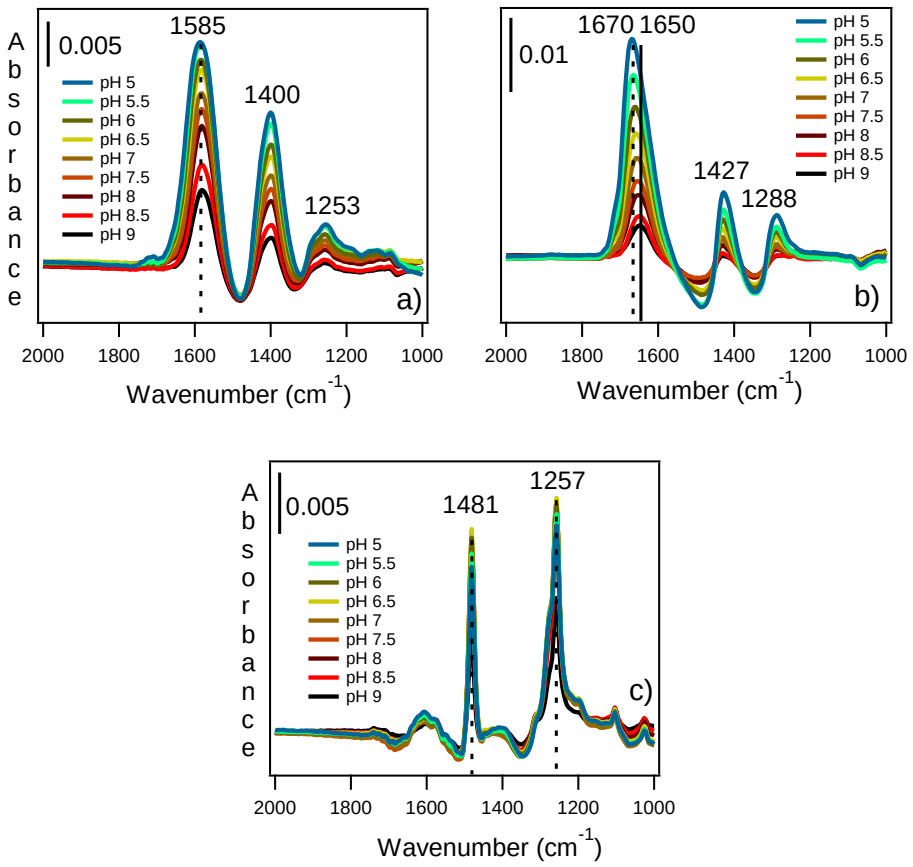

Figure 17. Adsorption of model organics (1 mM) on 6 mg hematite film at varying pH, I = 10 mM KCl, and a 2 mL/min flow rate at room temperature and nitrogen gas bubbling. ATR-FTIR absorbance spectrum of adsorbed a) citrate, b) oxalate and c) pyrocatechol respectively.

A peak shift from 1650 cm^{-1} to 1670 cm^{-1} was observed in the pH envelope absorption spectra of oxalate as pH is lowered from 9 to 5. Conversely, there was no observed shift in citrate and pyrocatechol absorbance spectra. One possible explanation for the observed shift in the absorbance spectra of oxalate is the fact that protonation of carboxylic groups on outer-sphere oxalate (Figure 10) reduces resonance, which increases double bound in adsorbed oxalate on positively-charged hematite surface. Another consequence of a decrease in pH is that the hematite surface develops a stronger positive charge that would increase the maximum adsorption of charged analytes to the surface of hematite. Figure 18 shows adsorption of model organics to

hematite nanoparticles as a function of pH, with peak height measurements taken at maximum peak height.

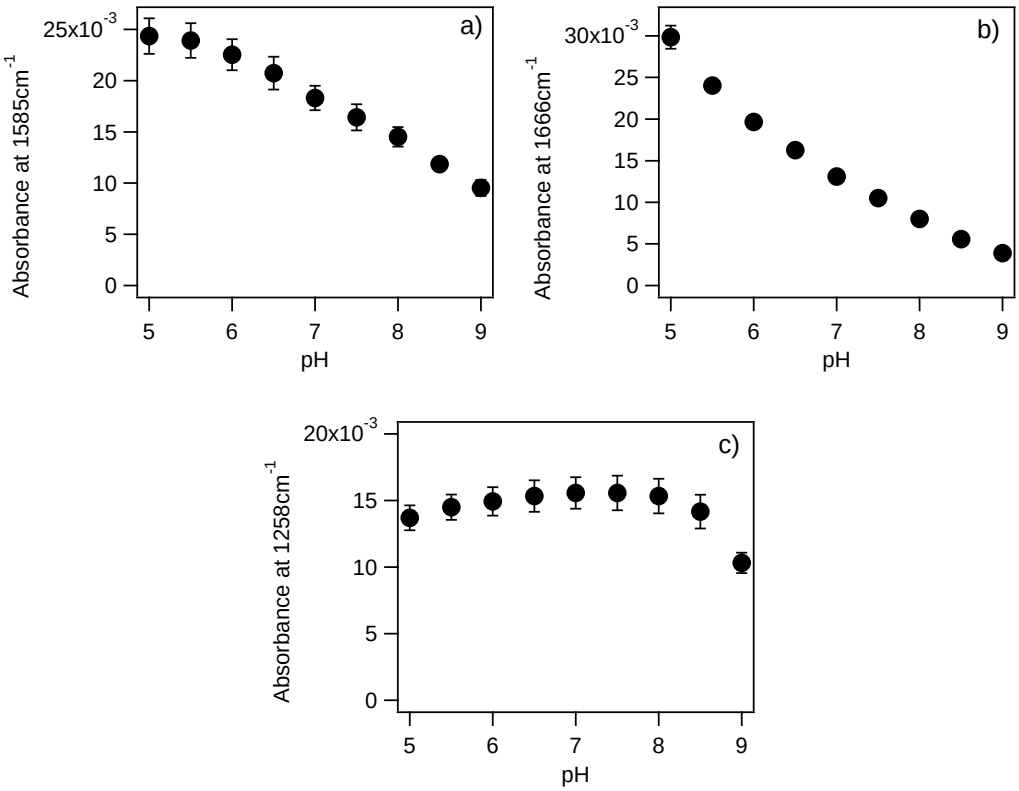

Figure 18. Adsorption of a) citrate b) oxalate and c) pyrocatechol adsorption on 6 mg hematite film as a function of pH, at I = 10 mM KCl, and a 2 mL/min flow rate at room temperature. Data points represent the average of three experiments. Error bars are ±s.

Trends observed in Figure 18 show an increase in oxalate and citrate adsorption with decreasing pH. This trend is likely caused by an increase in positive charge on the surface of hematite, which acts as a stronger electrostatic attractive force for the anionic model organics. The trend for pyrocatechol adsorption to hematite is not as straightforward, with adsorption increasing from pH 9 to 7 before decreasing slightly as pH is lowered to 5. Further analysis of pH envelope adsorption curves was performed in Situm et al. using triple-layer surface complexation

modelling.[45] The same pH envelope adsorption experiments were conducted using goethite nanoparticles, of which the absorption spectra is shown in Figure 19.

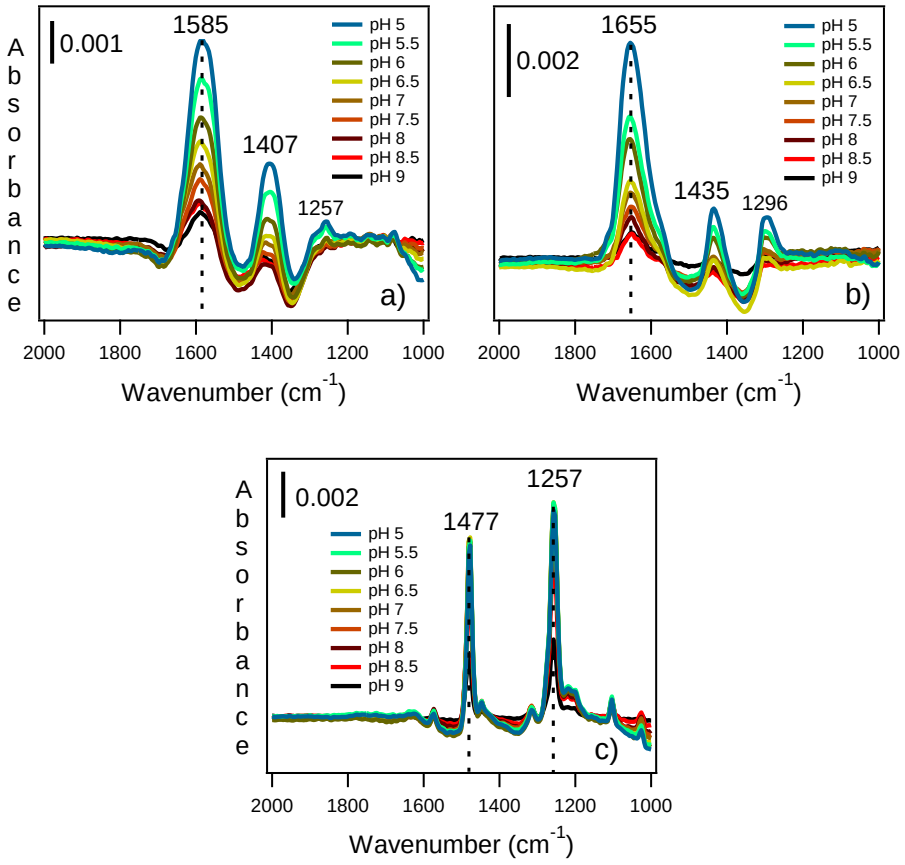

Figure 19. Adsorption of model organics (1 mM) on 16 mg goethite film at varying pH, I = 10 mM KCl, and a 2 mL/min flow rate at room temperature and nitrogen gas bubbling. ATR-FTIR absorbance spectra of adsorbed a) citrate, b) oxalate and c) pyrocatechol respectively.

pH envelope adsorption experiments were performed on goethite in order to compare the effect that pH has on the adsorption of model organics to different iron oxide nanoparticles. Unlike pH envelope adsorption on hematite nanoparticles, Figure 19 illustrates no observed shift in the

spectra for any of the model organics. Figure 20 shows adsorption to goethite nanoparticles of model organics as a function of pH, using baseline-corrected maximum peak heights.

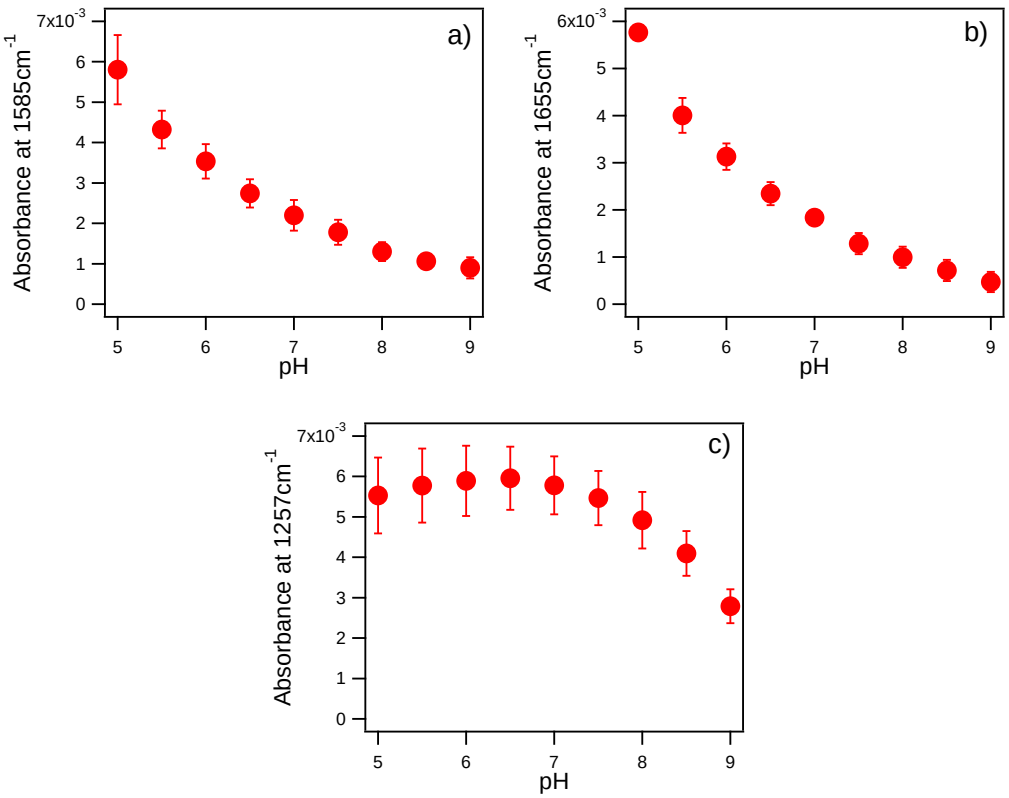

Figure 20. Adsorption of a) citrate b) oxalate and c) pyrocatechol adsorption on 16 mg goethite film as a function of pH, at I = 10 mM KCl, and a 2 mL/min flow rate at room temperature. Data points represent the average of three experiments. Error bars are ±s.

The trends observed in the pH envelope adsorption curves for goethite nanoparticles are similar to trends observed for hematite nanoparticles. Oxalate and citrate adsorption was observed to increase as an inverse function of pH, which is consistent with increased positive charge on the surface of goethite. Pyrocatechol, on the other hand, increases in adsorption from pH 9 down to around pH 6 before slightly decreasing as the pH is lowered to 5.

4.3 Adsorption kinetics of model organic matter

Adsorption kinetic experiments were conducted using citrate, oxalate, and pyrocatechol adsorption on unreacted hematite films at pH 7. Spectra from typical experiments are shown in Figure 21.

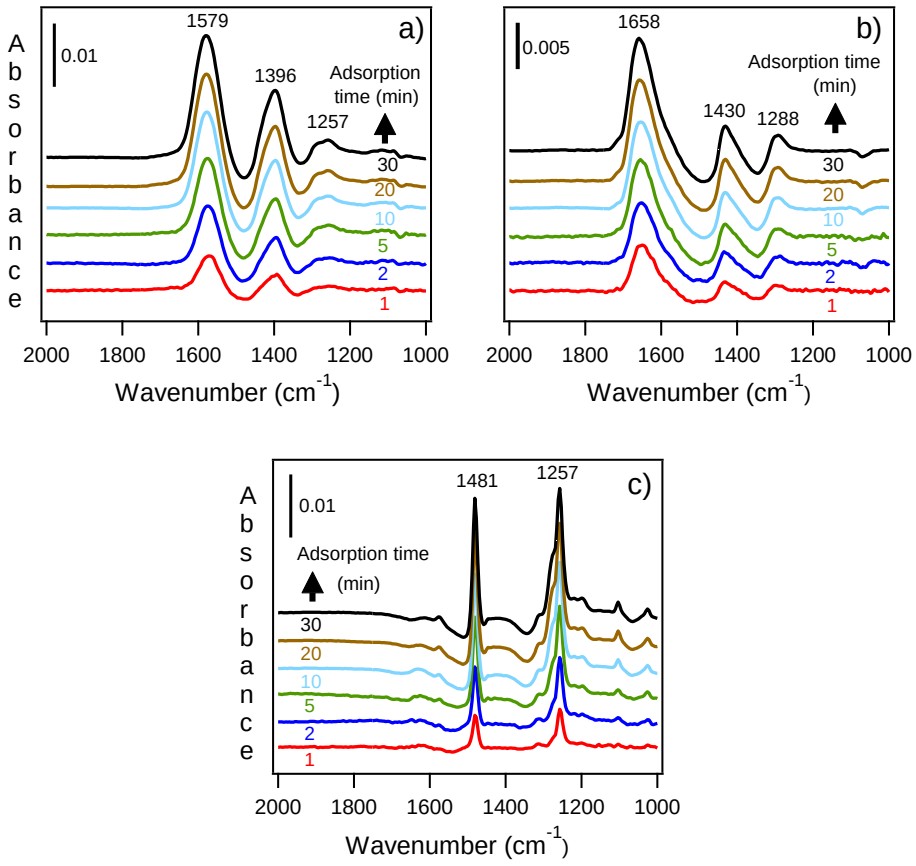

Figure 21. Adsorption of model organics (1 mM) on to a clean, 6 mg hematite film at pH 7, I = 10 mM KCl, and a 2 mL/min flow rate at room temperature. ATR-FTIR absorbance spectra of adsorbed a) citrate, b) oxalate and c) pyrocatechol respectively, collected as a function of time.

Using peak heights at 1579, 1658 and 1257 cm^{-1} for citrate oxalate and pyrocatechol respectively, baseline-corrected adsorption kinetic curves were generated as a function of

adsorption time. Baseline-corrected adsorption kinetic curves for each model organic on unreacted hematite nanoparticles are shown in Figure 22.

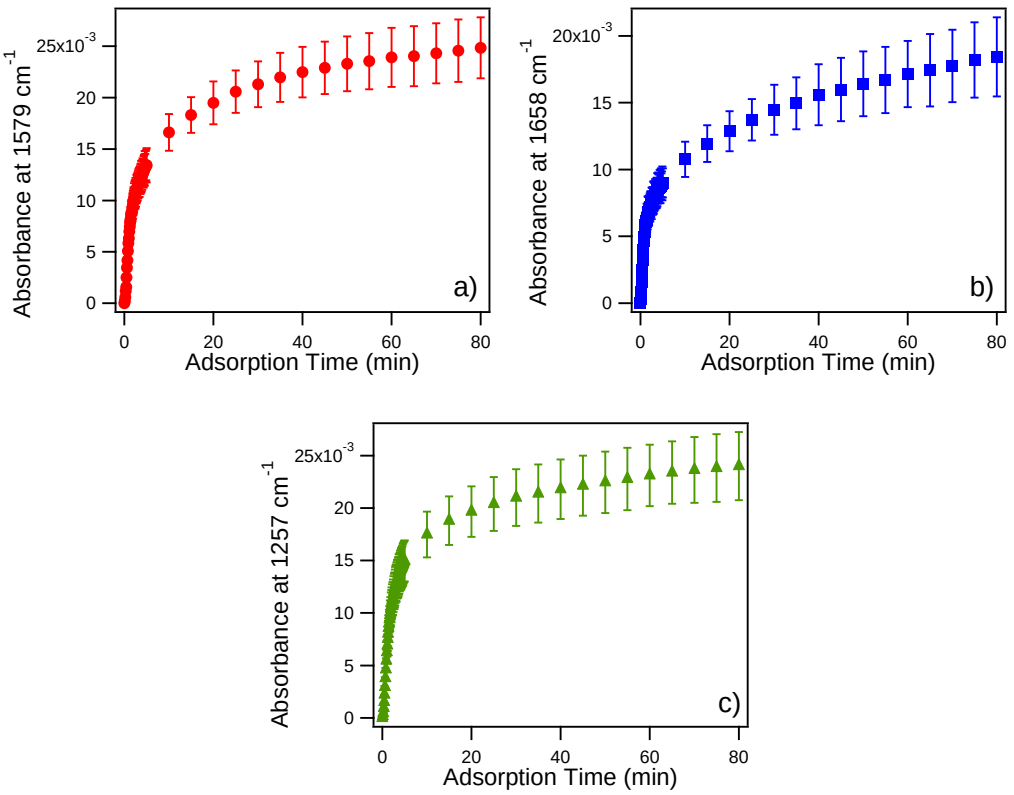

Figure 22. Adsorption kinetic curves generated from the baseline-corrected ATR-FTIR absorbances for a) citrate, b) oxalate and c) pyrocatechol adsorbed on to a clean, 6 mg hematite film at pH 7, I = 10 mM KCl, and a 2 mL/min flow rate at room temperature, respectively. Data points represent the average of three to four experiments. Error bars are ±s.

The results shown in Figure 22 show that organic adsorption on hematite is rabid fast, with equilibrium between aqueous phase model organics and the surface of hematite having been reached by the 80 min adsorption time. In order to gain more information on the type of surface complexes each model organic forms with the surface of hematite nanoparticles, adsorption kinetic experiments were carried out under multiple ionic strength conditions. The hypothesis is that charged surface complexes, especially outer-sphere complexes, will have rates of adsorption

different than inner- sphere because of the charge double layer formed on the surface of hematite by potassium and chloride ions. From Figure 22, it is observed that adsorption of model organics to the surface of hematite is fast within the first five minutes of adsorption time. Linearization of model organic adsorption kinetic curves can be performed in order to extract observed initial rates of adsorption. Baseline-corrected adsorption kinetic curves for each model organic on unreacted hematite nanoparticles under the various ionic strength conditions are shown in Figure 23.

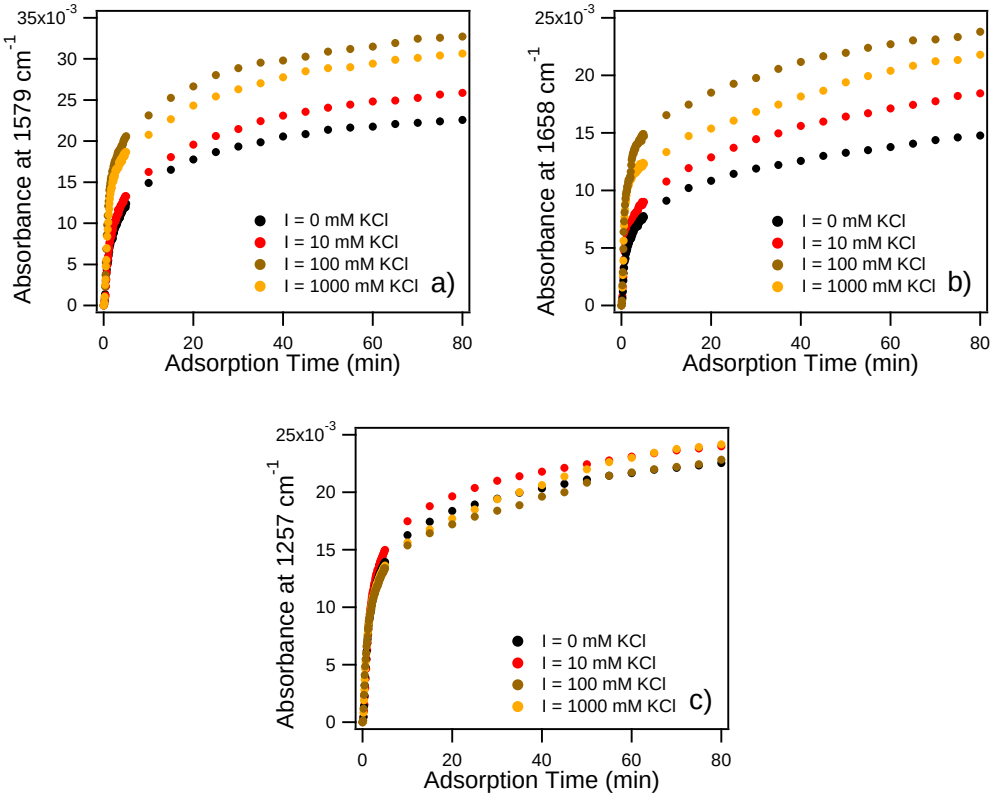

Figure 23. Adsorption kinetics of a) citrate, b) oxalate, and c) pyrocatechol on 6 mg hematite film with 0, 10, 100, and 1000 mM KCl at pH 7. [Data points represent the average of two to four experiments and error bars have been removed for clarity.]

Linearization of model organic adsorption kinetic curves shown in Figure 23 was preformed and the resulting linearized adsorption kinetic curves are shown in Figure 24.

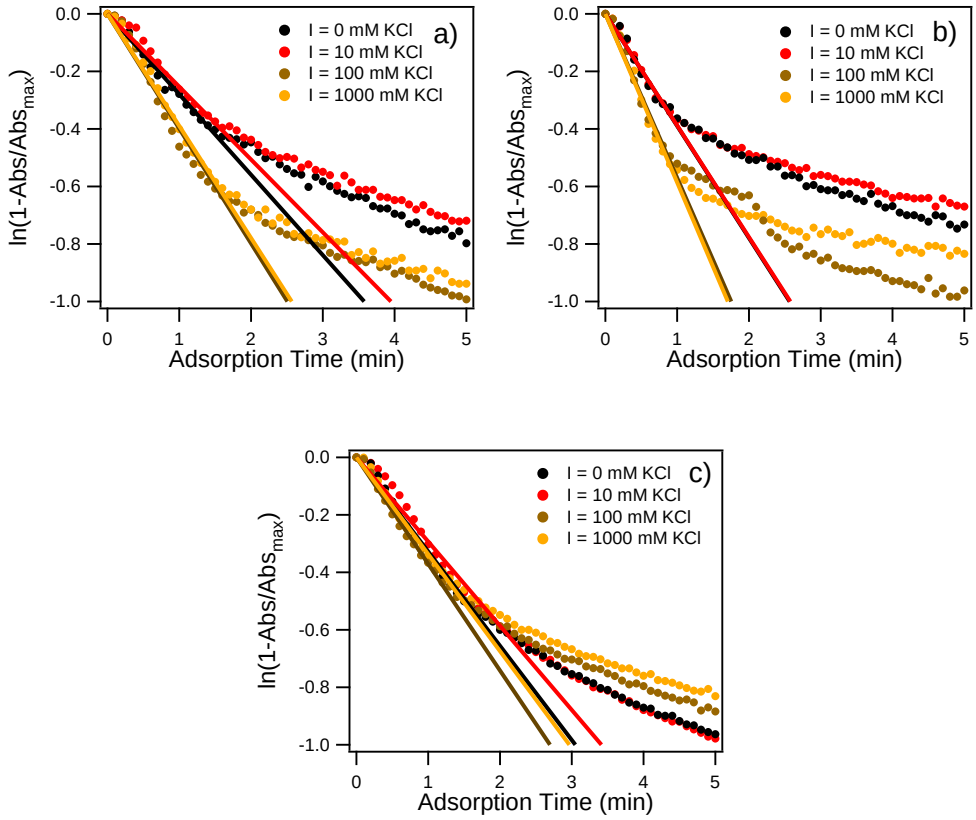

Figure 24. Linearized adsorption kinetics of a) citrate, b) oxalate, and c) pyrocatechol on 6 mg hematite film with 0, 10, 100, and 1000 mM KCl at pH 7. ln(1-(A(Organic)/A(OrganicMax))) with A(Organic) corresponding the band measured for citric oxalate, and pyrocatechol respectively. [Data points represent the average of two to four experiments and error bars have been removed for clarity.]

The linearization preformed in Figure 24 involves taking a natural log of model organic peak heights absorbances normalized against the maximum peak height absorbance measured at 80 minutes adsorption time (equation 4). The least-squared fits added to linearized model organic adsorption kinetics in Figure 24 are predicted to have slopes equal to the observed initial rates of adsorption (r_{obs1}) according to the kinetic form of the Langmuir adsorption model described in section 3.5. Initial observed rates of model organic adsorption to unreacted hematite nanoparticles are shown in Table 7.

Table 7. Linearized first-order observed adsorption rates (min^{-1}) at various ionic strength conditions of model organics on 6 mg hematite film.

Adsorption of surface organic:	Ionic strength condition			
	0 mM KCl	10 mM KCl	100 mM KCl	1000 mM KCl
Citrate	0.28 ± 0.01	0.25 ± 0.02	0.40 ± 0.05	0.39 ± 0.08
Oxalate	0.39 ± 0.06	0.39 ± 0.02	0.57 ± 0.11	0.59 ± 0.13
Pyrocatechol	0.33 ± 0.04	0.29 ± 0.01	0.37 ± 0.16	0.33 ± 0.15

The observed initial rates of model organic adsorption shown in Table 7 show a correlation between ionic strength and initial rates of absorbance for citrate and oxalate but a complete insensitivity of the initial rates of adsorption of pyrocatechol to changes in ionic strength. This increase in adsorption rates for the charged citrate and oxalate species is attributed to the presence of electrolytes and the surface of hematite. A charged double layer of electrolytes the surface of hematite should increase the adsorption of the negatively charged species because of electrostatic attraction to potassium ions. These results support proposed surface complexes of model organics on hematite nanoparticles. The adsorption rate of pyrocatechol on hematite nanoparticles supports the assignment of a neutral inner-sphere complex while the enhancing effect of ionic strength on citrate and oxalate adsorption help support the assignment of charged surface complexes.

4.4 Desorption kinetics of model organic matter on hematite

In this work, two different arsenicals were reacted with hematite nanoparticles, which had either been exposed to model organics or were unreacted, in order to gather information on the effect that organic functional groups have on the kinetics of arsenical adsorption. Information gathered from model organic desorption from hematite nanoparticles may also be utilized to support the assigned surface complexes of model organics on hematite. Previous studies conducted

within the Al-Abadleh group have shown that arsenate forms a strong inner-sphere bidentate binuclear complex with the surface of hematite nanoparticles, while DMA forms an outer-sphere complex.[3, 38] Desorption studies using these selected arsenicals, along with different concentrations of the weak desorbing agent chloride, allows for a general picture of the effectiveness that different types of desorbing agents have on adsorbed model organics.

4.4.1 Desorption kinetics of citrate due to flowing arsenicals

Experiments on the desorption of citrate from hematite nanoparticles were conducted using arsenate, DMA, and background KCl. Spectra from typical experiments are shown in Figure 25.

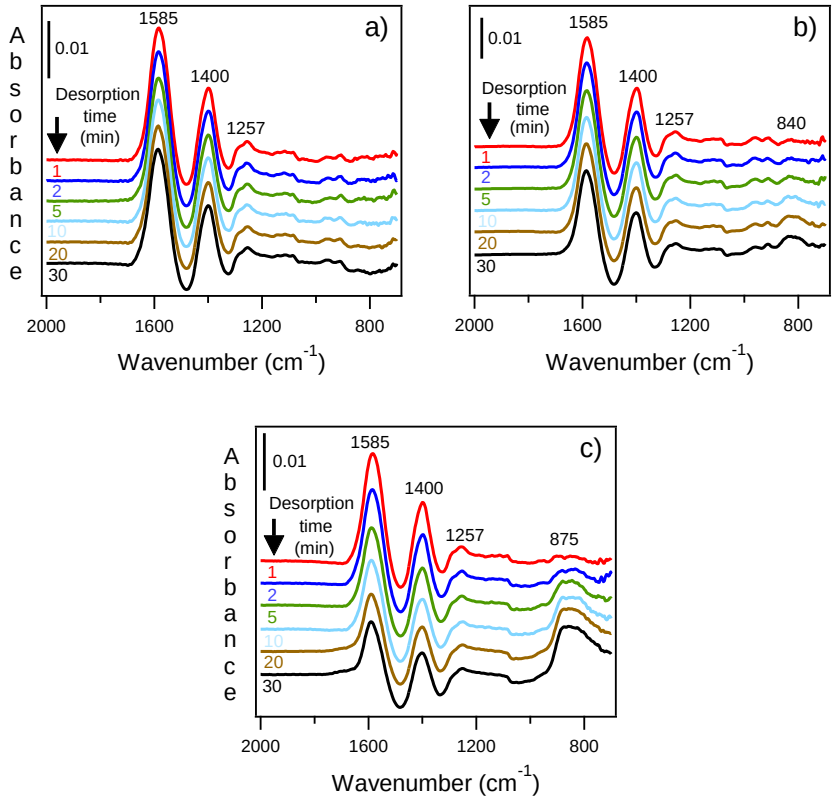

Figure 25. ATR-FTIR absorbance spectra correspond to citrate desorption from 6 mg hematite film at pH 7, I = 10 mM KCl, and a 2 mL/min flow rate at room temperature, by the flowing of a) 10 mM Cl^-, b) 1 mM DMA and c) 1 mM Ars respectively.

Using baseline-corrected peak height absorbances at 1585 cm^{-1} plotted as a function of desorption time, kinetic curves for citrate desorption from hematite nanoparticles were generated, and are shown in Figure 26 along with their linearized citrate desorption kinetics.

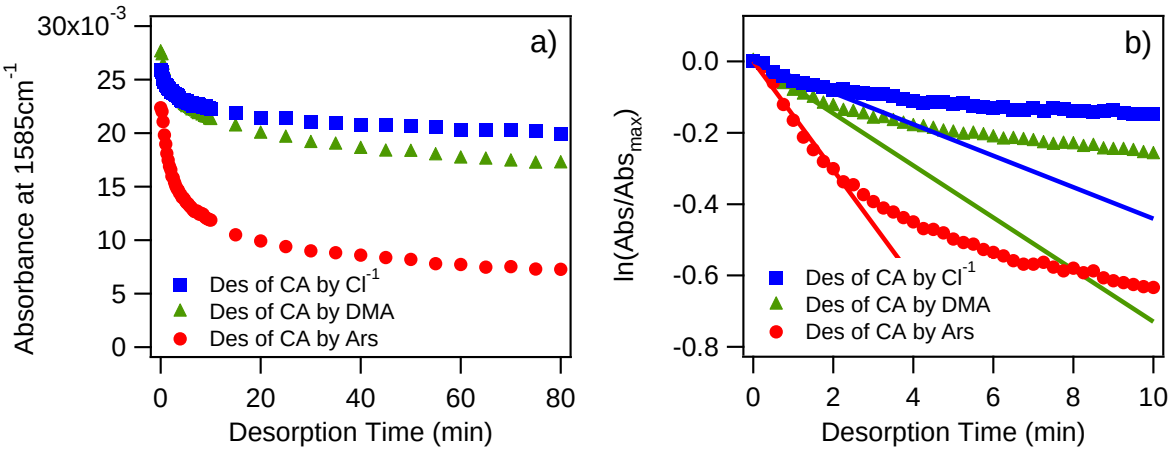

Figure 26. Desorption kinetic curves generated from the baseline-corrected ATR-FTIR absorbances of a) citrate from 6 mg hematite film at pH 7, I = 10 mM KCl, and a 2 mL/min flow rate at room temperature, by 10 mM KCl, 1.0 mM Arsenate and 1.0 mM DMA, and b) shows ln(A(Organic)/A(OrganicMax)) with A(Organic) corresponds to absorbance at 1579 cm^{-1}. Data points represent the average of two to four experiments and error bars have been removed for clarity.

Linearized desorption kinetics were generated in a similar way to linearized adsorption kinetics: by taking the natural log of baseline-corrected peak height absorbance values, normalized against the initial baseline-corrected peak height absorbance at 0 min desorption time (equation 9). The comparison of the slopes of the least-squared fits of linearized citrate desorption kinetics shows the effectiveness of different desorbing agents, as the slopes of the least-squared fits are predicted to be equal to the observed initial rates of desorption (k'_{des1}) according to the Langmuir desorption model described in section 3.6. Arsenate has the highest initial desorption rate of citrate

from the surface of hematite in the desorption kinetics curves in Figure 26, while the background 10 mM chloride solution has the lowest initial rate of citrate desorption.

4.4.2 Desorption kinetics of oxalate due to flowing arsenicals

Desorption kinetic experiments of citrate from hematite nanoparticles were conducted using arsenate, DMA, and background KCl at pH 7. Spectra from typical experiments are shown in Figure 27.

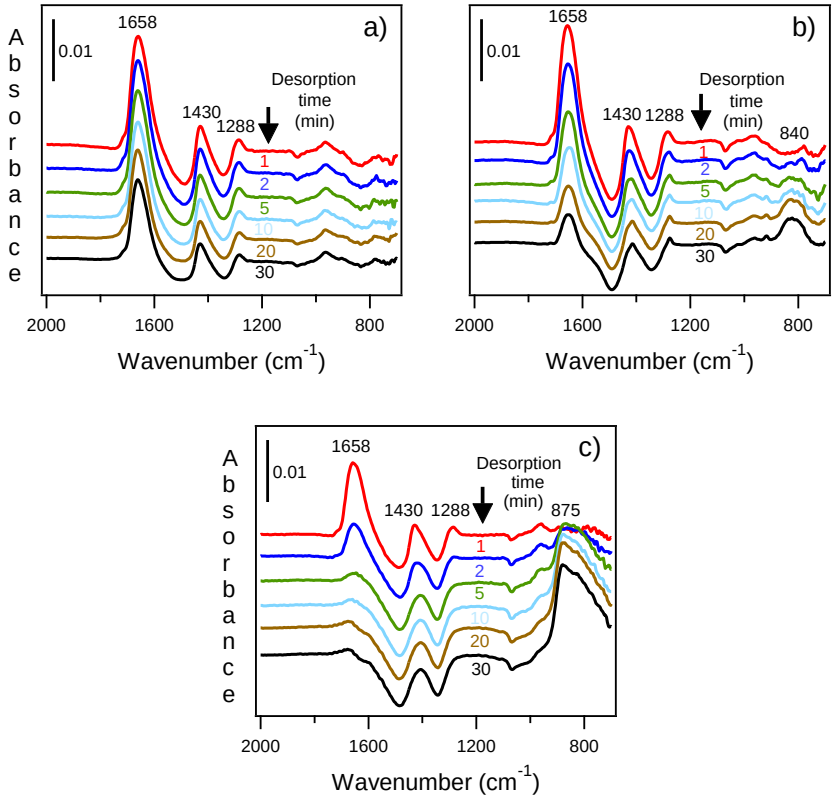

Figure 27. ATR-FTIR absorbance spectra correspond to oxalate desorption from 6 mg hematite film at pH 7, I = 10 mM KCl, and a 2 mL/min flow rate at room temperature, by the flowing of a) 10 mM Cl^-, b) 1 mM DMA and c) 1 mM Ars respectively.

Using baseline-corrected peak height absorbances at 1658 cm^{-1}, plotted as a function of desorption time, kinetic curves for oxalate desorption from hematite nanoparticles were generated, and are shown in Figure 28 along with their linearized citrate desorption kinetics.

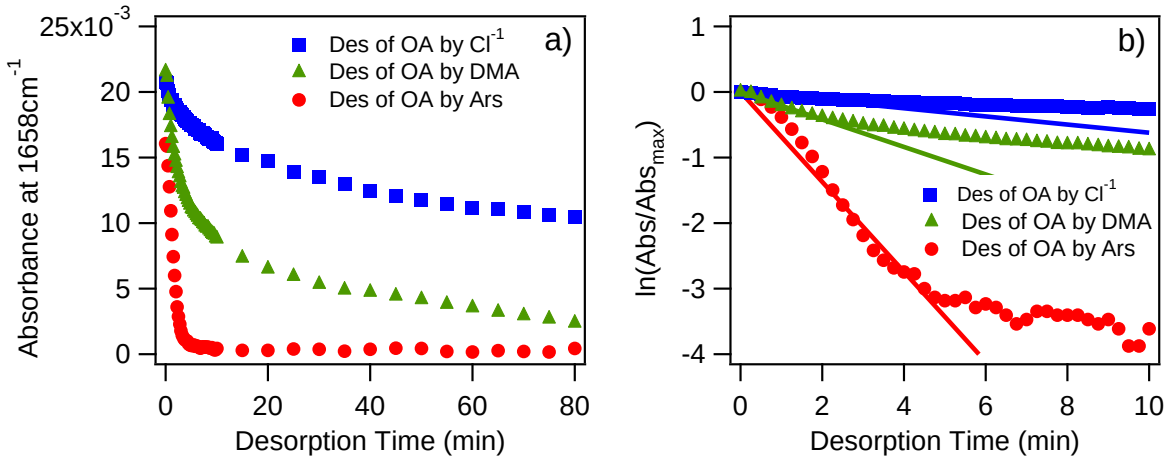

Figure 28. Desorption kinetic curves generated from the baseline-corrected ATR-FTIR absorbances of a) oxalate from 6 mg hematite nanoparticles at pH 7, I = 10 mM KCl, and a 2 mL/min flow rate at room temperature, by 10 mM Cl^-, 1.0 mM Arsenate and 1.0 mM DMA, and b) shows ln(A(Organic)/A(OrganicMax)) with A(Organic) corresponds to absorbance at 1658 cm^{-1}. Data points represent the average of two to four experiments and error bars have been removed for clarity.

Similar to the desorption kinetics of citrate shown in Figure 26, arsenate has the highest rate of initial desorption from hematite nanoparticles, while the background 10 mM chloride solution has the lowest initial rate of citrate desorption. However, unlike citrate desorption from hematite, oxalate desorption is much more rapid, with the surface oxalate peak at 1658 cm^{-1} being nonexistent after 10 minutes of desorption time using arsenate the desorbing agent, and almost completely absent after 80 minutes of desorption time using DMA. The high rates of desorption,

even by weak desorbing agents like DMA, support the assignment of surface-bound oxalate as being partially outer-sphere .

4.4.3 Desorption kinetics of pyrocatechol due to flowing arsenicals

Desorption kinetic experiments of pyrocatechol from hematite nanoparticles were conducted using arsenate, DMA, and background KCl at pH 7. Spectra from typical experiments are shown in Figure 29.

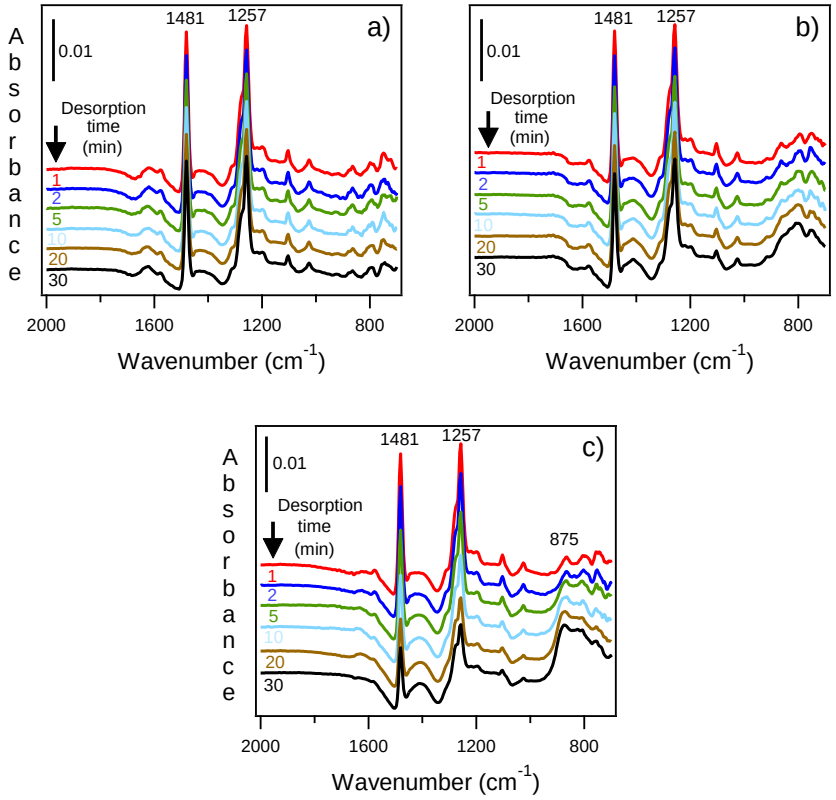

Figure 29. ATR-FTIR absorbance spectra correspond to pyrocatechol desorption from 6 mg hematite film at pH 7, I = 10 mM KCl, and a 2 mL/min flow rate at room temperature, by the flowing of a) 10 mM Cl^-, b) 1 mM DMA and c) 1 mM Ars respectively.

Using baseline-corrected peak height absorbances at 1257 cm^{-1} plotted as a function of desorption time, kinetic curves for pyrocatechol desorption from hematite nanoparticles were generated, and are shown in Figure 30 along with their linearized citrate desorption kinetics.

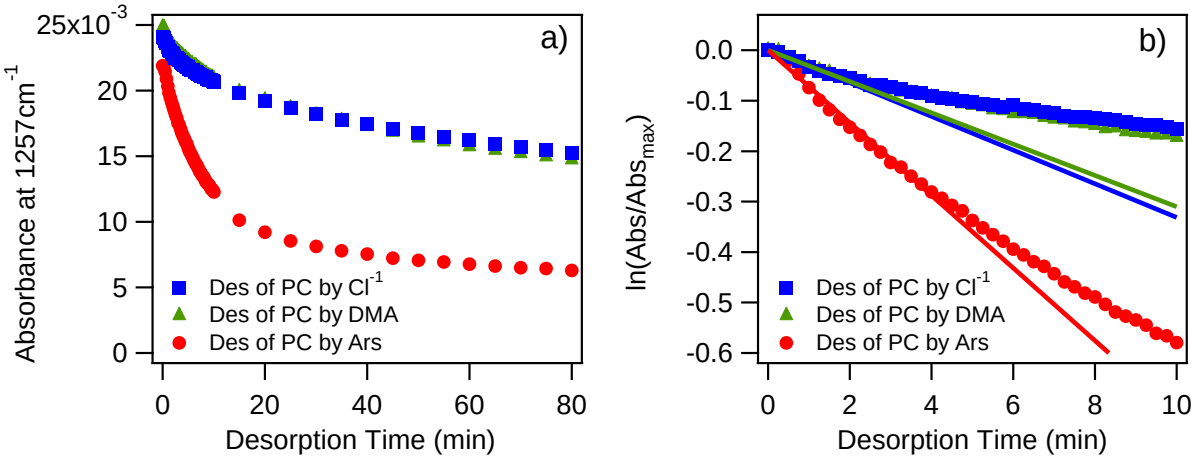

Figure 30. Desorption kinetic curves generated from the baseline-corrected ATR-FTIR absorbances of a) pyrocatechol from 6 mg hematite film at pH 7, I = 10 mM KCl, and a 2 mL/min flow rate at room temperature, by 10 mM Cl^-, 1.0 mM Arsenate and 1.0 mM DMA, and b) shows ln(A(Organic)/A(OrganicMax)) with A(Organic) corresponds to absorbance at 1257 cm^{-1}. Data points represent the average of two to four experiments and error bars have been removed for clarity.

Similar to the desorption kinetics shown in Figures 26 and 28, for citrate and oxalate desorption respectively, arsenate was observed for pyrocatechol to have the highest initial rate of desorption from hematite nanoparticles. However, the initial rate of pyrocatechol desorption by DMA is the same as the initial rate of desorption by the background 10 mM chloride solution. One possible explanation for this insensitivity of pyrocatechol to DMA as a desorbing agent is that the neutral inner-sphere complexes formed by pyrocatechol to the surface of hematite nanoparticles are not directly competing with the outer-sphere-forming DMA. Regardless, the insensitivity of pyrocatechol towards DMA supports the assignment of surface pyrocatechol to neutral inner-sphere.

4.4.4 Effect of aqueous chloride on the desorption kinetics of surface organics

In addition to the desorption experiments carried out using arsenate and DMA, desorption experiments were also performed as a function of chloride concentration from 0 – 1000 mM at pH 7 to get insight into the type of surface complexes the three model organics form with hematite. Using baseline-corrected peak height absorbances plotted as a function of desorption time, kinetic curves for citrate, oxalate and pyrocatechol desorption from hematite nanoparticles were generated and shown in Figure 31.

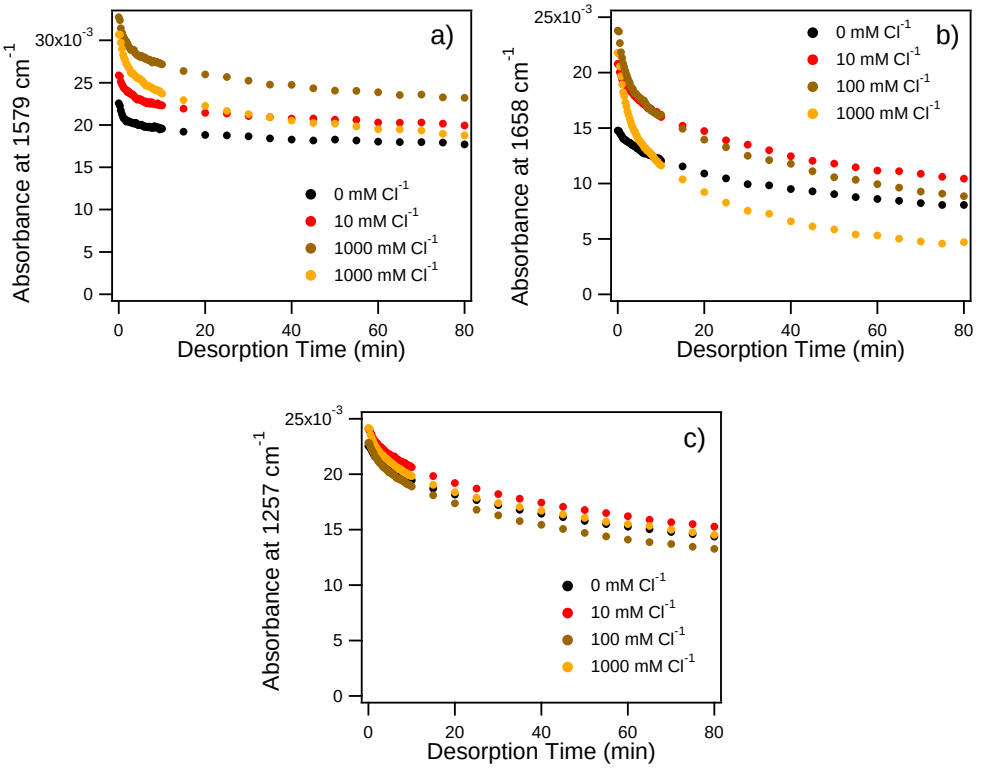

Figure 31. Desorption kinetics of a) citrate, c) oxalate, and e) pyrocatechol from 6 mg hematite film at pH 7, and a 2 mL/min flow rate at room temperature by 0, 10, 100, and 1000 mM Cl-. [Data points represent the average of two to four experiments and error bars have been removed for clarity.]

Linearization of model organic desorption kinetic curves shown in Figure 31 was preformed and the resulting linearized adsorption kinetic curves are shown in Figure 32.

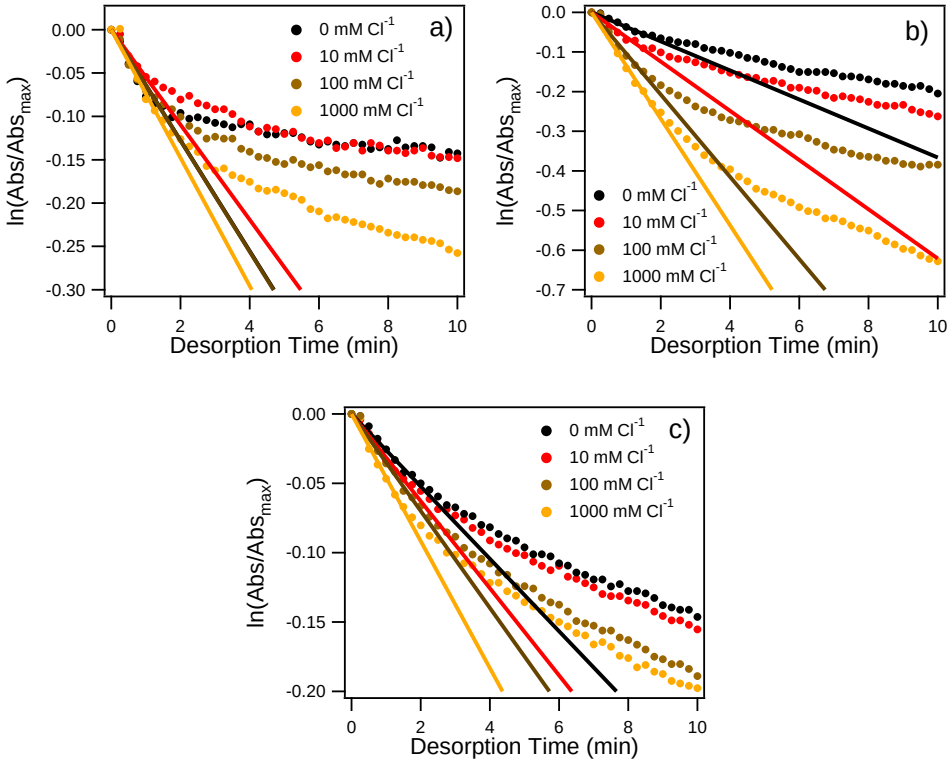

Figure 32. Desorption kinetics of a) citrate, c) oxalate, and e) pyrocatechol from 6 mg hematite film at pH 7, and a 2 mL/min flow rate at room temperature by 0, 10, 100, and 1000 mM Cl^-. b), d), and f) show ln(A(Organic)/A(OrganicMax)) with A(Organic) corresponding the band measured for citric oxalate, and pyrocatechol respectively. [Data points represent the average of two to four experiments and error bars have been removed for clarity.]

As an desorption kinetics of model organics by arsenicals, linearized desorption kinetics were generated by taking the natural log of baseline-corrected peak height absorbance values normalized against the initial baseline-corrected peak height absorbance at 0 min desorption time (equation 9). As predicted by the Langmuir desorption model, the slope of the lease squared fit of linearized desorption kinetics will be equal to the observed initial rates of desorption (k'_{des1}). Although discussed more in section 4.4.5, oxalate initial rates of desorption are very sensitive to

changes in chloride concentration consistent with the assignment of its surface complex as partially outer-sphere, while citrate and pyrocatechol show less sensitivity.

4.4.5 Comparison of surface organics desorption kinetics

The linearized kinetic curves shown in Figures 26, 28, 30, and 32 were analyzed to obtain observed first order rates of desorption of model organics from hematite as listed in Table 8.

Table 8. Linearized first-order observed desorption rates (min^{-1}) of model organics from 6 mg hematite film.

Desorption of surface organic:	Desorbing agent					
	0 mM KCl	10 mM KCl	100 mM KCl	1000 mM KCl	1.0mM Arsenate, 10 mM KCl	1.0mM DMA, 10 mM KCl
Citrate	0.064 ± 0.002	0.055 ± 0.004	0.064 ± 0.005	0.074 ± 0.009	0.156 ± 0.017	0.067 ± 0.010
Oxalate	0.036 ± 0.015	0.062 ± 0.001	0.104 ± 0.024	0.134 ± 0.016	0.685 ± 0.283	0.200 ± 0.013
Pyrocatechol	0.026 ± 0.001	0.033 ± 0.002	0.034 ± 0.018	0.072 ± 0.002	0.072 ± 0.021	0.031 ± 0.005

In desorption experiments using, negatively charged chloride, the ions act as desorbing agents as they compete for surface sites on hematite. It is observed that an increase in the chloride concentration is correlated with an increase in the initial observed rate of desorption. The exception to this is the observed desorption rate of citrate at 0 mM KCl, citrate, which had an increased initial observed rate of desorption compared to the observed rate at 10 mM KCl. One possible explanation

for this is that although there are more chlorine anions acting as desorbing agents in the 10 mM case than the 0 mM case, the presence of a small amount KCl has a stabilizing effect on the citrate–hematite complex. The stabilizing effect may be through ion pairing with the charged citrate–hematite complex. The response of citrate desorption to KCl is a further indicator that citrate forms a charged complex with hematite.

Desorption of model organics by arsenate and DMA have the same basic trend, with arsenate being a more effective desorbing agent then DMA for all three model organics. The flow of 1 mM arsenate at 10 mM KCl gives rise to the largest initial observed rates of desorption for all three model organics. Conversely, flowing 1 mM DMA at 10 mM KCl has a varied effect on model organic desorption rates from hematite. Oxalate desorption shows a high sensitivity to DMA flow, with an initial desorption rate 0.2 min^{-1} compared with a rate of only 0.062 min^{-1} for 10 mM KCl alone. Conversely, pyrocatechol shows no sensitivity towards the flowing of DMA with the observed intial rate of desorption being slightly lower than for 10 mM KCl alone (0.031 and 0.033 min^{-1} respectively). The sensitivity of citrate to DMA flow falls in-between with an observed initial desorption rate that is greater than the 10 mM KCl control experiment but lower than 1000 mM KCl case.

The comparison of initial observed rates of desorption shows that pyrocatechol surface complexes are the most resistant to desorption and oxalate surface complexes the least. This holds for all cases with the exception of the 0 mM KCl. The rates of desorption for the 0 mM KCl ionic strength experiments is pyrocatechol<oxalate<citrate, which is due to citrate being sensitive to the presence of KCl. One of the indicators that an outer sphere complex has been formed is changes in electrolyte concentration have an effect on the rate of desorption. The large increase in desorption rate of surface oxalate with increases in in chloride concentration helps support the

assignment of the oxalate–hematite complex as outer-sphere. Conversely, the lack of change and desorption rate of surface pyrocatechol to changes in chloride concentration helps support the assignment of a strong inner-sphere complex between pyrocatechol and the surface of hematite.

4.5 Adsorption kinetics of arsenic compounds on hematite

4.5.1 Adsorption on clean surfaces-spectra, spectral assignment and kinetic curves

Figure 33 shows the ATR absorption spectra of arsenate and DMA adsorption onto a clean hematite surface.

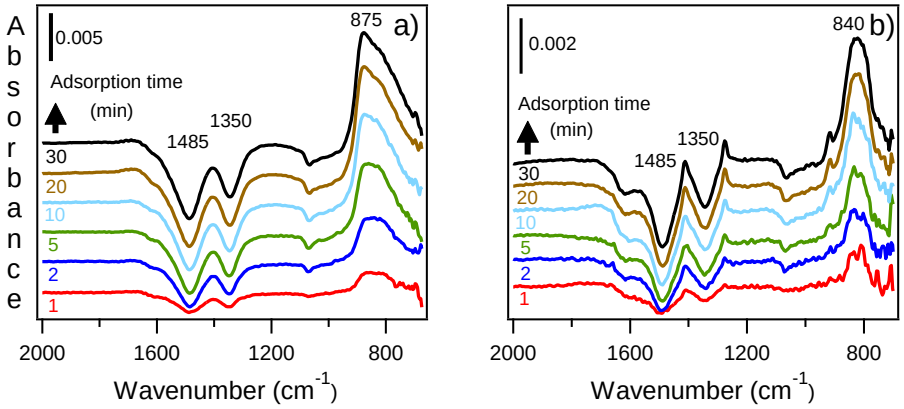

Figure 33. ATR-FTIR absorbance spectra of a) 1.0 mM arsenate and b) 1.0 mM DMA adsorption on to a clean, 6 mg hematite film at pH 7, I = 10 mM KCl, and a 2 mL/min flow rate at room temperature.

The main feature of adsorbed arsenate on clean hematite observed in Figure 33 a) is at 875 cm^{-1}. Arts et al. reported that this feature originates from arsenic-oxygen vibrations associated with an inner-sphere bidentate binuclear surface complex.[3] The main feature of adsorbed DMA on clean hematite observed in Figure 33 b) is at 840 cm^{-1}. Tofan-Lazar and Al-Abadleh report that this feature also originates from arsenic-oxygen vibrations and is associated with outer-sphere

complexation of DMA with the surface of hematite.[39] The negative features at 1485 and 1350 cm^{-1} are reported in Brechbuhl et al. to originate from a loss of carbonate from the surface of hematite.[51] The adsorption of aqueous species to the surface of hematite causes the loss of carbonate because carbonate competes with reactive sites on the surface of hematite. Negative carbonate features at 1485 and 1350 cm^{-1} are also observed in the ATR absorption spectra of surface adsorbed model organics but appear sharper in the arsenic surface spectra due to lack of surface model organic IR absorbance. The *v*(As-O) bands at 875 and 840 cm^{-1} were measured to create baseline-corrected kinetic curves seen in Figure 34 for arsenate and DMA respectively.

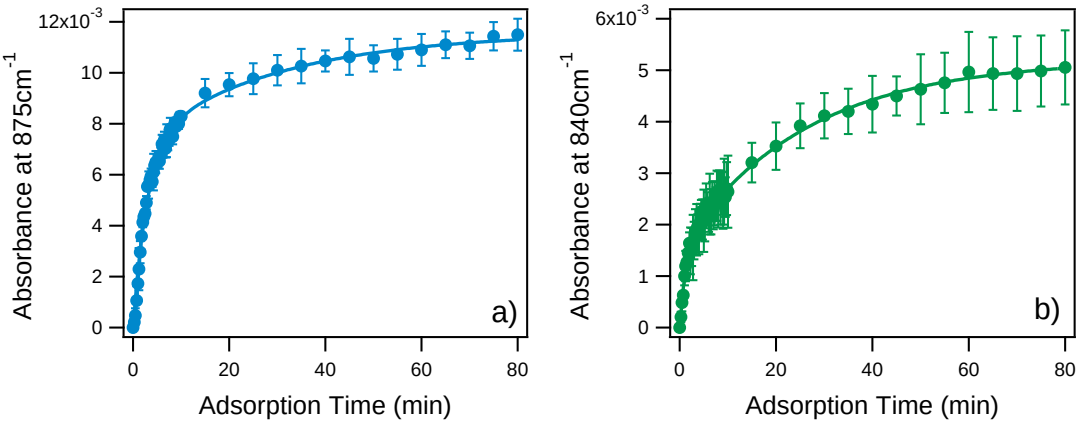

Figure 34. Baseline-corrected adsorption kinetics of a) 1.0 mM arsenate and b) 1.0 mM DMA on to a clean, 6 mg hematite film at pH 7, I = 10 mM KCl, and a 2 mL/min flow rate at room temperature, respectively. Data points represent the average of two to four experiments. Error bars are ±s.

The resulting kinetic curves show that after 80 min adsorption time, both arsenate and DMA have reached equilibrium with the surface of hematite. The use of these kinetic curves comes from their ability to be analyzed by kinetic model such as the kinetic form the Langmuir adsorption model to extract rates of adsorption.

4.5.2 Adsorption of arsenicals on surface pre-exposed to model organic matter-kinetic curves

Figure 35 shows the ATR absorption spectra of arsenate (a, c and e) and DMA (b, d and c) adsorption onto hematite surface pre-exposed to model organics.

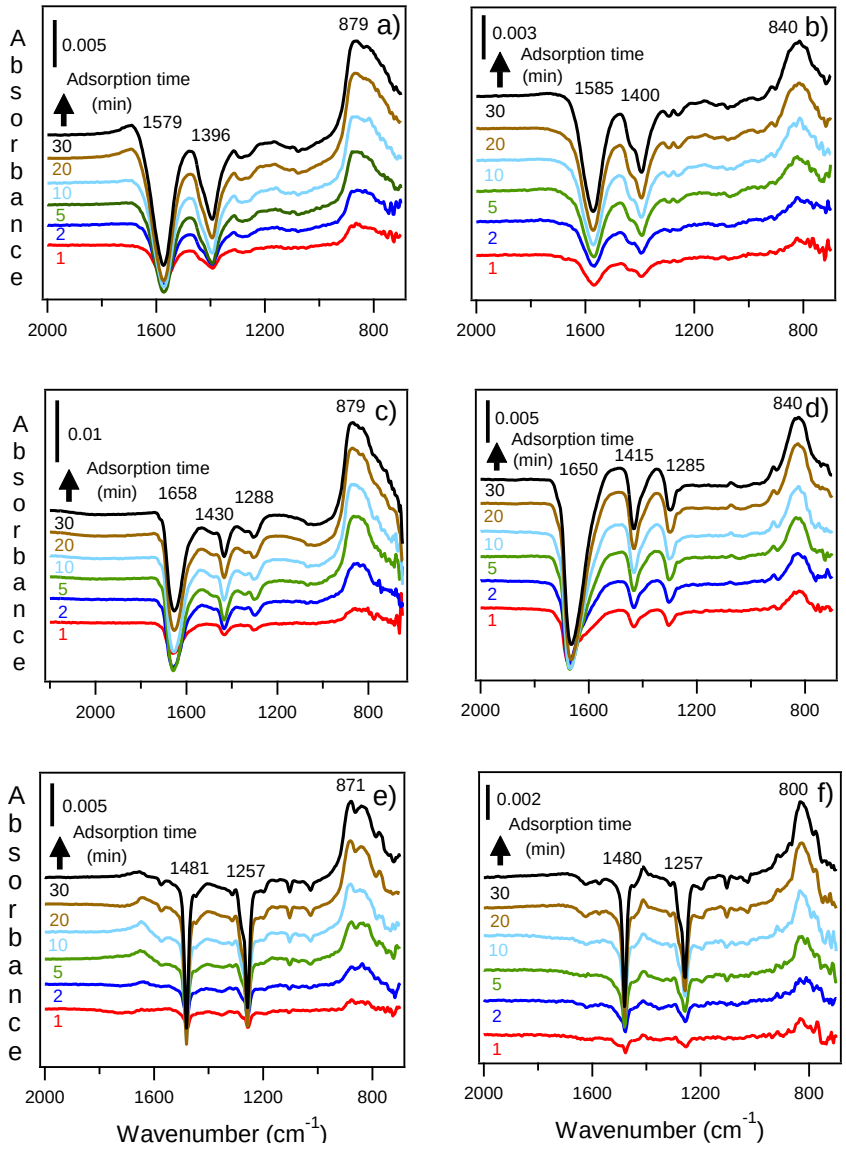

Figure 35. ATR-FTIR absorbance spectra of 1.0 mM arsenate adsorption on to a a) citrate, c) oxalate and e) pyrocatechol saturated 6 mg hematite film and 1.0 mM DMA adsorption on to a b) citrate, d) oxalate and f) pyrocatechol saturated 6 mg hematite film at pH 7, I = 10 mM KCl, and a 2 mL/min flow rate at room temperature. All absorbance spectra were generated using the corresponding 80 min model organic adsorption time single beam spectra as reference spectra.

Bands at around 875 cm^{-1} assigned to adsorbed arsenate and those bands at 840 cm^{-1} assigned to adsorbed DMA were measured to create baseline-corrected kinetic curves for arsenicals adsorption on the surface of hematite as a function of adsorption time. In order to determine initial rates of adsorption of arsenate and DMA on hematite, kinetic curves were linearized using equation 5 and plotted as a function of adsorption time. Both kinetic curves and linearized kinetic curves for arsenate are shown in Figure 36 a) and b), and Figure 36 c) and d) for DMA.

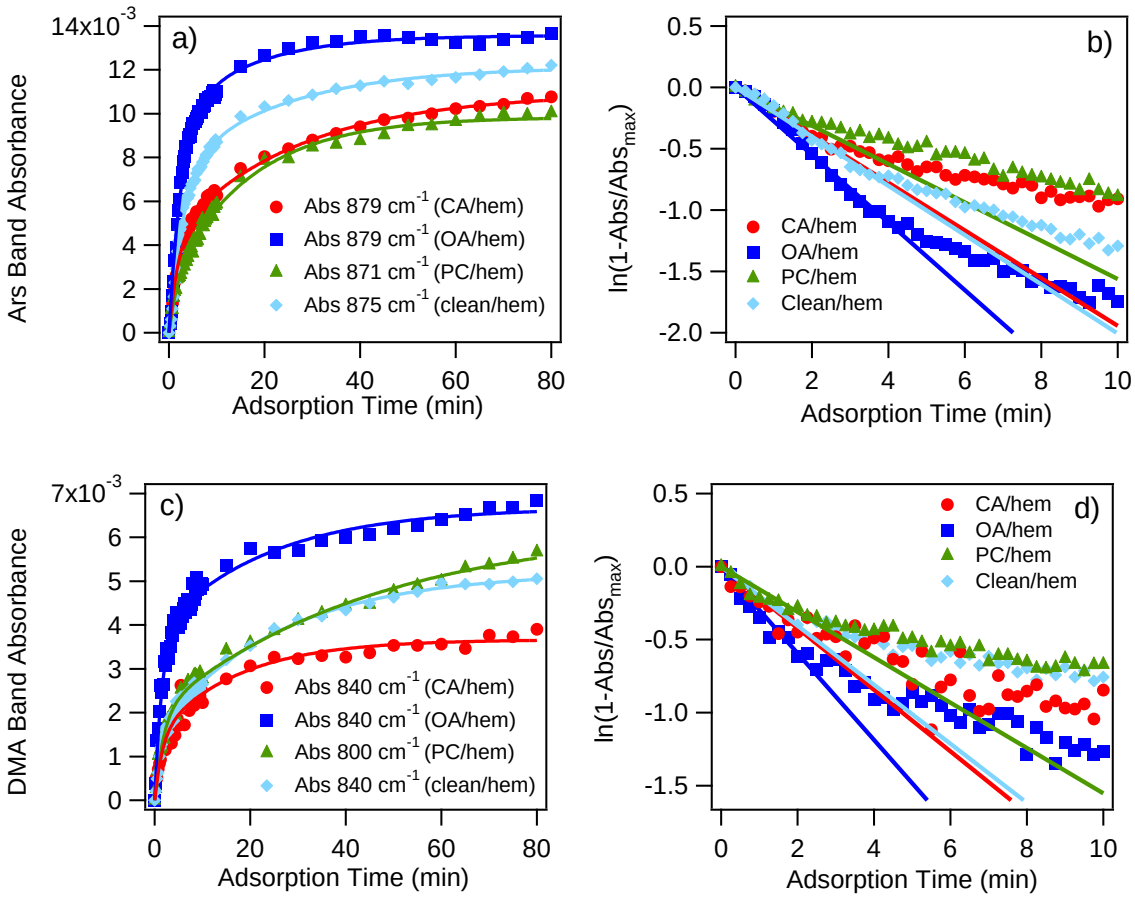

Figure 36. Baseline-corrected adsorption kinetics of a) arsenate and c) DMA respectively, on citrate, oxalate, pyrocatechol and unreacted hematite films at pH 7, I = 10 mM KCl, and a 2 mL/min flow rate at room temperature, and b) and d) show ln(1-(A(As)/A(AsMax))) with A(As) corresponding to each hematite film's arsenate or DMA peak respectively. Data points represent the average of two to four experiments and error bars have been removed for clarity.

Table 9 contains first-order observed rate constants of arsenate and DMA adsorption onto hematite clean and pre-exposed to model organics.

Table 9. Linearized first-order observed rate constants of 1.0 mM arsenate and 1.0 mM DMA adsorption onto 6 mg hematite in the presence and absence of adsorbed model organics.

Surface	Observed Rate (min^{-1}) 1.0 mM arsenate adsorption	Observed Rate (min^{-1}) 1.0 mM DMA adsorption
Unreacted hematite	0.21 ± 0.01	0.20 ± 0.01
Hematite/Citrate	0.19 ± 0.02	0.20 ± 0.03
Hematite/Oxalate	0.27 ± 0.02	0.30 ± 0.05
Hematite/Pyrocatechol	0.12 ± 0.03	0.16 ± 0.04

A few observations can be made from the kinetic curves in Figure 36 and first order observed rates of adsorption listed in Table 9 for each combination of arsenical and hematite surface. Citrate is not observed to have a significant effect on the initial rate of arsenate or DMA adsorption to hematite. A possible explanation for this is that the inner-sphere monodentate complex formed by citrate on the surface of hematite is blocking off the reactive surface sites that this inhibiting effect is counteracted by the increased electrostatic attraction provided by electrolytes within the diffuse double layer around the charged surface citrate. Citrate on the surface of hematite may allow for a larger diffuse double layer of electrolytes to form compared with unreacted hematite. Conversely, oxalate is observed to have an enhancing effect on the rate of adsorption of arsenate and DMA to the surface of hematite. One possible explanation for this is that surface bound oxalate also allows for a larger diffuse double layer of electrolytes to form because it is a much better leaving group then citrate it does not block reactive sites on the surface of hematite as effectively, thus leading to an increase in adsorption rates of arsenate and DMA. The results obtained from arsenate and DMA kinetic curves show that surface pyrocatechol has an

inhibitory effect on the initial rate of adsorption of arsenate but no significant effect on the rate of DMA adsorption. One explanation for this is that the surface pyrocatechol is blocks binding sites on hematite, which lowers the adsorption rate of arsenate and DMA, but the nonpolar interactions between phenolic groups on pyrocatechol and methyl groups on DMA lead to an increase in the adsorption rate of DMA. This would explain why pyrocatechol lowers the initial rate of adsorption of arsenate but is not observed to have an effect on DMA. To try to better understand these observations, arsenate adsorption experiments were repeated in triplicate over range of concentrations in order to extract pseudo- first order rate adsorption constants using equation 6, for arsenate on hematite nanoparticles. These experiments were conducted on clean hematite, oxalate and pyrocatechol hematite surfaces, the latter two having produced the highest and lowest observed first order rates of adsorption respectively. Figure 37 shows the observed first order rate constants and the maximum arsenate adsorption on oxalate, pyrocatechol and unreacted hematite surfaces.

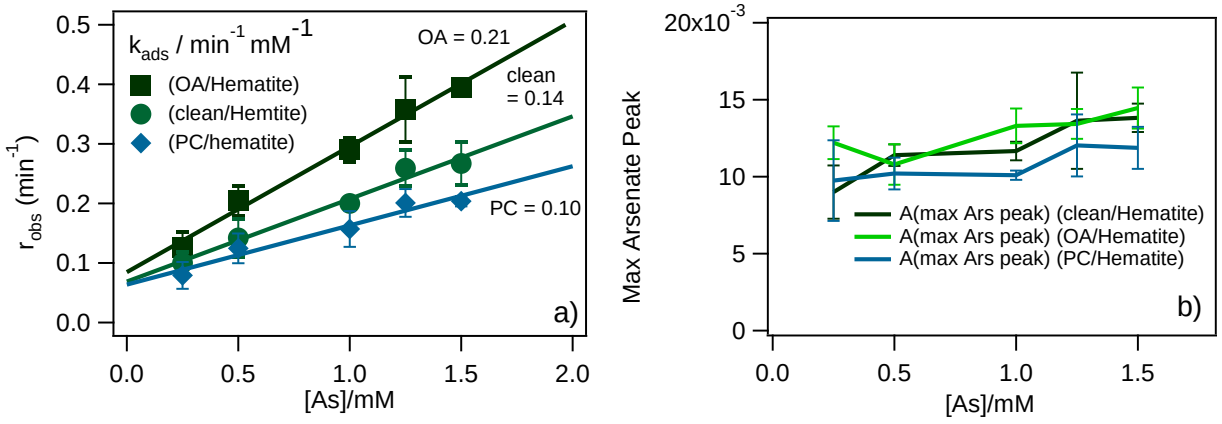

Figure 37. Dependency of a) the observed initial rate of adsorption (r_{obs}) on [arsenate(aq)] on hematite surfaces in the presence and absence of surface organics. Lines through the data represent linear least-squares fits and b) shows maximum adsorption of arsenate on hematite surfaces in the presence and absence of surface organics as a function of [arsenate(aq)]. Error bars are ±s.

Figure 37 a) confirms the trend observed in Figure 36 b) that surface oxalate increases, while surface pyrocatechol decreases the initial rate of arsenate adsorption. Table 10 lists the pseudo- first order rate constants for arsenate adsorption on hematite surfaces in the presence and absence of surface model organics. From Figure 37 b), the presence of pyrocatechol on the surface of hematite is not observed to have a significant inhibiting effect on the maximum adsorption of arsenate nor surface oxalate to have an increased the maximum adsorption. A possible explanation for this is that although both pyrocatechol and oxalate can alter the initial rates of arsenate adsorption to hematite, under longer reaction times they are simply desorbed from the surface of hematite and arsenate is able to reach equilibrium with the surface.

Table 10. Best-fit parameters from the linear least-squares regression to the experimental data of the observed adsorption rate (r_{obs}) versus [arsenate(aq)] as shown in Figure 37. For the adsorption of arsenate on hematite in the presence and absence of surface organics. 1 mM solution of each organic was flown over hematite for 80 min at 10 mM KCl and pH 7 prior to arsenate flow.

Surface organic (1.0 mM)	Arsenate peak (cm^{-1})	First order rate constant (min^{-1} mM^{-1} arsenate)
Unreacted hematite	875	0.14 ± 0.03
Oxalate/hematite	879	0.21 ± 0.03
Pyrocatechol/hematite	871	0.10 ± 0.02

Based on the differences in the pseudo- first order rate constants of arsenate adsorption on hematite surfaces in the presence and absence of surface organics in Table 10, the differences in the pseudo- first order rates of adsorption were found to be significant. The same set of experiments were carried out over range of DMA concentrations on hematite (either reacted or unreacted with model organics) in order to extract the pseudo- first order rates of DMA adsorption to hematite

nanoparticles using equation 6. Figure 38 shows the observed first order rate constants, as well as the maximum DMA adsorption, on oxalate, pyrocatechol and unreacted hematite surfaces.

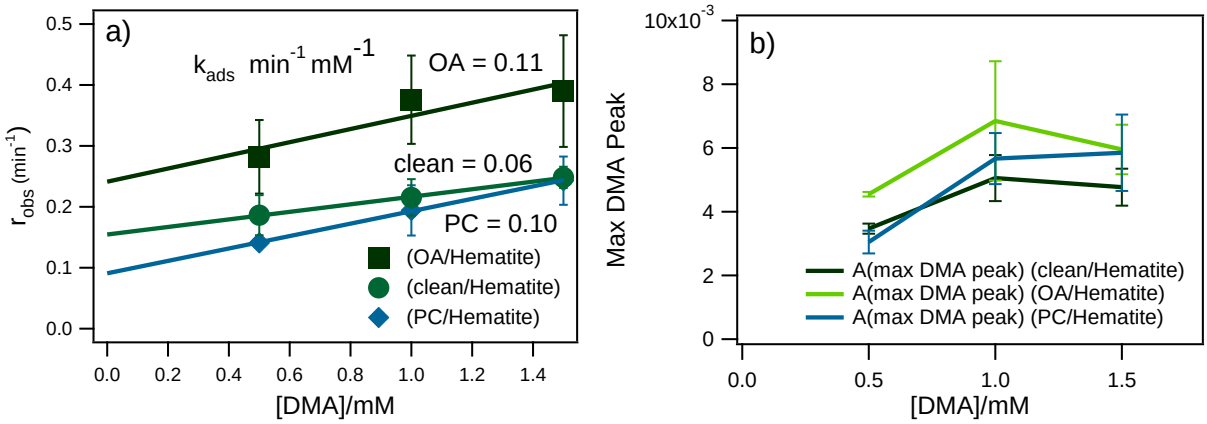

Figure 38. a) Dependency of a) the observed initial rate of adsorption (robs) on [DMA(aq)] on hematite surfaces in the presence and absence of surface organics. Lines through the data represent linear least-squares fits and b) shows maximum adsorption of DMA on hematite surfaces in the presence and absence of surface organics as a function of [DMA(aq)]. Error bars are ±s.

The same general trend for DMA max adsorption is observed in Figure 38 b) as was found in Figure 37 b), with no significant difference in max DMA adsorption on different hematite services. The pseudo- first order rate binding constants shown in Figure 38 a) are listed in Table 11.

Table 11. Best-fit parameters from the linear least-squares regression to the experimental data of the observed adsorption rate (r_{obs}) versus [DMA(aq)] as shown in Figure 38. For the adsorption of DMA on hematite in the presence and absence of surface organics. 1 mM solution of each organic was flown over hematite for 80 min at 10 mM KCl and pH 7 prior to DMA flow.

Surface organic (1.0 mM)	DMA peak (cm^{-1})	First order rate constant (min^{-1} mM^{-1} DMA)
Unreacted hematite	840	0.06 ± 0.02
Oxalate/hematite	840	0.11 ± 0.06
Pyrocatechol/hematite	800	0.10 ± 0.04

The results obtained for concentration-dependent DMA adsorption onto hematite films either reacted or unreacted with model organics is less definitive than the results obtained from arsenate experiments. While oxalate was observed to have an enhancing effect on the observed initial rates of DMA adsorption, the slope of these initial rates plotted against the concentration of DMA, k_{ads1}, is essentially the same as the associated k_{ads1} for DMA on pyrocatechol hematite nanoparticles. One large difference between these results are the y-intercepts, which are equal to k_{des1} according to equation 6, with the oxalate-reacted hematite surface having a much larger k_{des1} than that of DMA on pyrocatechol or on unreacted hematite.

5 Conclusions and significance

In conclusion, based on the results presented herein, the effect of small molecular weight organic on the binding of arsenicals to hematite is not purely inhibitory. Unlike studies involving large molecular weight natural organic matter, small molecular weight organic can either have an inhibiting or stimulating effect on the binding of arsenicals to hematite. This conclusion is based on the pseudo- first order rate constants of arsenate and DMA adsorption to hematite nanoparticles in the presence and absence of model organics. While surface pyrocatechol presence decreases arsenate binding kinetics, oxalate was observed to have increased rates of arsenate and DMA adsorption. This observed difference in effect is attributed to the ability of these organics to block binding sites on the surface of hematite and affect the presence of charged electrolytes in the diffuse double layer. The lack of change in adsorption kinetics of DMA on pyrocatechol hematite is hypothesized to be caused by nonpolar interaction between methyl and phenolic groups offsetting inhibitory effects of surface pyrocatechol. Both citrate and pyrocatechol were shown to form inner-sphere complexes on the surface of hematite with citrate forming a negatively charged monodentate and pyrocatechol both a mono and bidentate complexes. Oxalate in this work is

observed to form week outer-sphere complexes based on its sensitivity to changes in chloride concentration during the desorption experiments. This observation explains the enhancing effect of oxalate on rates of arsenate and DMA binding.

This work is significant because it provides a better fundamental understanding of the effect that different functional groups have on the binding of organics to geosorbents. This may aid in environmental modeling of organics through application of equilibrium constants. Also, the results provide a better understanding of the factors affecting the binding of arsenic compounds to geosorbents in the presence of organics, which helps to better model residence time of arsenicals in the aqueous phase and thus possibly predict their bioavailability and presence in drinking water. Application of these results may also aid in incorporating the effect of organics and fate/transport modelling of arsenicals. Finally, small molecular weight organics may serve specific functions within the environment (such as siderophores), or act as pollutants (such as artificial sweeteners) and hence their surface chemistry gives a better understanding of their environmental mobility.

Appendix A: Macros used in data collection

The number of scans is changed from 100 (used for manual spectra collection) to 5 or 25 depending on if an organic or an arsenical is being flown.

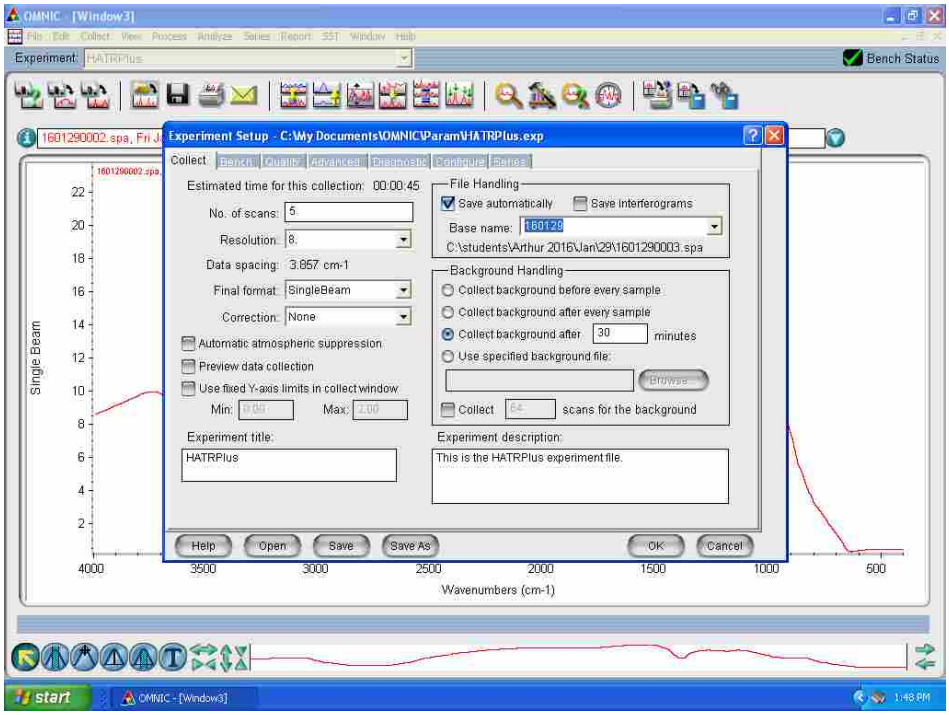

Macros Basic is opened and the spectrum collection macro is opened and the “Start of Loop” value adjusted to 50 or 40 depending on the spectra to be collected (50 for organics and 40 for arsenicals).

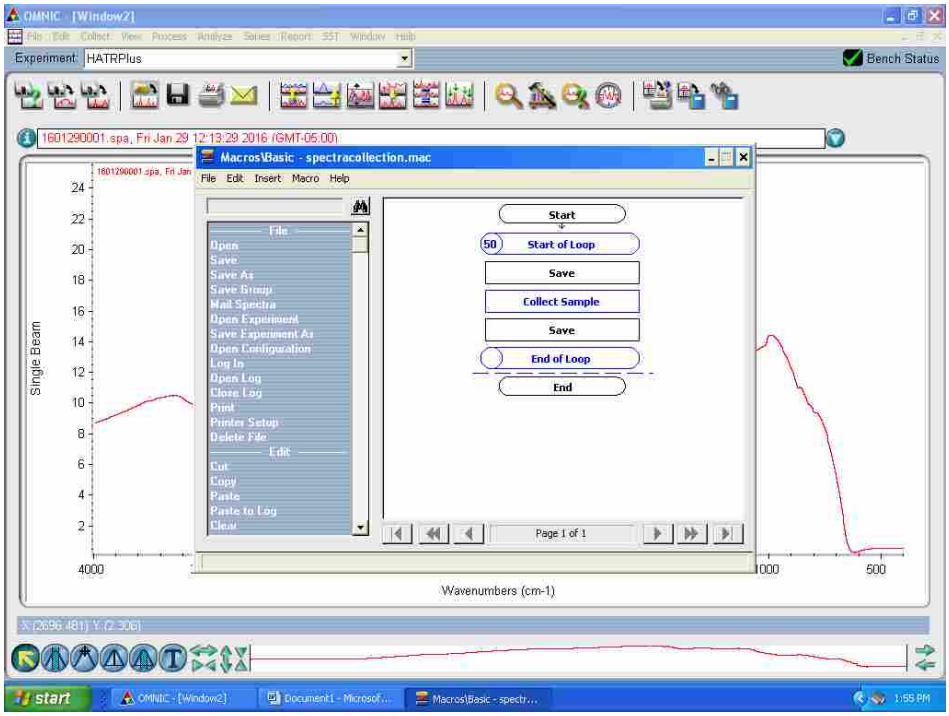

The macros is then run at the precise point when the solution reaches the ATR flow cell (the pump is started and one hand is on “Enter” while the other is on the stopwatch).

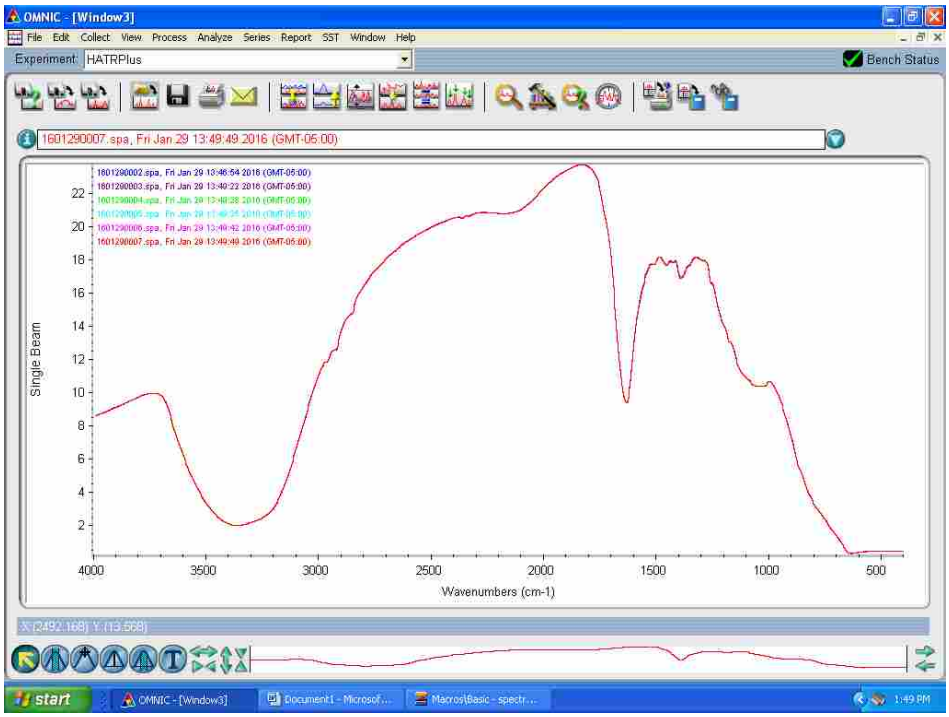

After the collection is finished the macros window is reappear on the screen.

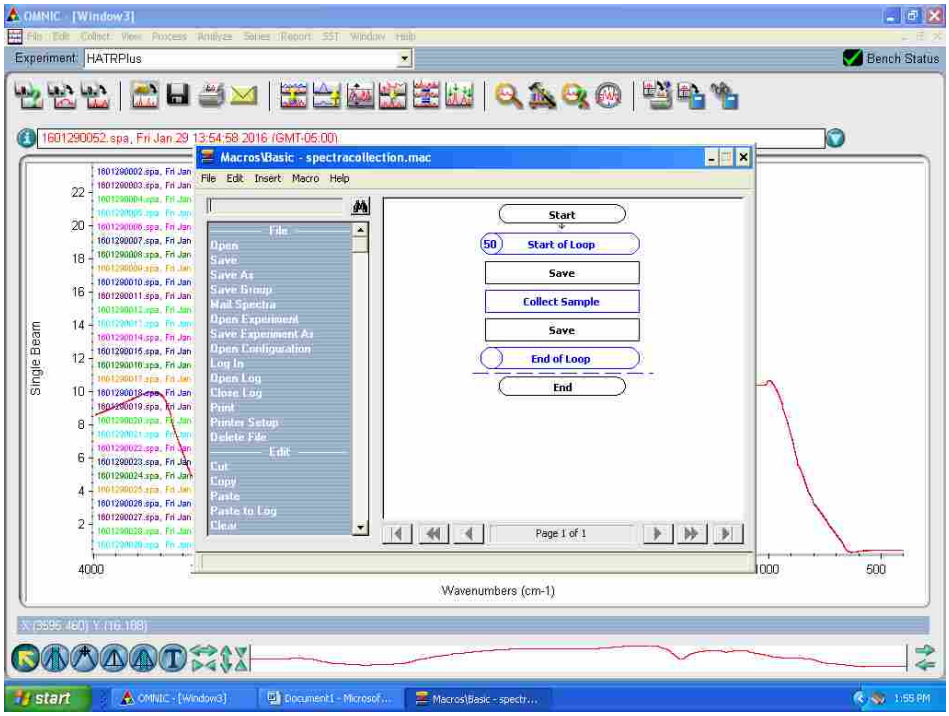

The number of scans is changed back in preparation for collection of manual scans.

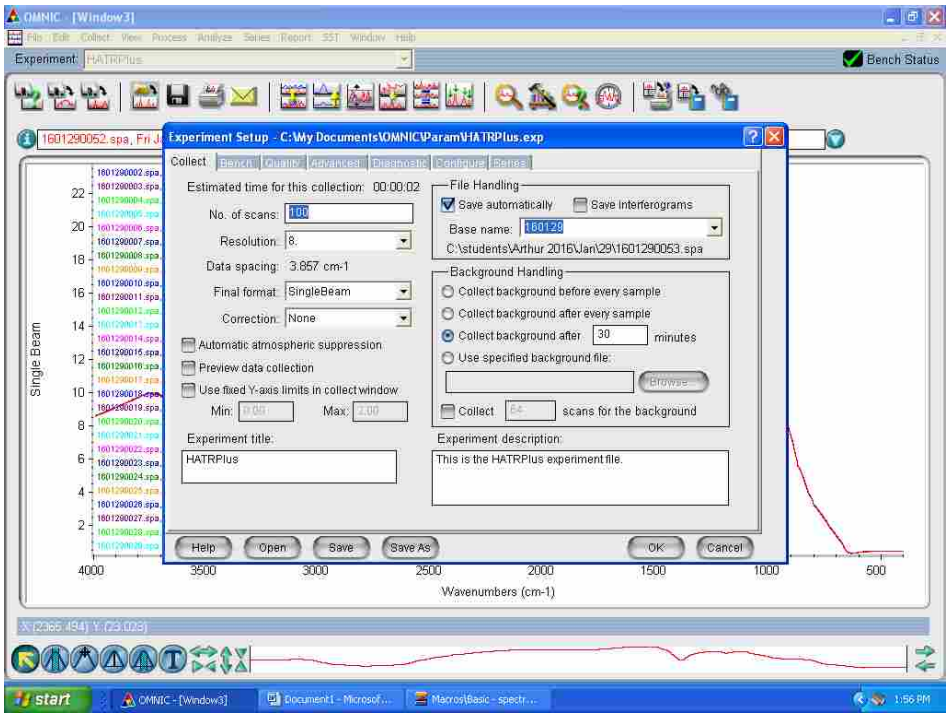

Appendix B: Macros used in data analysis

Macros is the useful program that we use to analyze Omnic spectra when there are too many in one experiment to analyze manually.

In Omnic, drag the black bar at the bottom of the screen to zoom in on the base line that will be used (should be about 50cm^-1 away from the base line).

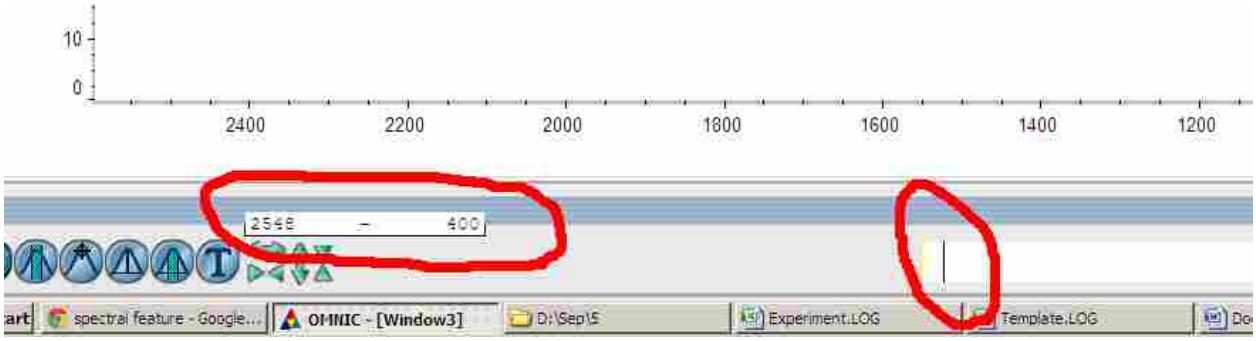

Press the **full scale** near the top of the screen

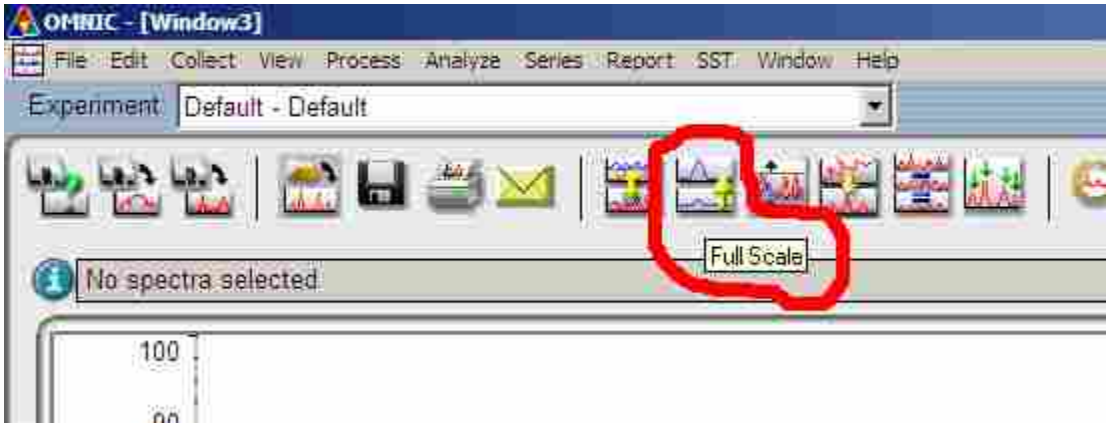

Open Macros and open the data analysis macro.

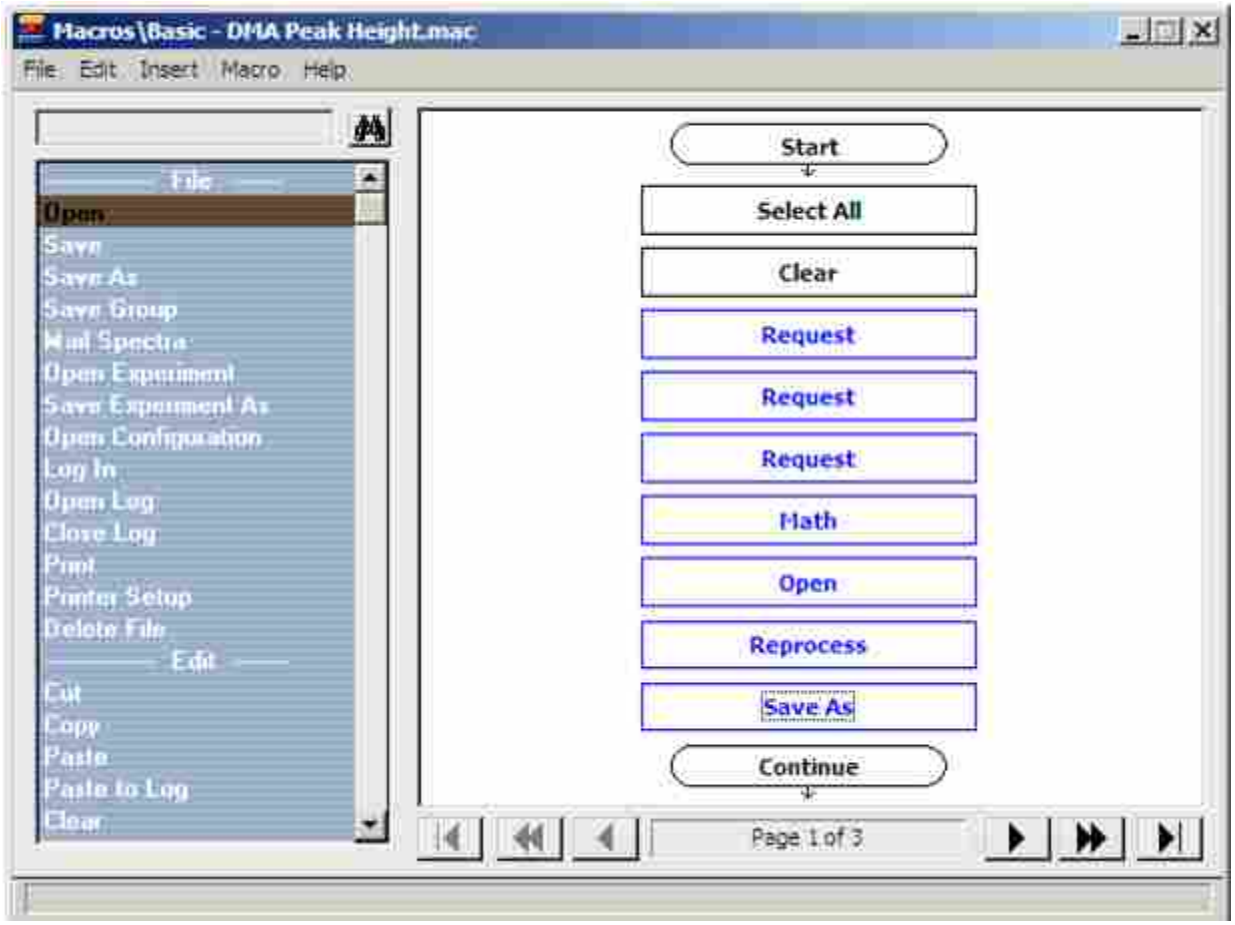

The following fields must be edited in the macro to correspond to the experimental data to be analyzed: Page 1: Open, Reprossess, Save As, Page 2: Open, Reprossess, Save As, and Page 3: Peak Height, Open Log. Each field is edited by double clicking.

In the window, change the "file name" to the location of the folder that has the single beam spectra followed by: \#mv6#.spa

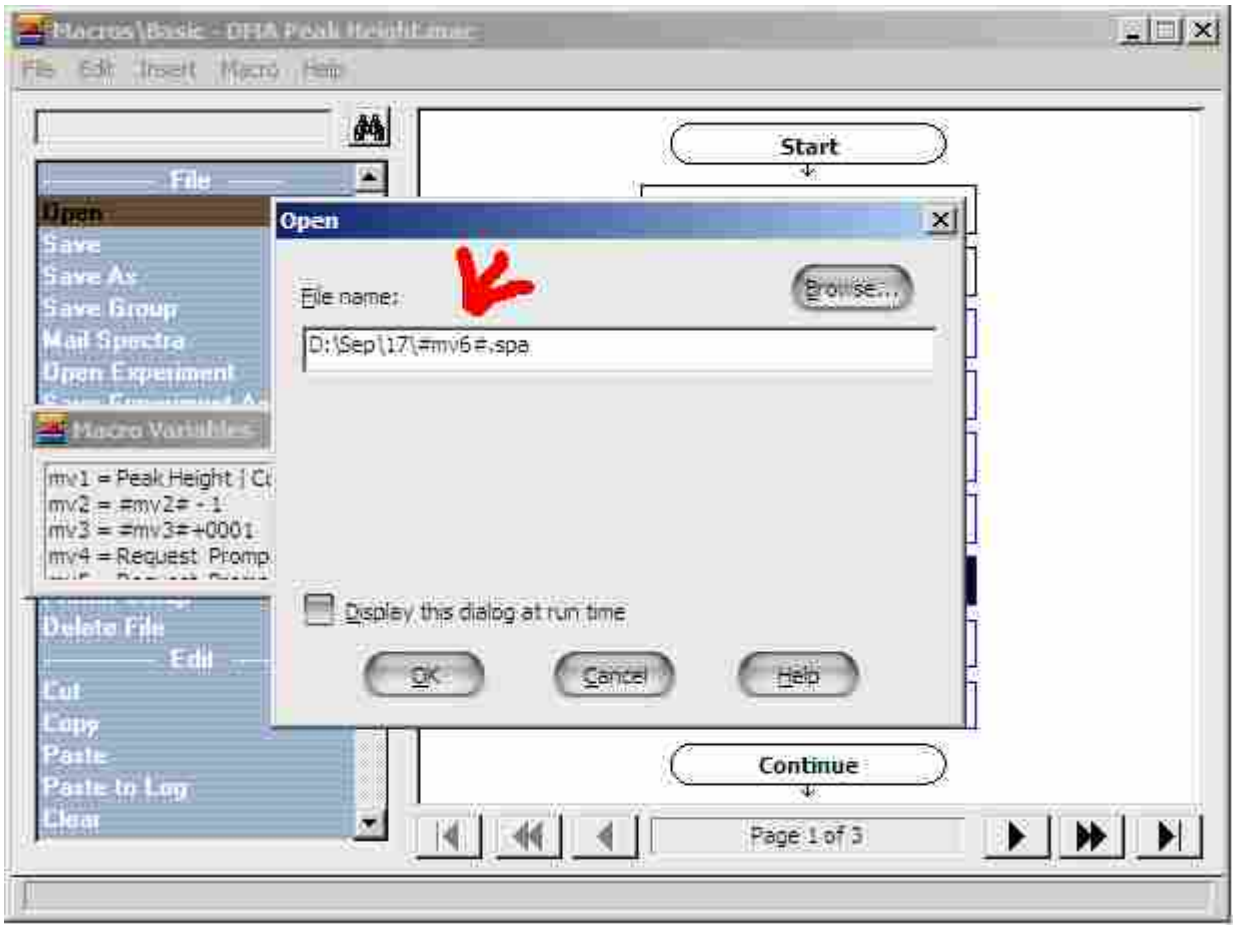

The location of your folder is what is written in the top left hand corner of the window when you have that folder open:

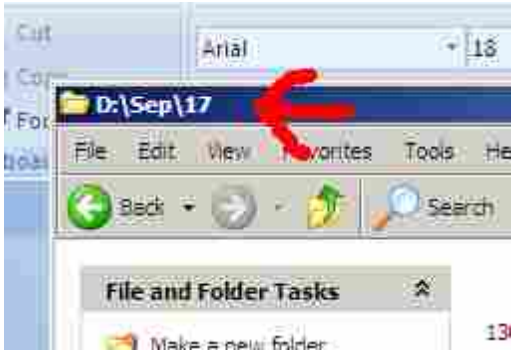

Press OK

The same thing is done for Save As, this time using the location of the folder the possessed absorbance spectra are to be saved.

The "Reprocess" field is to be edited by clicking "Browse" and selecting the reference spectra to be used in possessing.

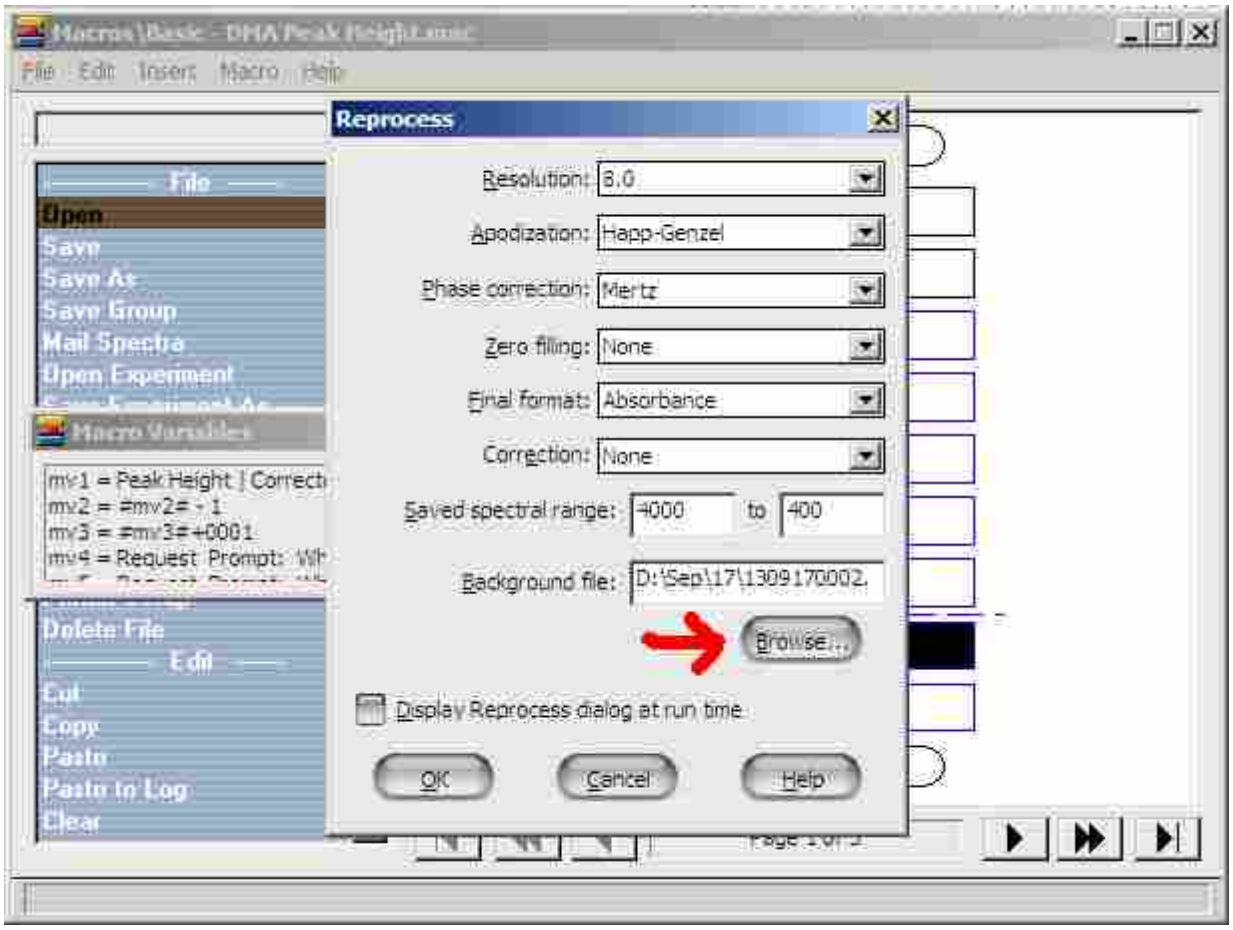

These steps are repeated for “Open”, “Save As” and “Reprocess” on page 2.

“Open Log” on page 3 is edited to include the file name of the resulting log file that is produced by the macros and where the file is to be saved.

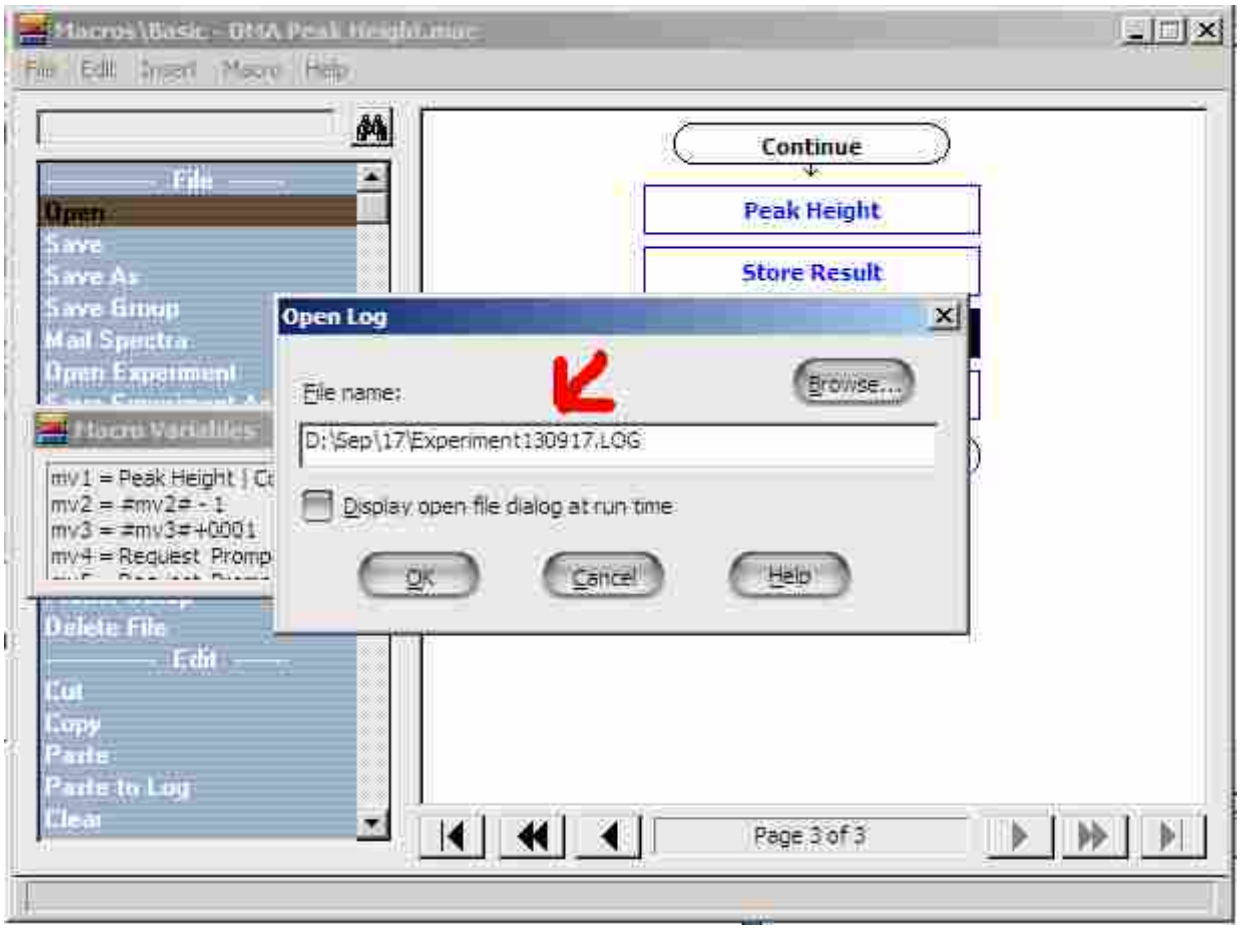

"Peak Height" is to be edited for the baseline and peak location of the absorbance peak being analyzed.

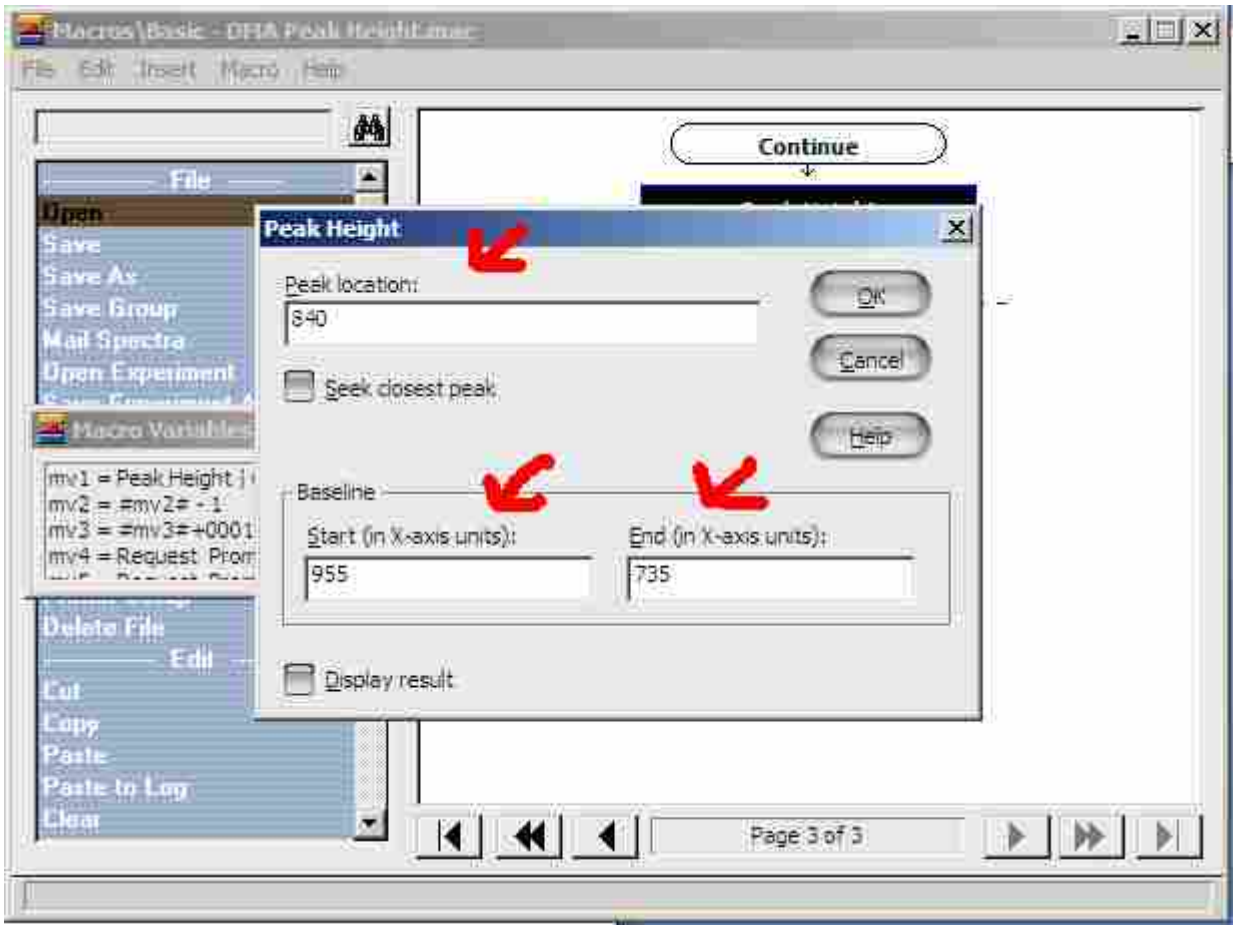

File then Save in the drop down menu.

File then Run in the drop down menu and select the macros analysis file

The last 4 digits of the single beam two before the first spectra to analyzed are entered into the first pop up.

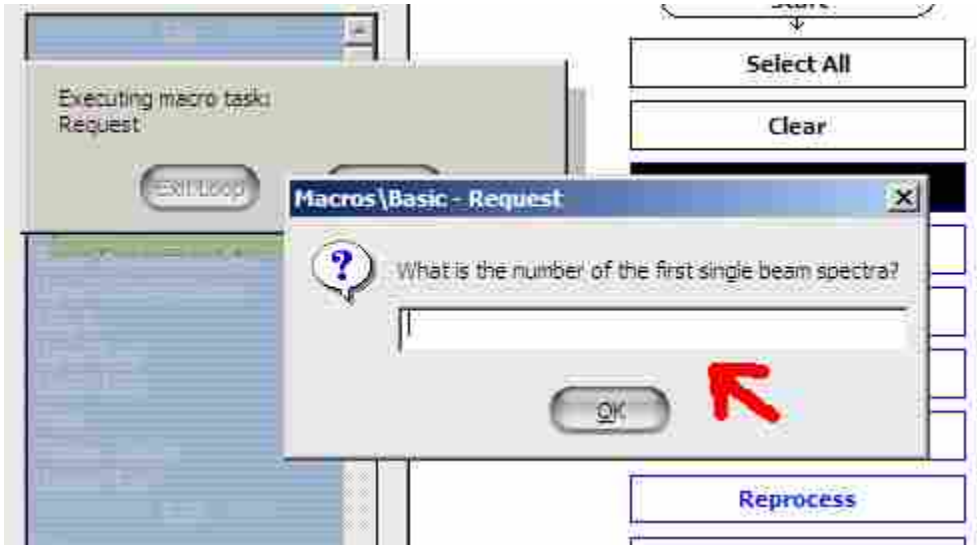

Two higher than the number of spectra to be possessed is entered into the second pop up.

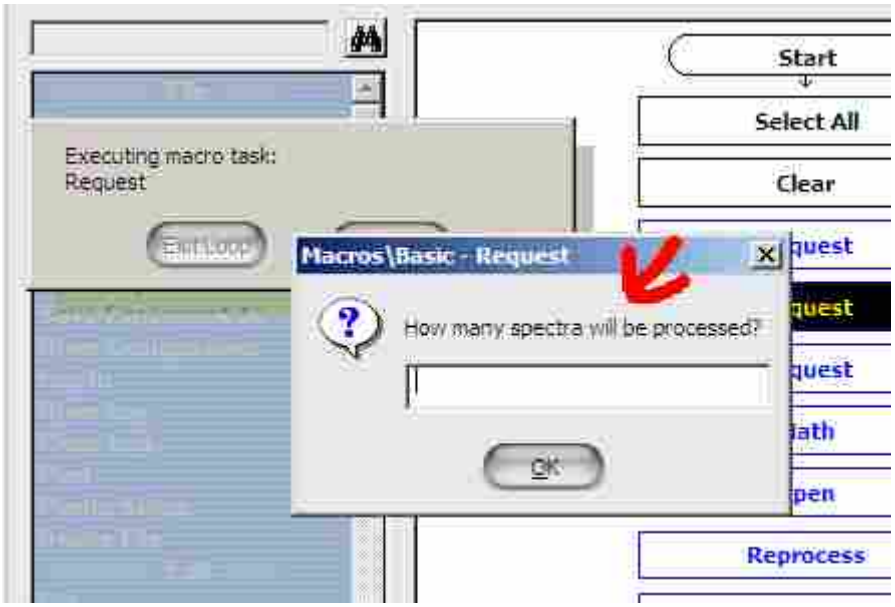

The base number of the spectra to be possessed (the number ahead of the last four numbers) is entered into the last pop up.

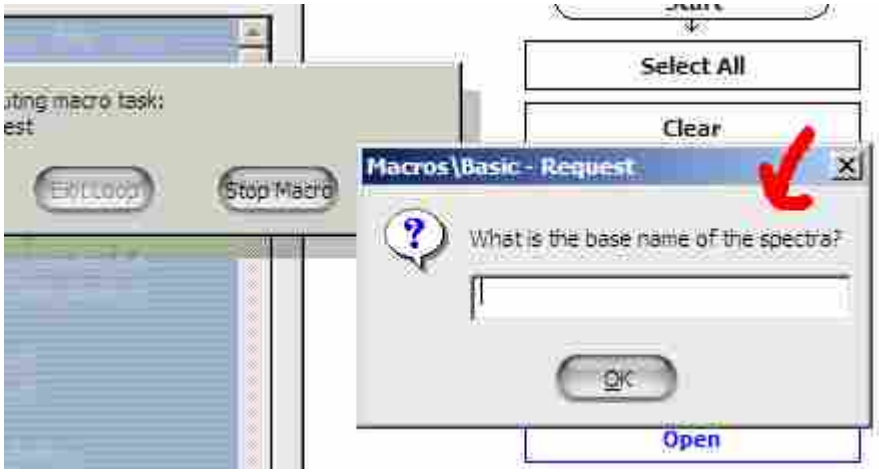

The macro is now running.

Once Macros is finished, the Omnic window is selected.

In Omnic; the log window is closed to generate the log file.

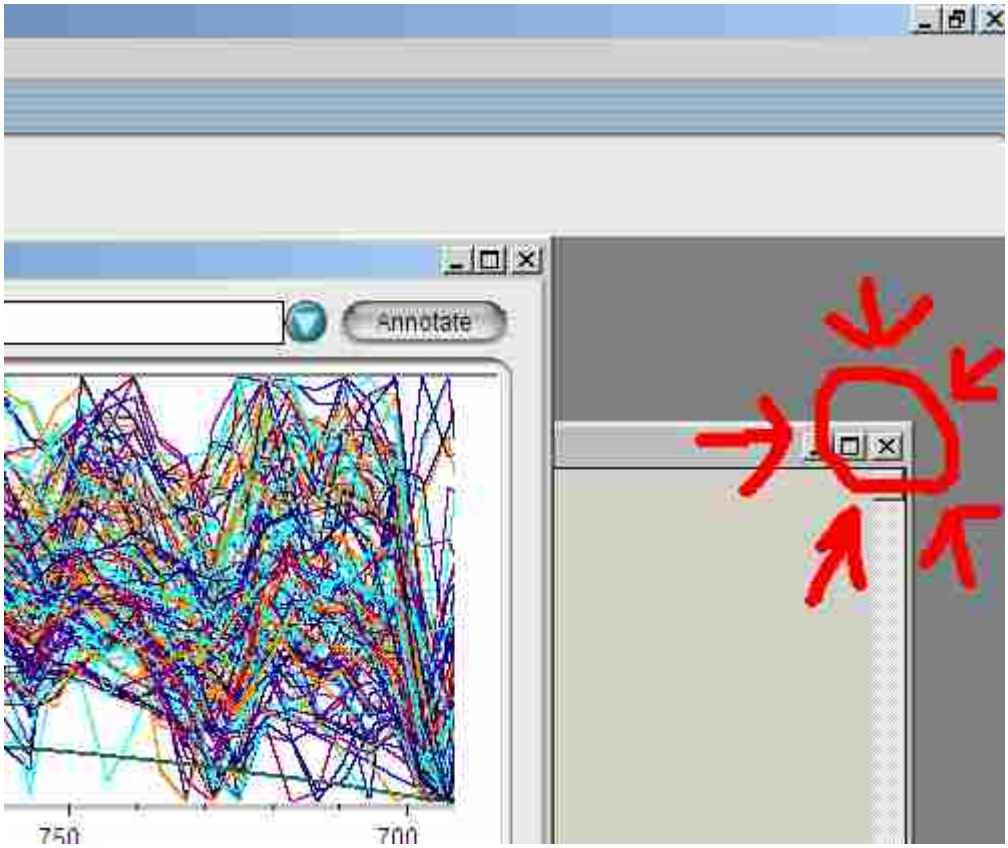

The log file is opened with Excel, column A selected and the Data tab selected.

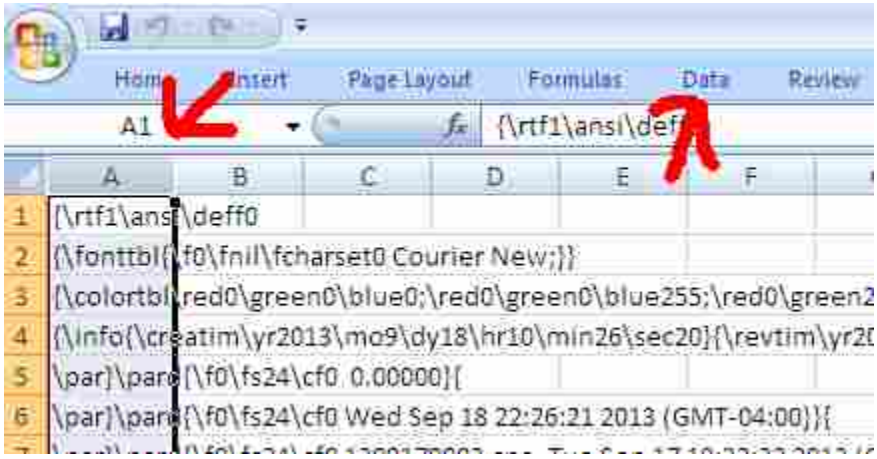

“Text to Columns” is selected and the data is changed to tab delimited as follows.

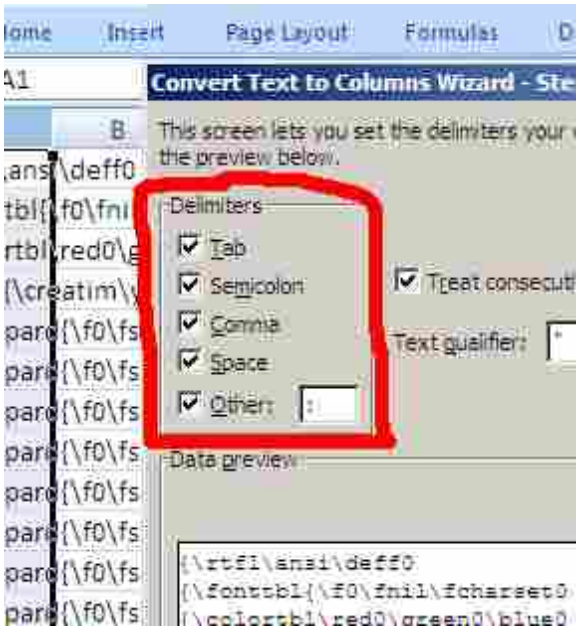

The Excel file now looks as follows:

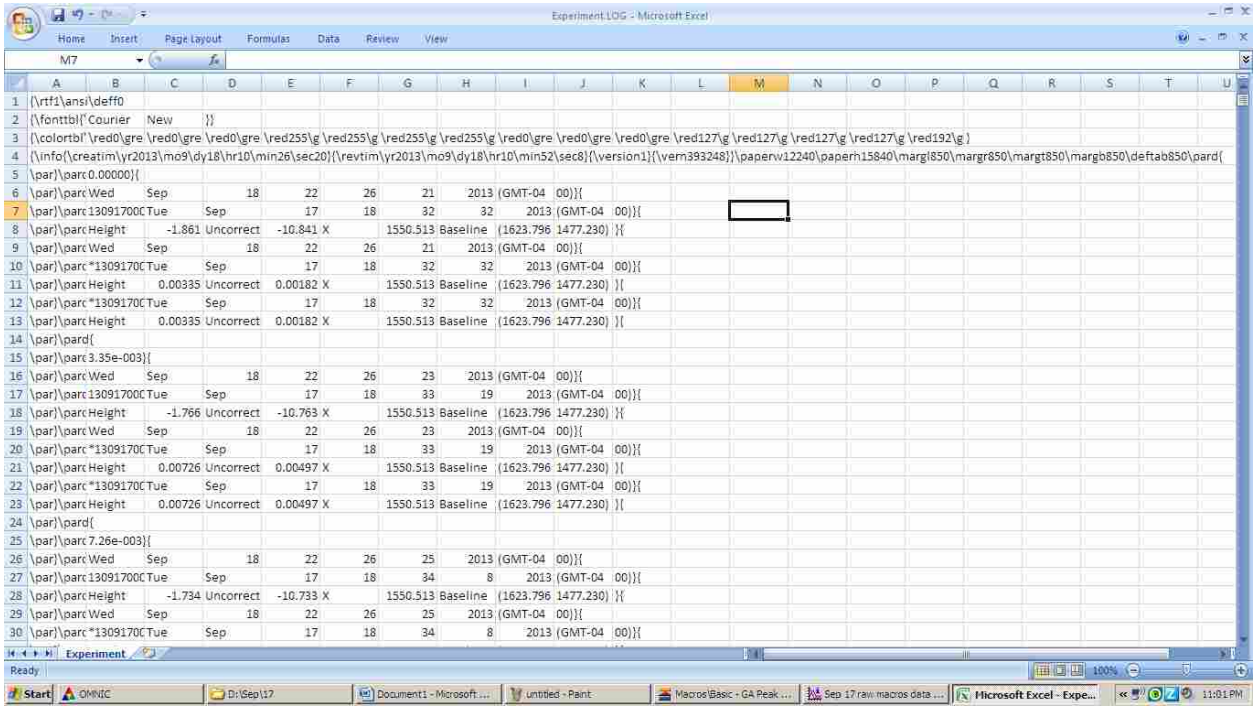

Using the OFFSET function the peaks heights are extracted.

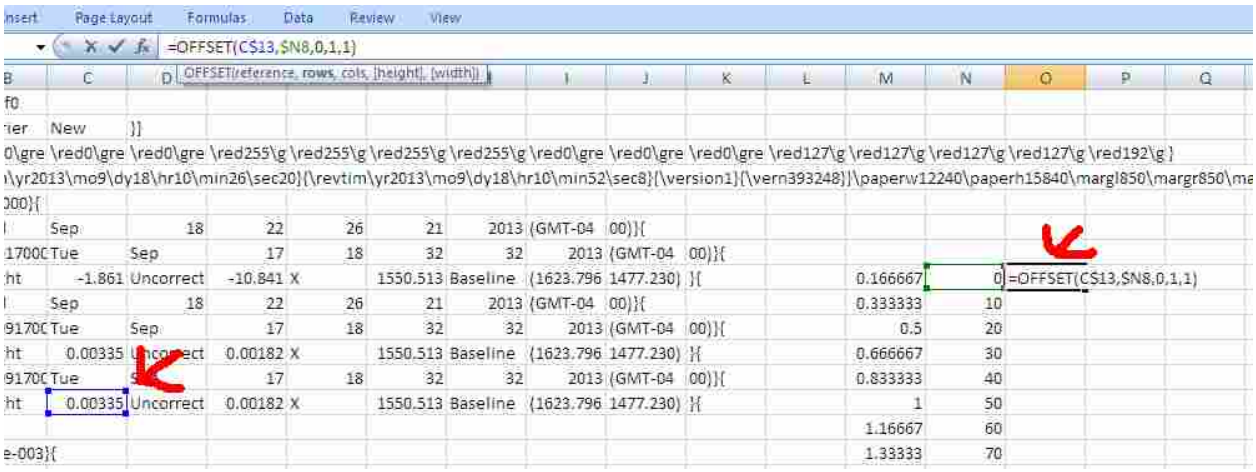

The peak height data can then be copied into Igor Pro for processing.

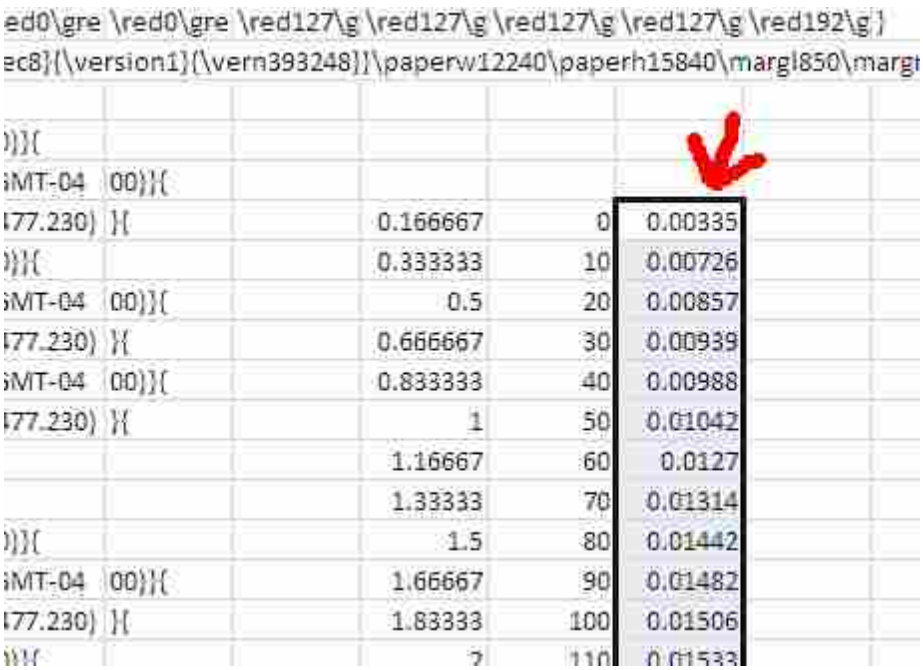

Appendix C: Spectral Math used in data analysis

Spectral math is used when analyzing spectra generated from aqueous tests (no film)

Both the single beam KCl reference spectrum (0002) and the single beam spectrum to be analyzed (0003) are opened.

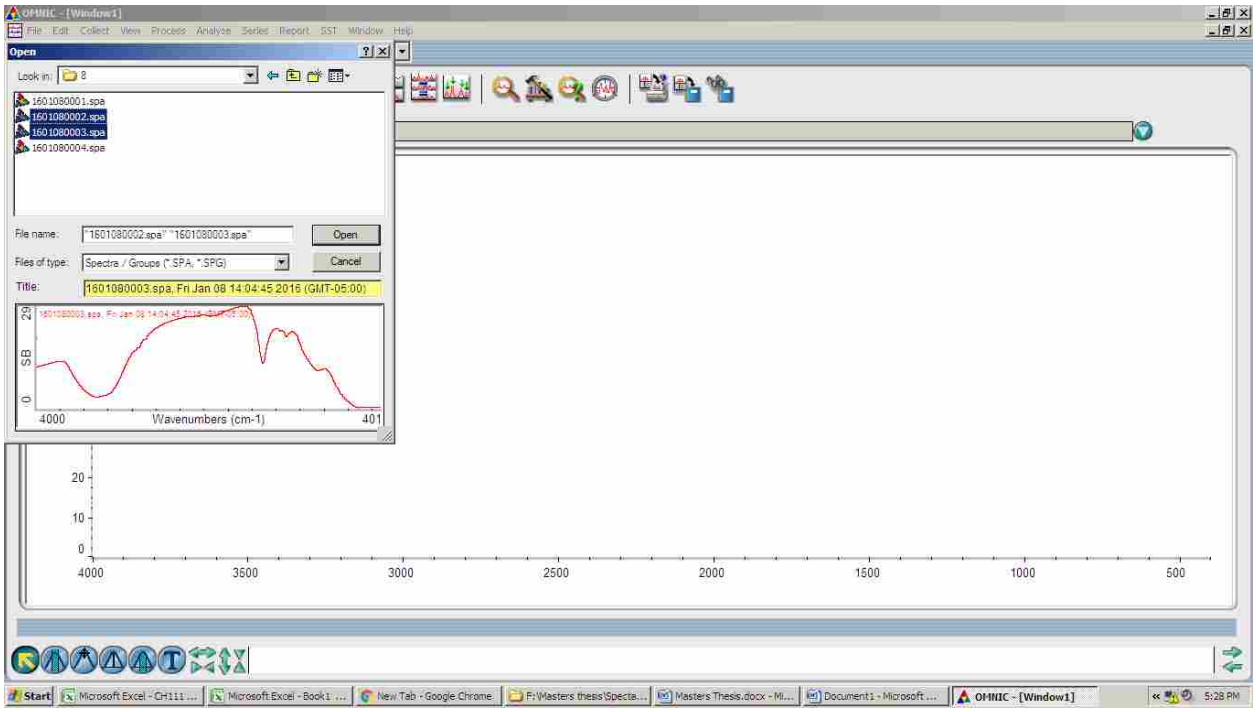

Absorbance spectra are generated by referencing both single beam spectrum to the dry ATR cell (0001) which is either Ge or ZnSe.

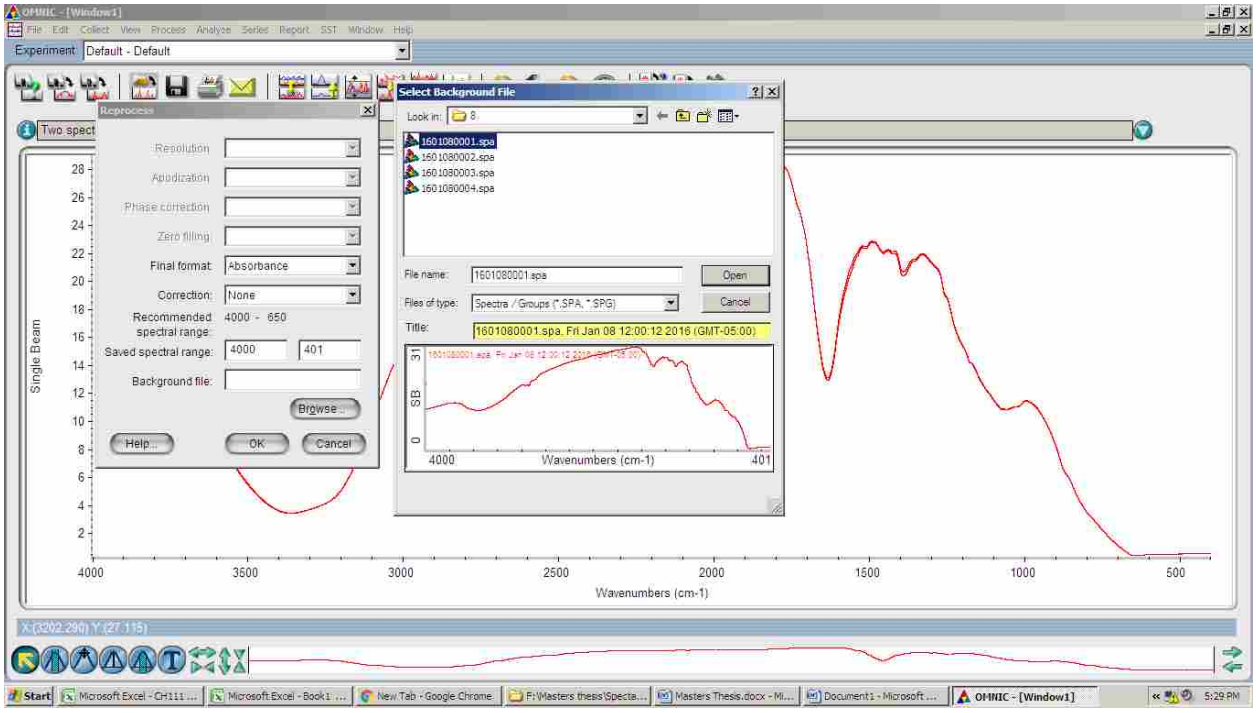

Spectral math is then opened by after selecting the spectra to be analyzed and the KCl reference spectrum in OMNIC.

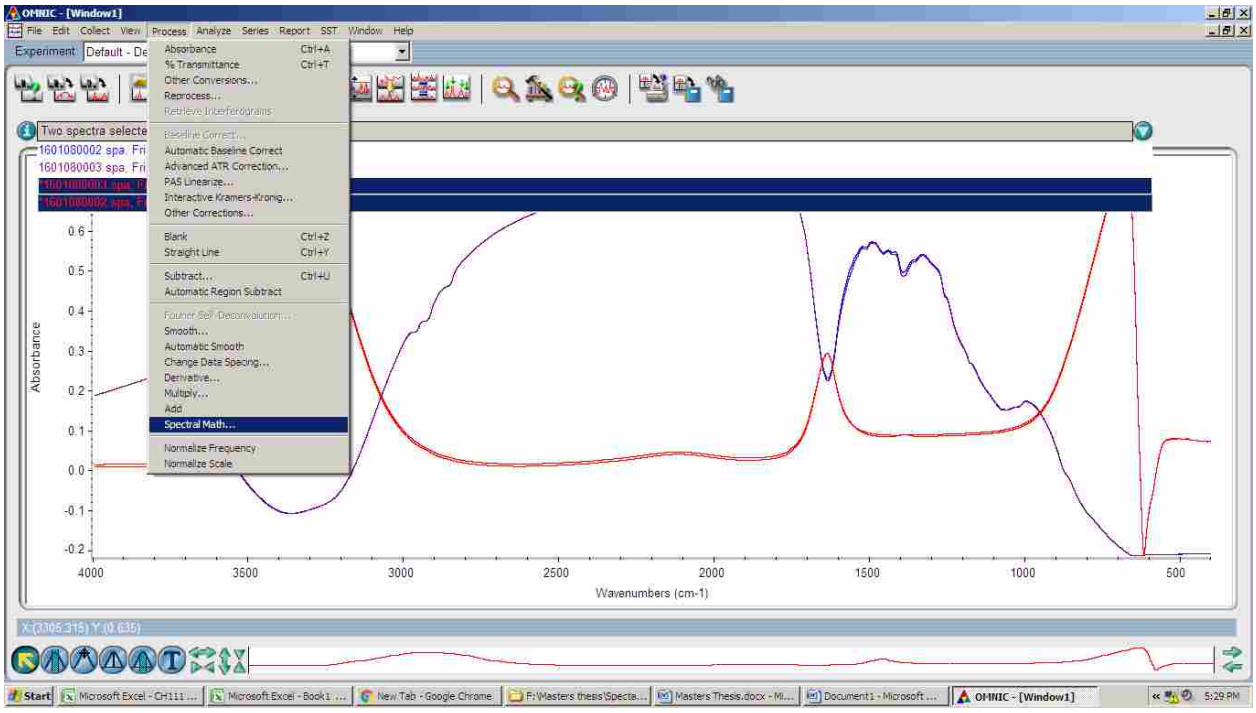

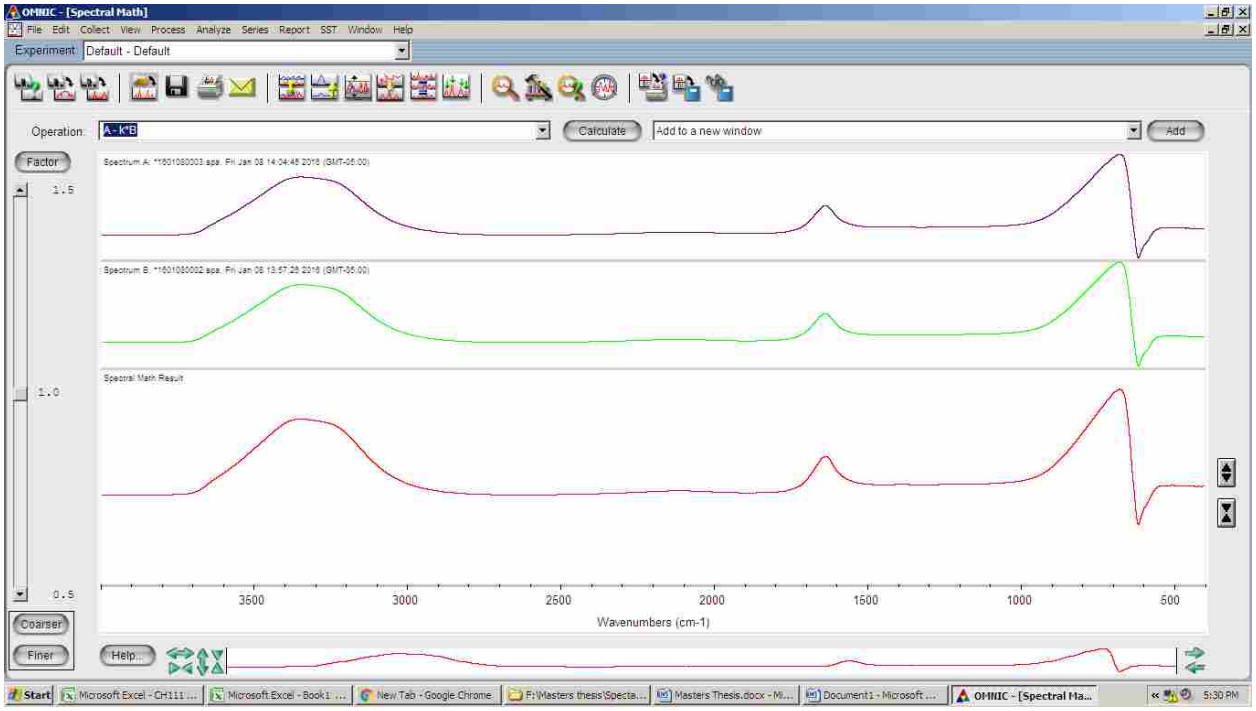

The resulting spectrum is generated in spectral math using “Calculate”.

The K factor is adjusted to minimize water absorbance at 1643cm^{-1}.

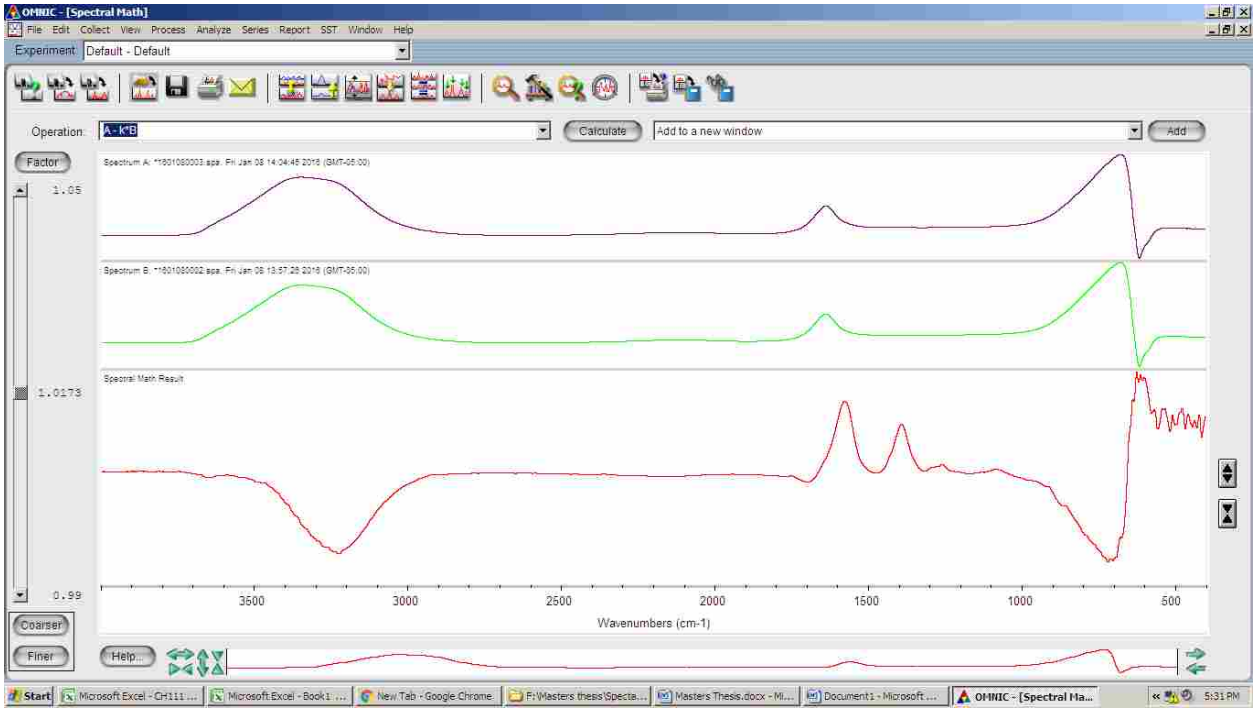

The absorbance spectrum is then added using "Add" to a new window in OMNIC for further analysis.

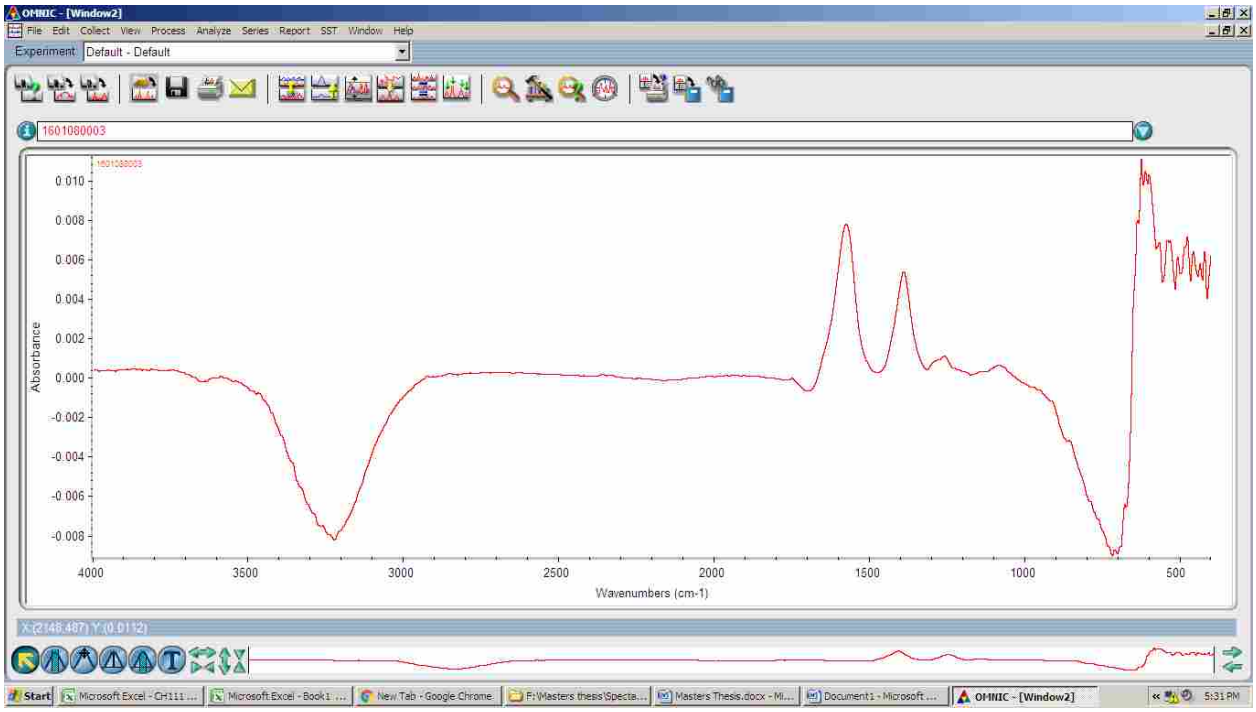

Appendix D: Speciation curve calculations

The following formulas where used to general the speciation curves presented in section 4.1 CHARACTERIZATION OF AQUEOUS PHASE MODEL ORGANICS USING ATR-FTIR.

Citric acid: CAH_3

$$[CAH_3] = \frac{CA_T}{1 + \frac{k_{a1}}{[H^+]} + \frac{k_{a1}k_{a2}}{[H^+]^2}}$$

$$[CAH_2^-] = \frac{CA_T}{\frac{[H^+]}{k_{a1}} + 1 + \frac{k_{a2}}{[H^+]} + \frac{k_{a2}k_{a3}}{[H^+]^2}}$$

$$[CAH^{2-}] = \frac{CA_T}{\frac{[H^+]^2}{k_{a1}k_{a2}} + \frac{[H^+]}{k_{a2}} + 1 + \frac{k_{a3}}{[H^+]}}$$

$$[CA^{3-}] = \frac{CA_T}{\frac{[H^+]^2}{k_{a2}k_{a3}} + \frac{[H^+]}{k_{a3}} + 1}$$

$k_{a1} = 3.13$, $k_{a2} = 4.76$, $k_{a3} = 6.40$, $CA_T = 0.001$M, concentrations normalized against this value.

Oxalic acid: OAH_2

$$[OAH_2] = \frac{OA_T[H^+]^2}{[H^+]^2 + k_{a1}[H^+] + k_{a1}k_{a2}}$$

$$[OAH^-] = \frac{OA_T k_{a1}[H^+]}{[H^+]^2 + k_{a1}[H^+] + k_{a1}k_{a2}}$$

$$[OA^{2-}] = \frac{OA_T k_{a1}k_{a2}}{[H^+]^2 + k_{a1}[H^+] + k_{a1}k_{a2}}$$

$k_{a1} = 1.25$, $k_{a2} = 4.14$, $OA_T = 0.001$M, concentrations normalized against this value.

Pyrocatechol: PCH_2

$$[PCH_2] = \frac{PC_T[H^+]^2}{[H^+]^2 + k_{a1}[H^+] + k_{a1}k_{a2}}$$

$$[PCH^-] = \frac{PC_T k_{a1}[H^+]}{[H^+]^2 + k_{a1}[H^+] + k_{a1}k_{a2}}$$

$$[PC^{2-}] = \frac{PC_T k_{a1}k_{a2}}{[H^+]^2 + k_{a1}[H^+] + k_{a1}k_{a2}}$$

k_{a1} = 9.4, k_{a2} = 12.8, PC_T = 0.001M, concentrations normalized against this value.

ReferencesUncategorized References

1. Cullen, W., Is Arsenic an Aphrodiatic? The Sociochemistry of an Element. RBC Publishing: Cambridge., 2008.
2. Smedley, P. L.; Kinniburgh, D. G., A review of the source, behaviour and distribution of arsenic in natural waters. *Applied Geochemistry* **2002,** *17* (5), 517-568.
3. Arts, D.; Abdus Sabur, M.; Al-Abadleh, H. A., Surface Interactions of Aromatic Organoarsenical Compounds with Hematite Nanoparticles Using ATR-FTIR: Kinetic Studies. *The Journal of Physical Chemistry A* **2013,** *117* (10), 2195-2204.
4. Kapaj, S.; Peterson, H.; Liber, K.; Bhattacharya, P., Human health effects from chronic arsenic poisoning--a review. *Journal of environmental science and health. Part A, Toxic/hazardous substances & environmental engineering* **2006,** *41* (10), 2399-428.
5. Moreno-Jimenez, E.; Esteban, E.; Penalosa, J. M., The fate of arsenic in soil-plant systems. *Reviews of environmental contamination and toxicology* **2012,** *215*, 1-37.
6. Wang, S.; Mulligan, C. N., Occurrence of arsenic contamination in Canada: sources, behavior and distribution. *The Science of the total environment* **2006,** *366* (2-3), 701-21.
7. Keeling, A.; Sandlos, J., Giant Mine: Historical Summary. **2012**.
8. Stellman, J. M.; Stellman, S. D.; Christian, R.; Weber, T.; Tomasallo, C., The extent and patterns of usage of Agent Orange and other herbicides in Vietnam. *Nature* **2003,** *422* (6933), 681-687.
9. Smith, E.; Naidu, R.; Alston, A. M., Arsenic in the soil environment. *Advances in Agronomy* **1998,** *64*, 149-195.
10. Davis, J. A. a. K., D. B., Surface Complexation Modeling in Aqueous Geochemistry. In *Mineral-Water Interface Geochemistry*, M. F. Hochella, J.; White, A. F., Eds. The Mineralogical Society of America: 1130 Seventeenth Street, N.W., Suite 330, Washington, D.C. 20036, 1990; Vol. 23, pp 177-260.
11. Dombrowski, P. M.; Long, W.; Farley, K. J.; Mahony, J. D.; Capitani, J. F.; Di Toro, D. M., Thermodynamic analysis of arsenic methylation. *Environmental science & technology* **2005,** *39* (7), 2169-2176.
12. Guidelines for Canadian Drinking Water Quality: Guideline Technical Document. Canada, H., Ed. Federal-Provincial-Territorial Committee on Drinking Water: 269 Laurier Avenue West, Ottawa, Ontario, 2006.
13. Smith, A. H.; Smith, M. M., Arsenic drinking water regulations in developing countries with extensive exposure. *Toxicology* **2004,** *198* (1-3), 39-44.
14. Korngold, E.; Belayev, N.; Aronov, L., Removal of arsenic from drinking water by anion exchangers. *Desalination* **2001,** *141* (1), 81-84.
15. Chakraborti, D.; Mukherjee, S. C.; Pati, S.; Sengupta, M. K.; Rahman, M. M.; Chowdhury, U. K.; Lodh, D.; Chanda, C. R.; Chakraborti, A. K.; Basu, G. K., Arsenic groundwater contamination in Middle Ganga Plain, Bihar, India: a future danger? *Environmental health perspectives* **2003,** *111* (9), 1194-201.
16. Jain, C. K.; Ali, I., Arsenic: occurrence, toxicity and speciation techniques. *Water Research* **2000,** *34* (17), 4304-4312.
17. Duckworth, O. W.; Martin, S. T., Surface complexation and dissolution of hematite by C1-C6 dicarboxylic acids at pH = 5.0. *Geochimica et Cosmochimica Acta* **2001,** *65* (23), 4289-4301.
18. Kalbitz, K.; Kaiser, K., Contribution of dissolved organic matter to carbon storage in forest mineral soils. *Journal of Plant Nutrition and Soil Science* **2008,** *171* (1), 52-60.

19. Kaiser, K.; Guggenberger, G., The role of DOM sorption to mineral surfaces in the preservation of organic matter in soils. *Organic Geochemistry* **2000,** *31* (7–8), 711-725.
20. Kramer, M. G.; Sanderman, J.; Chadwick, O. A.; Chorover, J.; Vitousek, P. M., Long-term carbon storage through retention of dissolved aromatic acids by reactive particles in soil. *Global Change Biology* **2012,** *18* (8), 2594-2605.
21. Lalonde, K.; Mucci, A.; Ouellet, A.; Gelinas, Y., Preservation of organic matter in sediments promoted by iron. *Nature* **2012,** *483* (7388), 198-200.
22. Jones, D., Organic acids in the rhizosphere – a critical review. *Plant and Soil* **1998,** *205* (1), 25-44.
23. Wang, S. L.; Mulligan, C. N., Enhanced mobilization of arsenic and heavy metals from mine tailings by humic acid. *Chemosphere* **2009,** *74* (2), 274-279.
24. Au, K.-K.; Penisson, A. C.; Yang, S.; O'Melia, C. R., Natural organic matter at oxide/water interfaces: complexation and conformation. *Geochimica et Cosmochimica Acta* **1999,** *63* (19–20), 2903-2917.
25. Ko, I.; Kim, J. Y.; Kim, K. W., Arsenic speciation and sorption kinetics in the As-hematite-humic acid system. *Colloid Surf. A-Physicochem. Eng. Asp.* **2004,** *234* (1-3), 43-50.
26. Redman, A. D.; Macalady, D. L.; Ahmann, D., Natural organic matter affects arsenic speciation and sorption onto hematite. *Environmental science & technology* **2002,** *36* (13), 2889-96.
27. Mladenov, N.; Zheng, Y.; Simone, B.; Bilinski, T. M.; McKnight, D. M.; Nemergut, D.; Radloff, K. A.; Rahman, M. M.; Ahmed, K. M., Dissolved Organic Matter Quality in a Shallow Aquifer of Bangladesh: Implications for Arsenic Mobility. *Environmental science & technology* **2015,** *49* (18), 10815-10824.
28. Sharma, P.; Ofner, J.; Kappler, A., Formation of Binary and Ternary Colloids and Dissolved Complexes of Organic Matter, Fe and As. *Environmental science & technology* **2010,** *44* (12), 4479-4485.
29. Mikutta, C.; Kretzschmar, R., Spectroscopic Evidence for Ternary Complex Formation between Arsenate and Ferric Iron Complexes of Humic Substances. *Environmental science & technology* **2011,** *45* (22), 9550-9557.
30. Ritter, K.; Aiken, G. R.; Ranville, J. F.; Bauer, M.; Macalady, D. L., Evidence for the Aquatic Binding of Arsenate by Natural Organic Matter−Suspended Fe(III). *Environmental science & technology* **2006,** *40* (17), 5380-5387.
31. Wang, S. L.; Mulligan, C. N., Effects of three low-molecular-weight organic acids (LMWOAs) and pH on the mobilization of arsenic and heavy metals (Cu, Pb, and Zn) from mine tailings. *Environ. Geochem. Health* **2013,** *35* (1), 111-118.
32. Evanko, C. R.; Dzombak, D. A., Influence of Structural Features on Sorption of NOM-Analogue Organic Acids to Goethite. *Environmental science & technology* **1998,** *32* (19), 2846-2855.
33. Yeasmin, S.; Singh, B.; Kookana, R. S.; Farrell, M.; Sparks, D. L.; Johnston, C. T., Influence of mineral characteristics on the retention of low molecular weight organic compounds: A batch sorption–desorption and ATR-FTIR study. *Journal of colloid and interface science* **2014,** *432*, 246-257.
34. Persson, P.; Axe, K., Adsorption of oxalate and malonate at the water-goethite interface: molecular surface speciation from IR spectroscopy. *Geochimica et Cosmochimica Acta* **2005,** *69* (3), 541-552.

35. Yang, Y.; Yan, W.; Jing, C., Dynamic Adsorption of Catechol at the Goethite/Aqueous Solution Interface: A Molecular-Scale Study. *Langmuir* **2012,** *28* (41), 14588-14597.
36. Hug, S. J.; Bahnemann, D., Infrared spectra of oxalate, malonate and succinate adsorbed on the aqueous surface of rutile, anatase and lepidocrocite measured with in situ ATR-FTIR. *Journal of Electron Spectroscopy and Related Phenomena* **2006,** *150* (2–3), 208-219.
37. Gulley-Stahl, H.; Hogan, P. A.; Schmidt, W. L.; Wall, S. J.; Buhrlage, A.; Bullen, H. A., Surface Complexation of Catechol to Metal Oxides: An ATR-FTIR, Adsorption, and Dissolution Study. *Environmental science & technology* **2010,** *44* (11), 4116-4121.
38. Tofan-Lazar, J.; Al-Abadleh, H. A., ATR-FTIR studies on the adsorption/desorption kinetics of dimethylarsinic acid on iron-(oxyhydr)oxides. *The journal of physical chemistry. A* **2012,** *116* (6), 1596-604.
39. Sabur, M. A.; Al-Abadleh, H. A., Surface interactions of monomethylarsonic acid with hematite nanoparticles studied using ATR-FTIR: adsorption and desorption kinetics. *Canadian Journal of Chemistry* **2015,** *93* (11), 1297-1304.
40. Sabur, M. A.; Goldberg, S.; Gale, A.; Kabengi, N.; Al-Abadleh, H. A., Temperature-Dependent Infrared and Calorimetric Studies on Arsenicals Adsorption from Solution to Hematite Nanoparticles. *Langmuir* **2015,** *31* (9), 2749-2760.
41. Hind, A. R.; Bhargava, S. K.; McKinnon, A., At the solid/liquid interface: FTIR/ATR — the tool of choice. *Advances in Colloid and Interface Science* **2001,** *93* (1–3), 91-114.
42. Noerpel, M. R.; Lenhart, J. J., The impact of particle size on the adsorption of citrate to hematite. *Journal of colloid and interface science* **2015,** *460*, 36-46.
43. Lefèvre, G.; Preočanin, T.; Lützenkirchen, J., Attenuated total reflection - Infrared spectroscopy applied to the study of mineral - aqueous electrolyte solution interfaces: a general overview and a case study. In *Infrared Spectroscopy*, Theophile, T., Ed. Intech: 2012.
44. Öhrström, L.; Michaud-Soret, I., Fe−Catecholate and Fe−Oxalate Vibrations and Isotopic Substitution Shifts from DFT Quantum Chemistry. *The Journal of Physical Chemistry A* **1999,** *103* (2), 256-264.
45. Situm, A.; Goldberg, S.; Al-Abadleh, H. A., Spectral Characterization and Surface Complexation Modeling of Organics on Hematite Nanoparticles: An Interface Important in Environmental Systems and Medical Applications. *Environmental Science: Nano (Submitted)* **2016**.
46. Arai, Y.; Sparks, D. L.; Davis, J. A., Effects of dissolved carbonate on arsenate adsorption and surface speciation at the hematite--water interface. *Environmental science & technology* **2004,** *38* (3), 817-24.
47. Filius, J. D.; Hiemstra, T.; Van Riemsdijk, W. H., Adsorption of Small Weak Organic Acids on Goethite: Modeling of Mechanisms. *Journal of colloid and interface science* **1997,** *195* (2), 368-380.
48. Geelhoed, J. S.; Hiemstra, T.; Van Riemsdijk, W. H., Competitive Interaction between Phosphate and Citrate on Goethite. *Environmental science & technology* **1998,** *32* (14), 2119-2123.
49. Marcussen, H.; Holm, P. E.; Strobel, B. W.; Hansen, H. C. B., Nickel Sorption to Goethite and Montmorillonite in Presence of Citrate. *Environmental science & technology* **2009,** *43* (4), 1122-1127.
50. Hiemstra, T.; Van Riemsdijk, W. H., A Surface Structural Approach to Ion Adsorption: The Charge Distribution (CD) Model. *Journal of colloid and interface science* **1996,** *179* (2), 488-508.

51. Brechbuhl, Y.; Christl, I.; Elzinga, E. J.; Kretzschmar, R., Competitive sorption of carbonate and arsenic to hematite: combined ATR-FTIR and batch experiments. *Journal of colloid and interface science* **2012,** *377* (1), 313-21.